POLYCHROMATIC X-RAY DIFFRACTION USING A PNCCD: APPLICATIONS FOR MATERIAL SCIENCE

DISSERTATION
zur Erlangung des Grades eines Doktors der Naturwissenschaften

vorgelegt von
M. Sc. Ali Abboud

eingereicht bei der Naturwissenschaftlich-Technischen Fakultät
der Universität Siegen
Siegen 2015

Gutachter:
Prof. Dr. Dr. Ullrich Pietsch
Prof. Dr. Lothar Strüder

Datum der mündlichen Prüfung: 17.02.2015

Prüfer:
Prof. Dr. Dr. Ullrich Pietsch
Prof. Dr. Lothar Strüder
Prof. Dr. Otfried Gühne
Prof. Dr. Andreas Kolb

Zusammenfassung

Die Bereitstellung von kleineren und immer leistungsstärkeren Bauelementen der Elektronik oder von Metallen mit hoher Dauerfestigkeit unter großer Beanspruchung sind einige von vielen Anforderungen, die die moderne Technik erfüllen muss. Die Herstellung dieser Materialien verlangt einbesseres Verständnis von strukturellen Materialeigenschaften auf molekularer Ebene. Dieser Bedarf agiert als Triebkraft der Entwicklung neuer experimenteller Methoden und von Werkzeugen der Datenanalyse. In den letzten Jahren ist eine Vielfalt von neuen Analysetechniken entwickelt worden. Dazu gehören zerstörungsfreie Verfahren wie die Röntgen-Mikrocomputertomografie (CT), die 3D-Röntgenbeugung, die ortsaufgelöste Röntgenbeugung, die Transmission-Elektronenmikroskopieund die Tomographie. Die meisten dieser Verfahrenerfordern oft ein zeitaufwändiges Scannen der Probe, was nur bei sehr stabilen experimentellen Bedingungen möglich ist. Innerhalb dieser breiten Palette an Werkzeugen zur Materialanalyse stellt die energiedispersive 2D-Röntgenbeugung eine neuartige zerstörungsfreie und schnelle Analysetechnik dar. Dafür müssen sowohl die entsprechende brillante Röntgenstrahlung sowie geeignete Nachweissysteme zur Verfügung stehen. Brillante Röntgenstrahlung kanndurch Synchrotronstrahlungsquellen der dritten Generation erzeugt werden. Diese Quellen liefern kohärente, mikrometerfokussierte Röntgenstrahlung in einem breiten Spektralbereich. Daneben ermöglicht Synchrotronstrahlung auf Grund ihrer hohen Intensitt zeitaufgelöste Untersuchung der Probe mit guter Zhlstatistik. Allerdings kann in vielen Anwendungennicht das volle Potenzial der Synchrotronstrahlung ausgeschöpft werden, wasauf teilweise unterentwickelte Detektortechnologien zurückzufhren ist. Die größte Hürde für die Detektortechnologie besteht darin, gleichzeitig die Energie und die Position des detektierten Photons zu bestimmen. Diese Fähigkeit besitzt erstmals

der ”pn-junction type CCD” Sensor der Firma pnSensor GmbH. Diese Dissertation beschäftigt sich mit der Entwicklung von Methoden, die den Einsatz von pnCCD in polychromatischen Röntgenbeugungsexperimenten ermöglichen. Einerseits wird der pnCCD Sensor verwendet, um die Energie von Laue-Spots eines verformten Kupferkristalls aufzulösen. Mit diesem Ansatzentfällt die Notwendigkeit der vorherigen Bestimmung der Energie des einfallenden Strahls. Andererseits werden thermisch induzierte Interdiffusionsprozesse in einem metallischen Mehrschichtsystem (Eisen-Platin) durch Röntgenreflektometrie mit weißer-Synchrotronstrahlung auf der Zeitskala von wenigen Minuten dargestellt. Dies geschieht bei Energien in der Nähe der Absorptionskanten des Probematerials, um den Elektronendichtekontrastzu verbessern. Die in dieser Dissertation präsentierten Methoden ermöglichen der Einsatz hochbrillanterpolychromatischer Sybchrotronstrahlung in Verbindung mit einem pnCCD Detektor, um das Grundverständnis von Materialeigenschaften auf atomarerEbene zuverbessern.

Abstract

The need to understand material structural properties is driving the development of new experimental methods and tools of investigation and data analysis. For example, thinner mobile phones, efficient electronic devices and materials that can withstand high fatigue cycles are only a few of what the requirements for everyday appliances are. In the process, the physical properties of materials need to be understood at the micro level scale.

In recent years, a variety of three dimensional depth probing techniques has been developed. These include non destructive methods such as X-ray micro computer tomography (CT), 3D X-ray diffraction, spatially resolved X-ray diffraction, transmission electron microscopy, and tomography[1] Most of these techniques require time consuming sample scans that destabilize the experiment.

Within this broad range of possible tools for material analysis, 2-dimensional, energy dispersive X-ray diffraction stands out as a non destructive and rapid probing technique, provided that the appropriate X-ray sources and suitable detection systems are available.

Brilliant X-rays can be found in third generation synchrotron radiation facilities. These provide coherent X-rays with a continuous spread of wavelengths and micro meter focused beams. A synchrotron source also provides the sufficient intensity needed for time resolved studies. However, the detector technology still lags behind, limiting the complete exploitation of the capabilities of synchrotron radiation in research. Such limitations are attributed to the inability to simultaneously acquire the energy and the position of the diffracted photons from the material under investigation, which is crucial in order to avoid sample rotations.

[1] International Congress on 3D Materials Science 2014. Correlative 3D Imaging Across Time and Length Scales.

The pn-junction type CCD from pnSensor GmbH is a detector which provides a solution. This thesis focuses on developing methods in which the pnCCD is utilized for polychromatic X-ray diffraction experiments. On one side it explores the possibilities to use the pnCCD to resolve the energetic structure of Laue spots originating from deformed single crystals (Copper). This approach circumvents the need to know the energy of the incident beam on the sample as a priori to the measurement. On the other side, a metallic multilayer system (Iron-Platinum) is probed in a Grazing-incidence scattering experiment while annealing. The resulting inter-diffusion process is dynamically monitored on the time scale of few minutes, and at energies close the absorption edges of the sample material, in order to enhance electron density contrast. The developed methods make it possible to utilize the hight brilliant and polychromatic characteristics of new generation synchrotron radiation sources with a pnCCD detector to improve materials understanding.

Contents

Chapter 1

Introduction

The pnCCD was developed and funded by the Max-Planck-Institute Für Extraterrestrische Physik (MPE) for the European Space Agency (ESA) and the USA National Aeronautics and Space Administration (NASA) as an imaging X-ray spectrometer for European Space Agency X-ray Multi Mirror mission (XMM). The pnCCD is derived from silicon drift detectors developed by Gatti and Rehak [2]. Strüder [3] modified the basic concept and performed a complete device simulation. After further modifications the first working devices were produced in the year 1993. The XMM mission requested an energy resolving 2D detector with maximum quantum efficiency between 1 and 10 keV, frame rates above 100 Hz and an energy resolution close to the Silicon Fano limit. Dark and leakage currents were suppressed by cooling the device down to -60 °C. Operation in the single counting mode implies that photons should neither overlap in space nor in time. For bright sources, only a part of the detector active area is used and frames can reach several kHz [3]. To operate in space, radiation hardness of the device is needed. Measurements with an intense beam of about $2x10^9$ MeV protons per cm^2 predicted that during a lifetime in space of 10 years, the FWHM of the Mn$K\alpha$ line would increase by 30 eV at most [4].
In 2002 the University of Siegen stepped into a collaboration with the **MPE** and **PnSensor GmbH** in order to develop the pnCCD camera for research in the fields of Solid State Physics and Medical imaging. The challenge was to utilize the capabilities of a device designed for space exploration with the experimental demands

of X-ray research and in particular for the use of highly intense synchrotron radiation.
As a result intensive studies have performed to develop and test new experimental methods and new tools for data analysis. Below is a list of the issues under investigations:

- Increasing the frame rate in order to measure dynamical process and to limit undesirable effects such as signal pile up.
- Investigate the limits of the pixel full-well capacitance (Dynamic range). High intensity synchrotron sources require that each pixel saturation threshold is quantified in order to tune the photon flux to a suitable range.
- Sub-pixel positional resolution for spatial-resolved experiments. Traditional diffraction benefits from high spatial resolution in the q-space and therefore new developed methods are required to achieve sub-pixel resolution.
- To get reliable quantitative results Quantum Efficiency studies are essential **QE**, in which the interaction cross-sections of radiation with matter are included.
- Energy resolution and gain linearity studies were performed.
- Data handling and storing techniques were developed to address the Gigabyte **GB** data flow.
- Software routines and algorithms were developed to handle 3-dimensional data sets in order to extract reliable information from experiments.

Many experiments were performed to verify the camera performance. In this thesis a few of these experiments are presented along with the newly developed methods and data analysis techniques.
The general aim of the work is to develop new experimental methods for polychromatic X-ray diffraction. Two particular experiments are performed to asses quantitatively and qualitatively the performance of the pnCCD. First, the dynamics of inter-diffusion at the interfaces of a metallic multilayer is studied. Second,

the deformations in the real structure of a single crystal Copper cantilever after deformation is investigated.

Chapter 2

Concept of the pnCCD

This chapter describes the concept of a charge-coupled-device **CCD** and the steps that lead to the development of the pn-junction CCD. The concept of X-ray detection with the pnCCD is also presented along with the technical realization needed for operation of the device. The physical properties of the device are defined and different operation modes are presented. These properties include spatial and energy resolution, charge handling capacity, quantum efficiency and the burst operation mode for high frame rates.

2.1 From CCDs to pnCCDs

The charge coupled device was invented by Smith and Boyle in 1969 while they were looking for a memory device working at Bells laboratories. It was not difficult to immediately figure out the benefits and the possible applications of the device. These applications promoted the rapid development of the CCD.
Functioning as a practical imaging device, the existence of the CCD effected greatly the imaging technology. Its practical applications stretched over many areas such as commercial camera devices medical imaging, e.g. imaging of the human body, surgery and diagnostics. In astronomy, the CCD proved to be a valuable tool in mapping the optical and X-ray radiations of the universe.
The charge coupled device is based on a Metal-Oxide-Silicon three layer formation know as **MOS** capacitor. Figure 2.1, shows the structure of the MOS capac-

itor in depletion mode. In its simplest function, the MOS capacitor is a memory device used to store charges underneath the metal-oxide coupler.
Charges are created in the depletion region by photoelectric effect and cause a change in the potential at the surface. The number of the created charges is proportional to the energy of the photon. In order to transfer the stored charges, many MOS capacitors are stacked next to each other and a 3 phase transfer cycle is applied to move the stored charges to a terminal read out anode. The result is a functional device that makes use of stored charge packets to preserve the accumulated charge pattern. In the early stages of test and development the CCD suffered from transfer inefficiency.

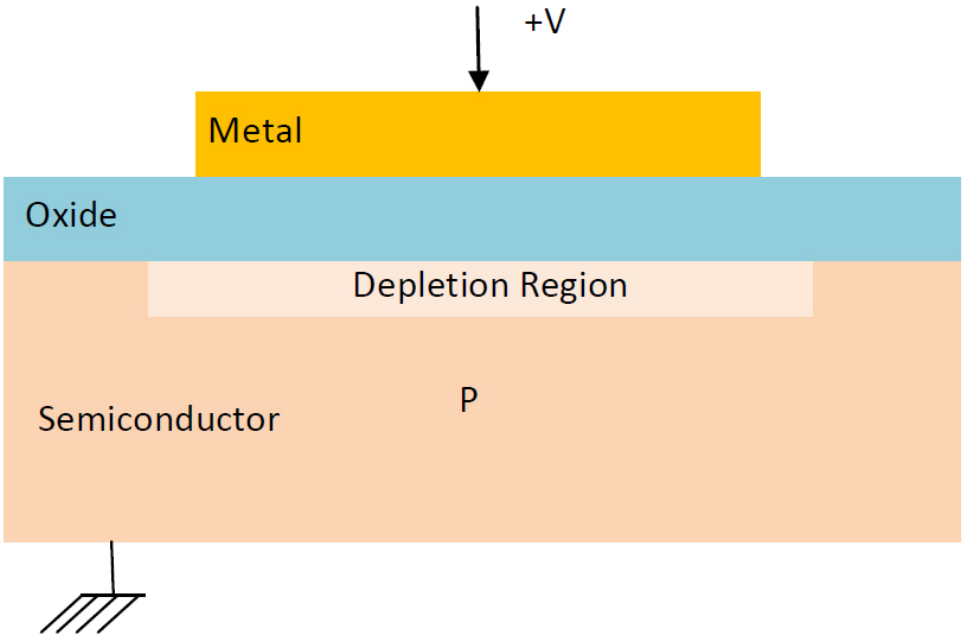

Figure 2.1: The Metal Oxide Semiconductor MOS forms the basis of most charged coupled devices. Under an applied external voltage; at the metal contact, a depletion region takes form in the p-type semiconductor.

As the stored charges move close to the oxide surface, they become trapped at the interface for an interval of time. This effect causes the image to be smeared out. The solution to this problem comes with the buried channel CCD where the charge packets are moved away from the surface into the bulk of the silicon substrate as seen in figure 2.2.

The development of the device was rapid and driven by intense competition between different manufacturers. On 6th of October of 2009 the Royal Swedish Academy of Science decided to award Willard S. Boyle and George E. Smith a Nobel Prize in Physics shared with Charles K. Kao for the invention of an imaging semiconductor circuit, the CCD sensor.

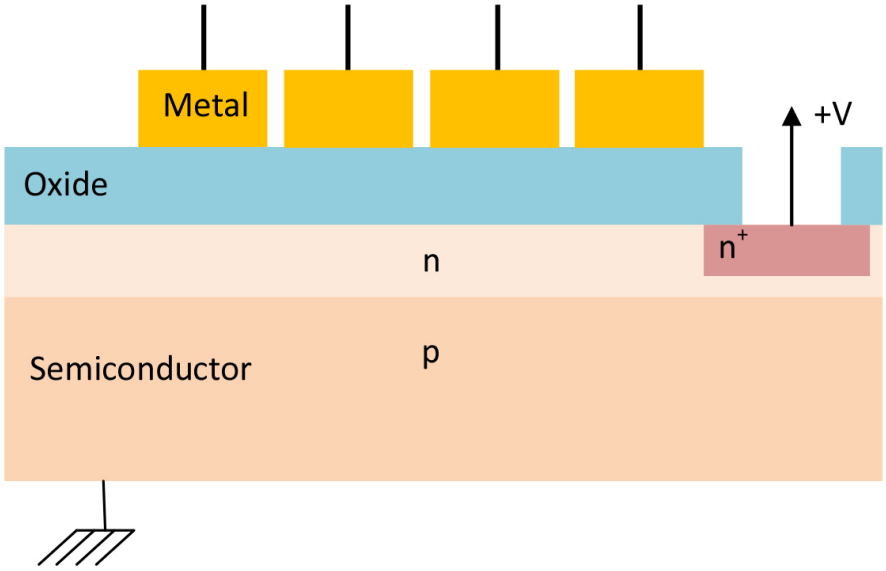

Figure 2.2: The buried channel CCD with an extra n-type semiconductor layer pushes the stored charge carriers away from the Oxide surface.

2.2 Fully depleted pnCCDs

The pnCCD is a combination of a CCD and a drift chamber specifically built to detect particles and X-ray photons. The full depletion of the substrate is achieved by asymmetric double pn-junctions on both sides of a weakly n-doped silicon substrate, figure 2.3. A highly n-doped contact on the side held at zero potential attracts the electrons from the substrate. In a silicon drift detector the stripes are held at an increasing potential in the direction of the read out anode, figure 2.5. However, in a pnCCD the potential beneath the gates is modulated with periodic potentials that defines the pixel geometry, figure 2.4. To stop the spread of charges in the direction perpendicular to the transfer direction, surface doping is increased in a stripe-like pattern. These stripes form channel guides separated by channel

stops, figure 2.6.

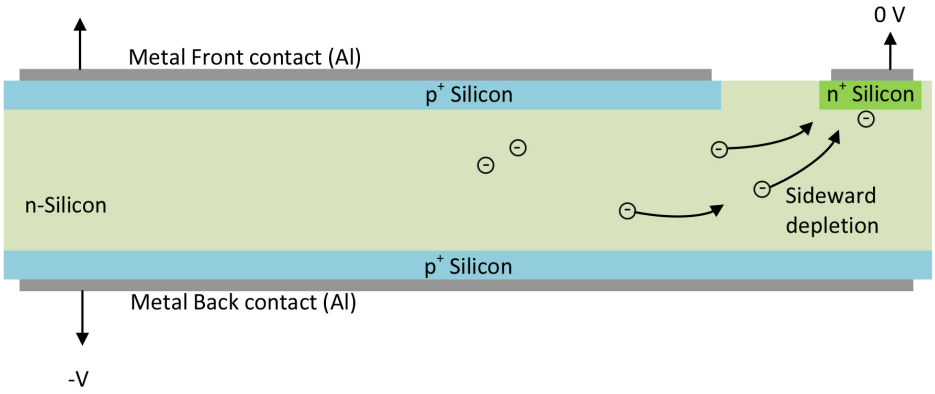

Figure 2.3: Sideward depletion concept: the green colored n-type contact held at zero potential deplete the substrate from excessive carriers and shapes the sideward depletion procedure.

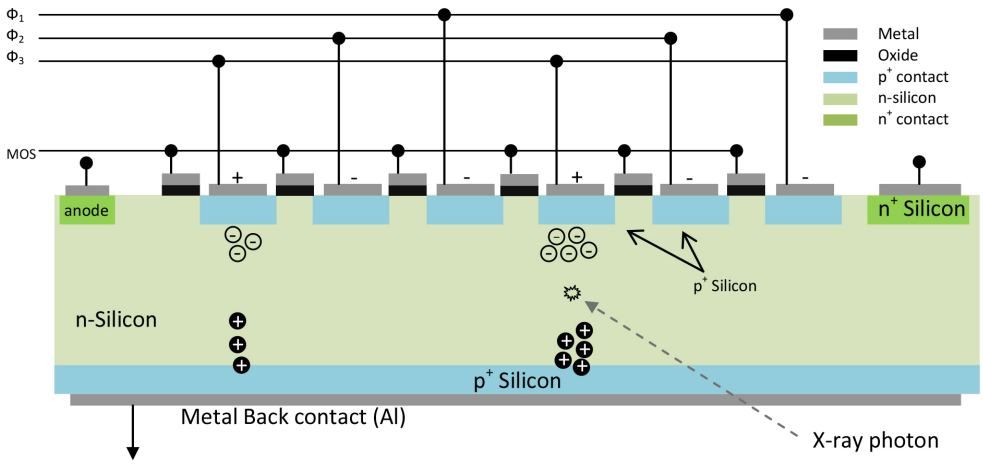

Figure 2.4: The pnCCD with the basic structural components. The MOS structure and the analogy to the drift detector is visible. X-ray photons are converted to signal charges. Full depletion allows for proportionality between photon energy and charge number. The potential of the gates is sequentially manipulated in a 3-phase cycle to transport charges in parallel to the read out anode.

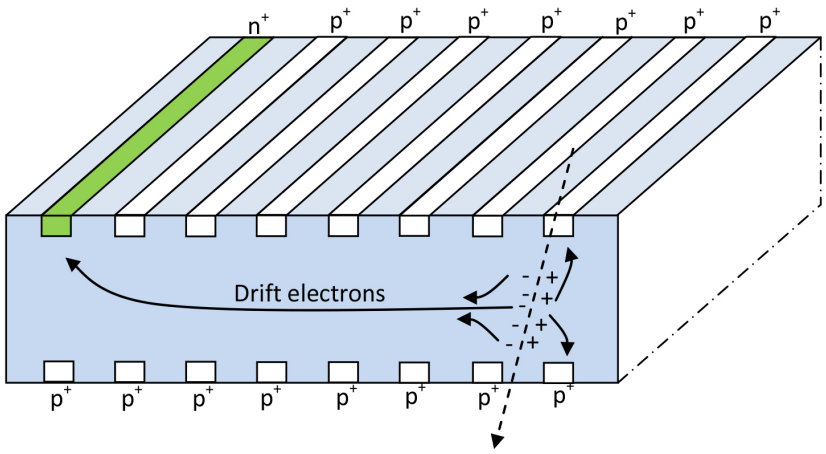

Figure 2.5: The drift detector concept forms the basis for the pnCCD. When radiations interact with the bulk material creating electrons and holes, the p^+ contact guides the electrons to the read out anode. In the pnCCD additional guides are used to pixelate the detector. See figure 2.6

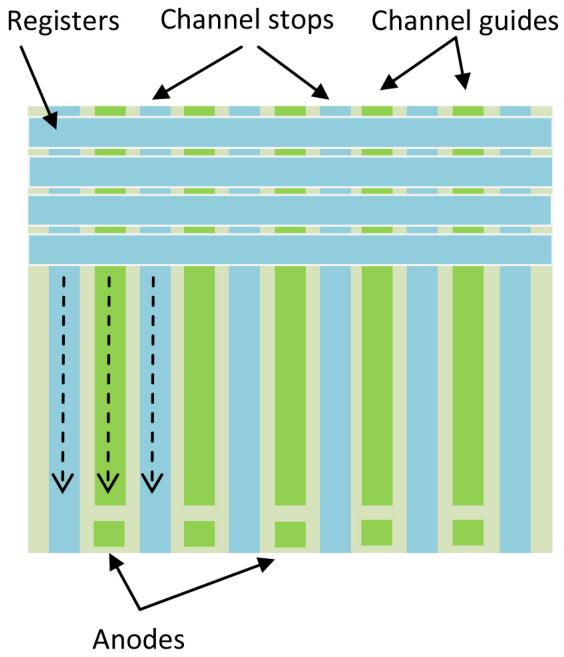

Figure 2.6: A top view of the pnCCD chip. The channel guids hold the electrons underneath the register as they are transfered from one pixel to another. The channel stops prevent the electrons charge buckets from spilling to neighboring pixels perpendicular to transfer.

2.3 X-rays detection with a pnCCD

2.3.1 Charge generation and collection

When electromagnetic radiation traverses the detector silicon bulk, they may be absorbed or scattered. The interaction probability per unit thickness of the absorber depends on the sum of the total probabilities of various absorption and scattering processes. At low photon energies, photo electric absorption is the dominating process, as shown in figure 2.7 [5]. The linear attenuation coefficient shows that the absorption is dominated by photoelectric effect up to an energy of 30 keV. At 60 keV the cross section of Compton scattering and photoelectric absorption becomes equal.

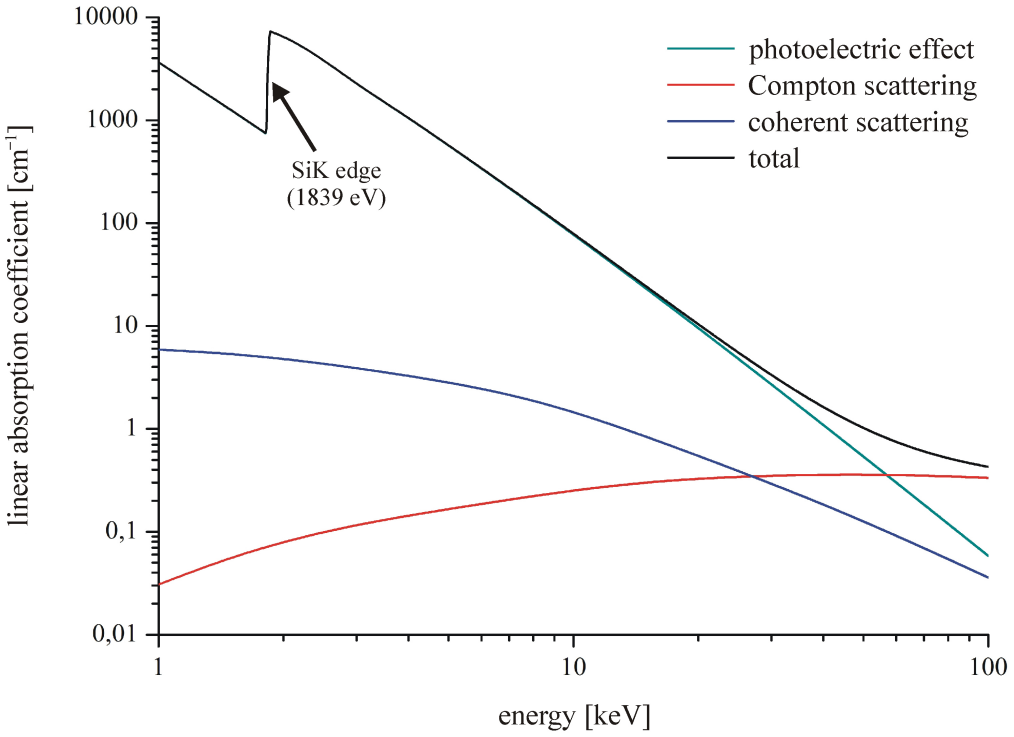

Figure 2.7: The attenuation coefficient for photons of different energies going through silicon [5].

Depending on the incident radiation energy, a number of electrons (N) are lifted from the valance band into the conduction band leaving behind an equal number

of holes. The amount of energy needed for this process is $w = 3.63$eV [6] for a Silicon crystal which is 3 times larger than the band gap at room temperature due to energy lost in phonon emissions. The number (N) of created electron-hole pairs is given by the following equation:

$$N = \frac{E}{w} \tag{2.1}$$

where E is the energy absorbed in the detector and w is the mean energy needed to create an electron-hole pair. The variance of the number (N) of elector-hole pairs created is given by 2.2.

$$\langle \Delta N^2 \rangle = F.N = F\frac{E}{\varepsilon} \tag{2.2}$$

where F is a material specific constant that measures the fluctuation in the number of ionization events (Fano factor).

The electric field across the bulk (applied externally), separates the electrons from the holes. The holes drift towards the back side whereas the electrons form a charge cloud that drifts towards the front side of the CCD. Drift and diffusion allow the charge cloud to reach the potential minima underneath the registers where it is stored. The fully depleted Silicon bulk reduces the effects of recombination and hence limits charge losses.

Electron charge clouds are stored in an epitaxial layer of few microns underneath the front side of the detector in order to prevent surface traps. A predefined setting of the registers potentials allow for the electrons to be stored underneath 1 or 2 registers from a total of 3 that define a pixel as shown in figure 2.4. Charge transfer from one register to another is accomplished by a cyclic change of registers potentials as seen in figure 2.4, until the charge stored in each pixel reaches the read out anode at the terminal of each pixel column. The initial and final charge cloud size depend on the energy of the incident photon and are explained in details in section 3.1.

The Mechanism in which the charge beneath the pixel registers flow one pixel to another depends on the temperature of the detector bulk, the number of charges and the magnitude of the registers electric potential. In summery the three processes are explained below:

- Diffusion of the electrons due to their thermal energy. $E_{thermal} \sim \frac{1}{2}kT$ where k is Boltzmann constant and T is defined as the thermal bath temperature (bulk temperature).

- Self-induced fields produced by the repelling negative charge of the electrons. This process is faster than thermal diffusion, however it is only important for large charge buckets in comparison with the pixel charge capacity.

- Fringing fields due the 3 phase transfer cycle. These fields depend on the geometry of the registers and can operate much faster than the previous two processes.

Mathematically the charge current density is a two dimensional function in space and time which is expressed as [7]:

$$j(y,t) = qD_n \frac{\delta Q_n(y,t)}{\delta y} + Q_n \mu_n E_s + Q_n \mu_n E_f \tag{2.3}$$

where q is the electron charge, D_n is the diffusion constant, Q the total charges stored underneath one register, μ the mobility of the electrons in silicon, E_s the self induced fields and E_f the fringing fields.

2.3.2 On-chip electronics

On-board electronics components such as buffer registers and current sources are specifically designed and implemented on the sensor chip in order to avoid long connections lines that decrease the signal to noise ratio. A scheme of the "On board electronics" is shown in details in figure 2.8. The most important components are the n-type Junction-gate-Field-Effect Transistor (JFET) and the Metal-Oxide-Semiconductor Field-Effect Transistor (MOSFET) used for amplification and reset of the anode charge. The charges transferred by the last register to the read out anode change the gate voltage of the JFET and therefore induce a change at the output of the first on board JFET in a form of a voltage signal. MOSFET transistor resets the anode after each read out stage, this can be a period of one frame or one pixel transfer time depending on the needs of an experiment.

The reset transistor insures that the JFET do not reach a ”latch up” stage where the gate voltage becomes largely negative so that the depletion region (in the FET) completely constricts the channel (source-Drain flow). This sufficiently negative (pinch-off voltage) is caused by an anode signal being larger than the dynamic range of the FET. Every channel of the pnCCD has its own JFET-MOSFET structure and is independent of the other ones allowing for parallel readout. F2 is the current generator of the first JFET located outside the pnCCD sensor board.
The holes that result from the elector-hole pairs drift towards the back end of the detector and become neutralized. Holes can be neglected for charge collection by the pnCCD due to the fact that their mobility is three times lower than electrons.

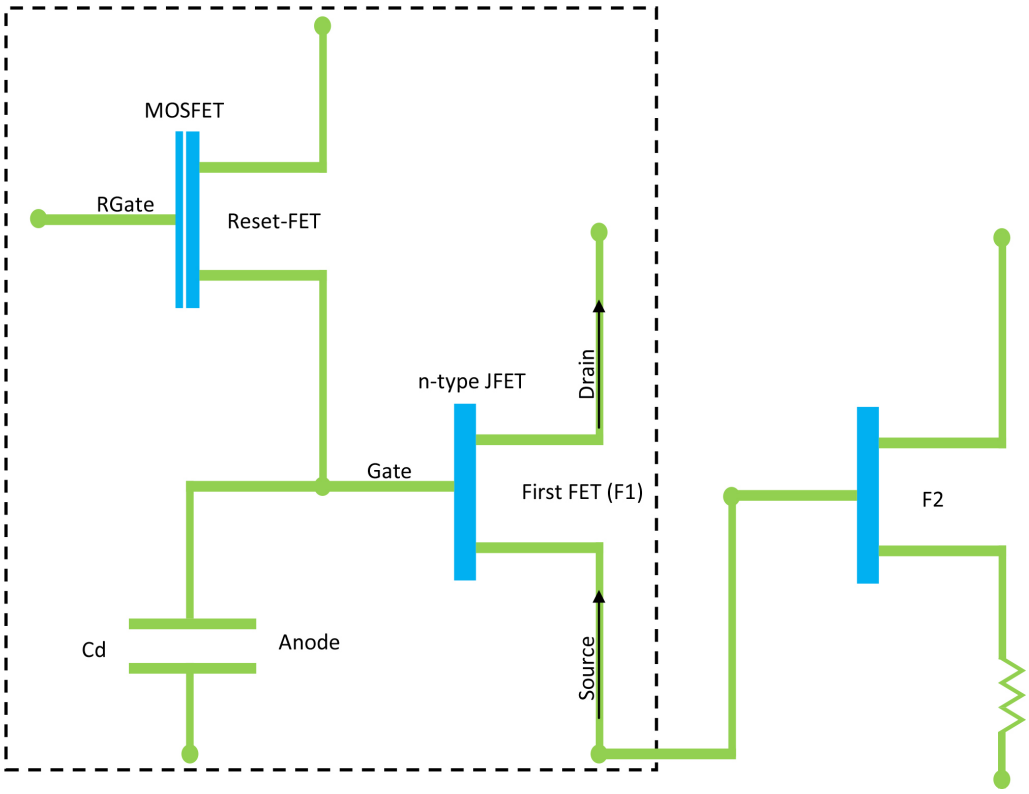

Figure 2.8: Sketch of the on-board source-follower-configuration of the readout circuit. A field effect transistor FET and the reset metal-oxide-semiconductor FET. The dashed boundary indicates the components that are present on the CCD.

2.3.3 Off-chip electronics (CAMEX)

The CAMEX 128 (CMOS Amplifier and multiplexer chip) is the off-board circuit designed for the pnCCD readout. It supplies the drive currents for the on-board electronics.
The CAMEX is based on CMOS technology and is fabricated at the Fraunhofer IMS in Duisburg, Germany. CMX 128I J is the version used for the read out of 75 x 75 μm^2 pixel size pnCCDs. The CAMEX128 is formed of 128 parallel read out channels each consisting of three main functional stages:

- **Amplification**
- **Filtering**
- **Multiplexing**

The first amplification stage is achieved through the connection of the **CSA1** amplifier to a series of feedback capacitors that are used to set the amplification gain (**SR1**). The second stage is composed of 8 multi-correlated double sampling capacitors (**MCDS**) that are utilized to filter the signal coming from the first amplifier. This is performed in two consecutive steps.
First the CAMEX is disconnected from the first FET and the base line is sampled, then the CAMEX is connected to the first FET and the anode signal is sampled (see switch states of figure 2.9). The **MCDS** capacitors are switched-on sequentially through **S1-S8** as illustrated in figure 2.9. In the third functional stage the signal from the 8 **MCDS** capacitors are integrated over the **CSA2** amplifier and delivered to a Sample & Hold capacitor (**S&H**). At the **S&H** the analogue, filtered and integrated signal waits for serialization.
A multiplexer is responsible for the serialization of all 128 CAMEX channel before the signal arrives at the 50 MHz analogue-to-digital converter **ADC**.

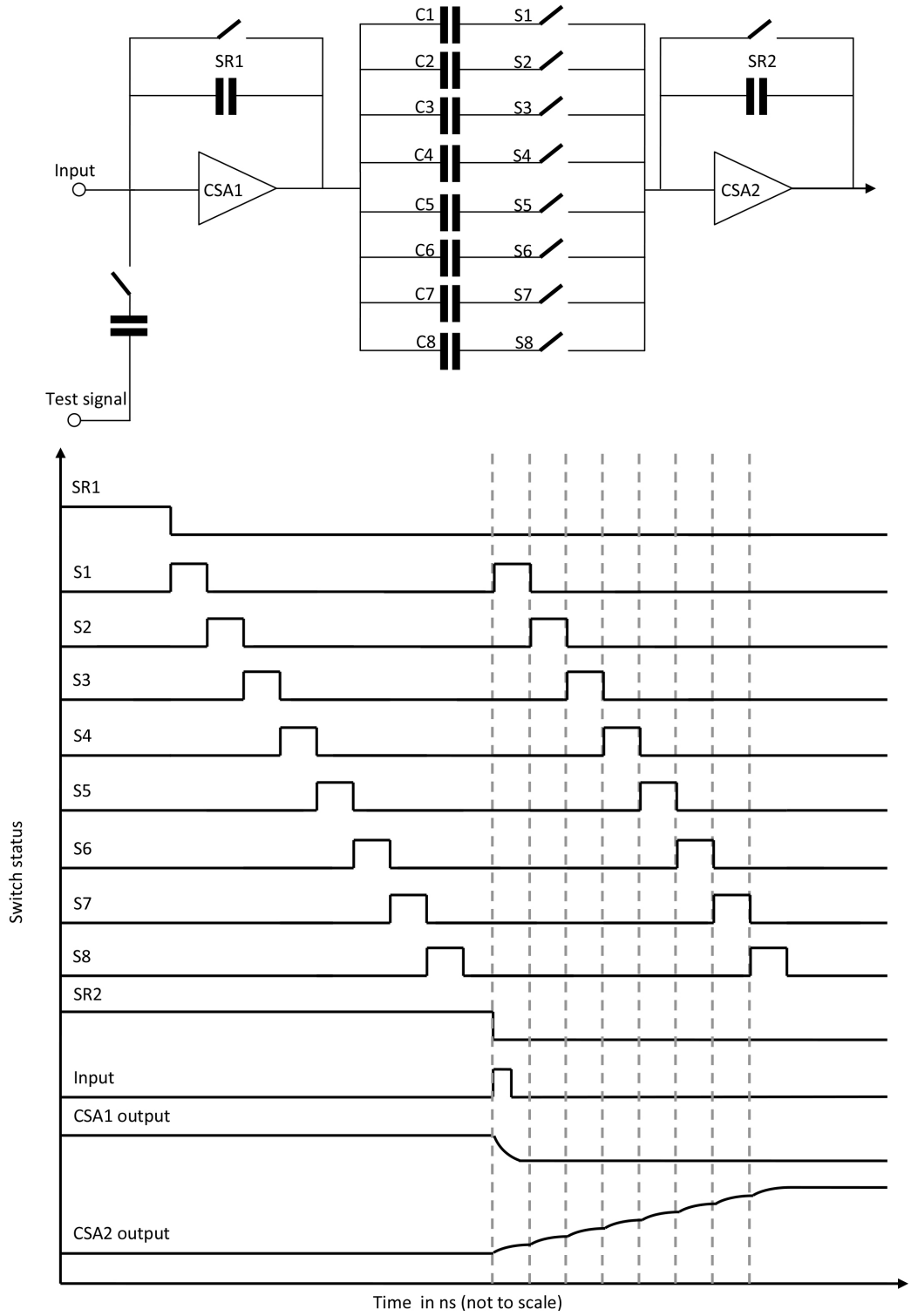

Figure 2.9: A sketch of the CAMEX128 along with the timing schematics of the readout

2.4 Physical Properties of the pnCCD

Applications of the pnCCD depend on the response of the device characteristic parameters and its performance under different experimental conditions. By characteristic parameters we mean those that affect the performance of the CCD such as energy and spatial resolution, quantum efficiency, read out frequency, dynamic range of the pixels. A better understanding of the response parameters helps to design suitable experiments and applications.

2.4.1 Spatial and energy resolution

A 2D energy dispersive detector simultaneously measures the spatial coordinates and the energy of a photon event. Spatial resolution is defined as the smallest discernible detail in an image [8]. This is determined by the smallest **pic**ture **el**ement of the CCD known as the pixel. A photon entering the detector interacts within the Silicon material and creates an electron charge cloud which is detected by one or many pixels depending on the size of the electron charge cloud. Using these pixel coordinates the photon impact position is reconstructed.

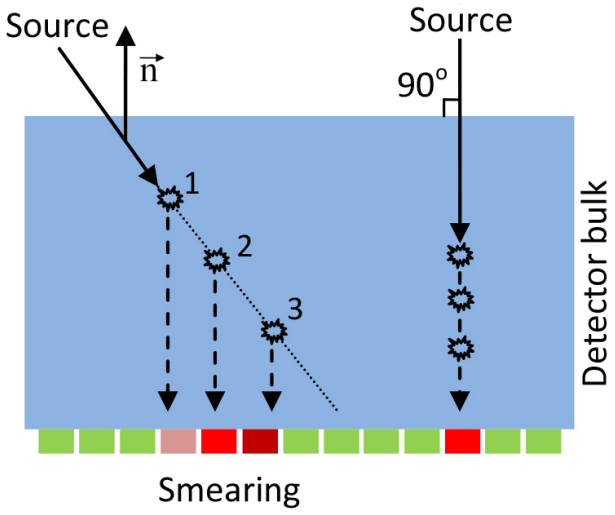

Figure 2.10: The parallax effect: photons from a source inclined with respect to the surface may interact and convert to photoelectrons along the line 1-2-3 which results in charge smearing of the object image.

In case of photons that are incident perpendicular to the detector plane, the photon impact position can be directly determined from the coordinates of the triggered pixel (pixels). In case of a very close source to the detector distance, or an oblique illumination, smearing of the image takes place as it is demonstrated in figure 2.10.
The spatial resolution improves beyond the physical size of the pixel by calculating the center of gravity of an event that spreads over more than one pixel. This method is described in details in the next section.
The energy resolution of the pnCCD is a quadratic sum of the electronic noise contribution and the statistical fluctuations of the number of ionizations in the detector material [9]. For mono-energetic X-ray photons, the full width half maximum (FWHM) of the energy spectrum (fitted with a Gaussian distribution) is a measure energy resolution and is equivilent to $FWHM = 2.35\sigma_{Gaussian}$. Mathematically this is represented as in equation 2.4.

$$FWHM(E) = 2.355w\sqrt{\frac{FE}{w} + ENC^2} \tag{2.4}$$

where **F** is the Fano factor defined as the variance of the number of ionizations, **w** is the electron-hole pair creation energy, **ENC** the Equivalent Noise Charge due to the on-board electronic circuit, the CAMEX chip and the analogue to digital converter (ADC). For Silicon the theoretical Fano factor is 0.115 while the measured one is close to 0.1 [9].
The energy resolution of the detector can be improved by reducing the contributions of the Fano noise, i.e. cooling the device to limit phonon creation. Cooling of the detector substrate also reduces leakage current contributions to ENC.

2.4.2 Counting rates and charge handling capacity

The pnCCD can operate in two different modes, the single photon counting mode "SPC" and the integration mode as demonstrated in figure 2.11.
In the single photon counting mode, individual charge clouds are separable in space and time. Separation prevents overlapping of individual signal charges in the same pixel. In a measurement, the incident flux of photons on the detector is

set by absorbers of different thicknesses such that the photon flux density do not exceed a ”threshold” value separating the SPC and the integration mode [5]. Exceeding this threshold, charge clouds formed by two or more photons will overlap in the same pixels which makes direct energy measurements impossible. If the photon flux density continues to increase, the pnCCD operates as a position resolving CCD.

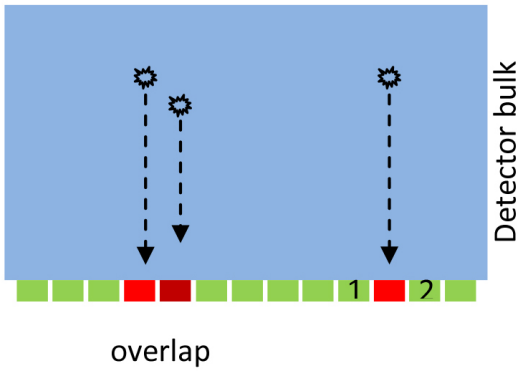

Figure 2.11: For count rates beyond a certain limit, event overlap will occur. The single-photon-counting mode intitles pixels 1 and 2 to be free if the pixel in the middle has a hit.

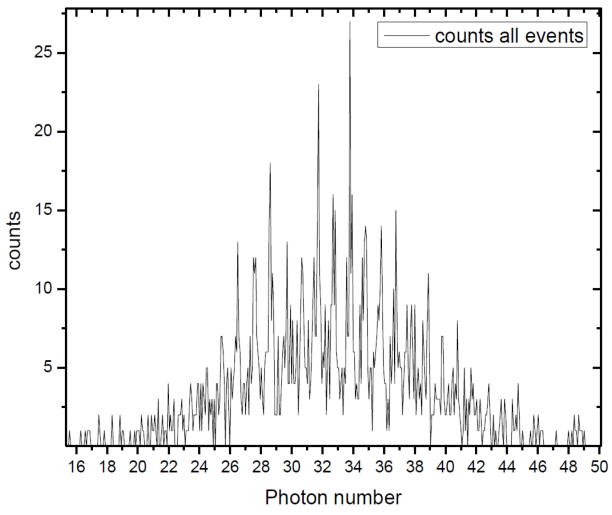

Figure 2.12: A collimated beam of 12 keV photons in one pixel with an average photon rate of 32 photons per frame will result in a pile up spectrum that follows a Poisson distribution.

For a certain photon density per pixel, where the accumulated number of charges exceeds the registers trapping potentials, the charges spread over the neighboring pixels. This phenomenon is called blooming. The maximum number of charges that can be trapped named as" full well capacity", depends on the potential of the pixel registers. For a one-register storing configuration the amount of charges is approximately 161,000 electrons corresponding to an overlap of approx 50 photons of 12 keV energy [10]. Figure 2.12 shows the results of a measurement aiming to find the maximum charge that can be deposited in a single pixel [10]. A collimated beam of 12 keV photons centered in one pixel with an average photon rate of 32 photons per frame results in a pile up spectrum that follows a Poisson distribution. Fine features of the distribution show that separating one spectrum spike to another is a distance of 1 photon.

2.4.3 Quantum efficiency

The quantum efficiency (QE) of a CCD detector defines its response to different photons wavelengths. Photoelectric effect dominates the processes by which photons are converted into electrons in Silicon up to 30 keV. For a beam of mono energetic photons of intensity I_0 penetrating a layer of material of thickness x and density ρ, the number of photo electric converted photons (N_{pe}) is defined by:

$$N_{pe} = I_0 \left[1 - exp(-\mu\rho x)\right] \tag{2.5}$$

where $\mu(Z, E)$ is the linear attention coefficient.[1]
As the energy of the photon increases, theQE decreases as Compton effect becomes the dominating process of interaction in Silicon.
Figure 2.13 represents the simulated curve of the quantum efficiency of a pnCCD equipped with an optical and UV blocking filter. Between 1 and 10 keV the quantum efficiency is close to 1. Absorption edges of air elements (Nitrogen, Oxygen) are visible together with the Aluminum edge of the secondary optical shielding material.

[1] ICRU (1980), Radiation Quantities and Units, Report 33 of the International Commission on Radiation Units and Measurements (Bethesda, MD).

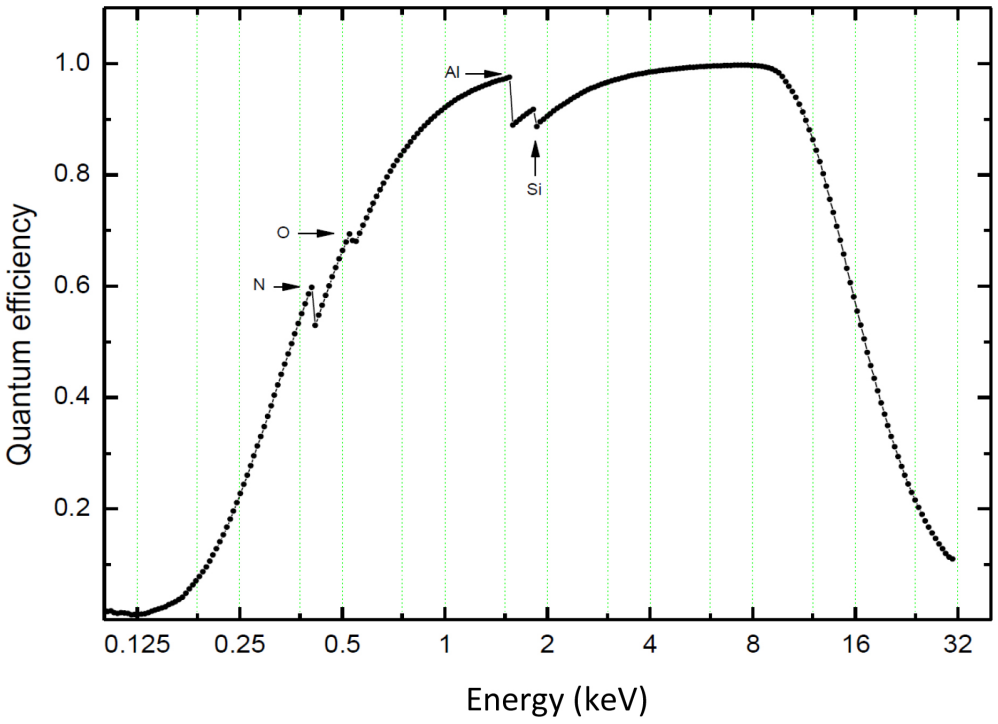

Figure 2.13: The simulated quantum efficiency spectrum for the pnCCD. Absorption edges for some materials of oxygen, nitrogen, aluminum, and silicon possibly a result of a contaminated entrance window of the detector housing.

2.4.4 Readout frequency and the burst mode

The pnCCD detector operates in two different modes: the full-frame and the frame-store mode. In the full-frame mode, the total area of the CCD is exposed to X-rays. This is used in applications where the incident photon flux on the CCD is low, i.e. space imaging and astronomy. Whereas in the frame-store mode half the detector area is shielded by a Copper sheet that prevents all photons to reach the CCD, figure 2.14. The frame store mode allows for the signal to be integrated in the frame area and followed by a quick transfer (900 ns/pixel)[2] to the shielded area where it is read slowly by the CAMEX chip (28 µs/pixel)[3].

[2]In standard operation mode
[3]In standard operation mode

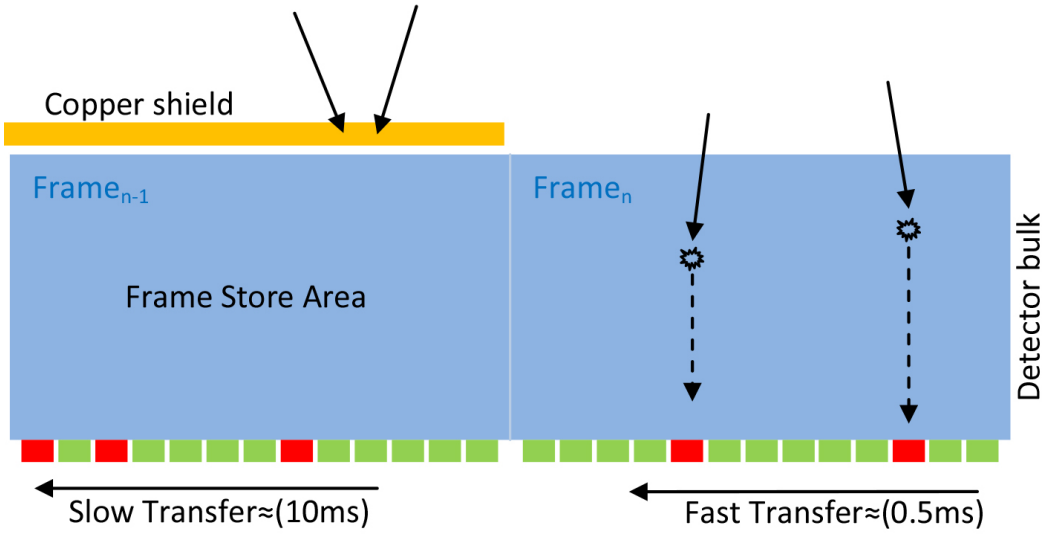

Figure 2.14: A sketch of the detector in the frame store mode. A copper shield prevents incoming photons that disturbs the slow read out by the CAMEX

The advantages of the frame store mode is to reduce out-of-time events, however it also reduces the active area of the detector by one half. In frame store mode the readout frequency is the sum of the transfer time to the frame store area and the readout time by the CAMEX chip. Both quantities depend on the number of pixels and the CAMEX settings and are given by:

$$Frequency(Hz) = 1/(t_{transfer} + t_{readout}) * (N_{pixels}) \tag{2.6}$$

The read out frequency can be increased my reducing the number of read out pixels. This can be done virtually in a special operation **burst mode**. The burst mode reduces the number of pixels read at each frame cycle. This is achieved through summing up the pixel signal values at the terminal anode, see figure 2.15 (a, b). Read out of the anode charge is performed after the transfer of 2, 4, or 8 (**binning factors**) rows of pixels, hence the CAMEX would only process 1/2, 1/4 and 1/8 of the total number of pixels respectively. The result is an increase in the readout frequency by a factor of 2, 4 and 8 respectively. By summing up pixels, the position resolution is degraded along the transfer direction. The degradation is again the binning factor (2, 4 or 8). For example a 128 x 128 pixels detector area is reduced into a 64 x 128, 32 x 128 or 16 x 128, figure 2.15 (c, d). The

measurement in figure 2.15 (c, d) is a diffraction signal measured in the home lab using a Copper radiation X-ray tube and is used to demonstrate the burst mode principle. Table 2.1 shows the frequencies that can be reached when the CAMEX is over-clocked and in case the burst mode is used. Depending on the application requirements, the detector readout frequency is selected.

Operation mode	nb	nb	nb	nb	nb	2x	4x	8x	16x
Frequency (*Hz*)	170	294	340	380	430	370	700	1250	2000
Cycle time (*ms*)	5.2	3.4	3	2.6	2.3	2.7	1.4	0.8	0.5
Niose (*ENC*)	8.2	8.8	11.2	22.2	24	9.7	9.6	9.65	9.53
FWHM (Cuk_{α})	207	262	292	409	422	212	206	204	206
CTI (x10^{-6})	30	24	23	29	38	42	57.7	78	82.8

Table 2.1: Cycle times achieved with operation in the standard mode (nb: no binning) for 170 Hz and higher frequencies through over-clocking the CAMEX. In comparison, the burst mode operation mode is shown with the diferences in FWHM, Noise and CTI values.

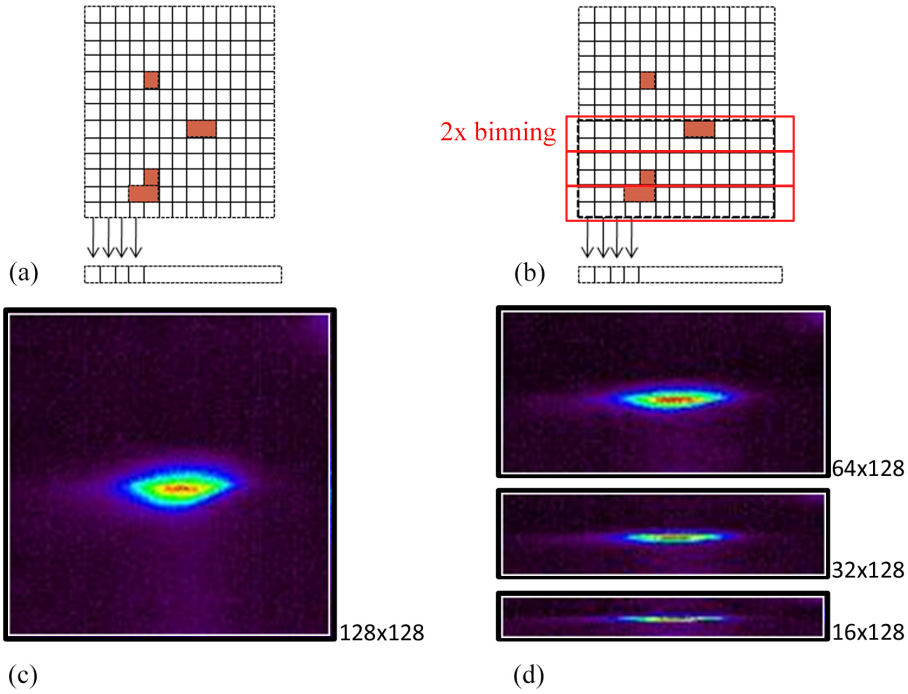

Figure 2.15: A sketch of the detector in the frame store mode. A copper shield prevents incoming photons that disturbs the slow read out by the CAMEX.

Chapter 3

Beyond the pixel borders

Many applications require a spatial resolution better than the pixel size of a CCD sensor. Examples are:

- Position resolved x-ray fluorescence.
- High resolution medical imaging.
- High resolution space imaging.
- Micro Laue X-ray diffraction.

For Laue diffraction, the experiment depends on the accuracy to measure the energy and the angle of the diffracted beam of photons i.e. the wave vector k_1 [5] [11]. The enhancement of the spatial resolution can be done by decreasing the device physical pixel size. However, this is not always be a solution due to the resulting degradation in the signal to noise ratio. Figure 3.1 illustrates the effect of the reduction of pixel size and the affect on the signal to noise ratio.
The alternative is to use software algorithms that reconstruct the sub-pixel position of an event. In this part of the thesis, the center of gravity technique (CG) will be applied to restore the position of the photons impact coordinates with sub-pixel resolution. In order to achieve this aim, the charge cloud dynamics in the detector bulk are studied, and the charge cloud size at the time of charge collection by the pixel is interpolated by combining numerical simulations and experimental results. The shape of the charge cloud is approximated by circular disk in the

pixel plane with a rectangular density profile. The approximations made for the shape and size are tested by a transmission contrast imaging experiment.

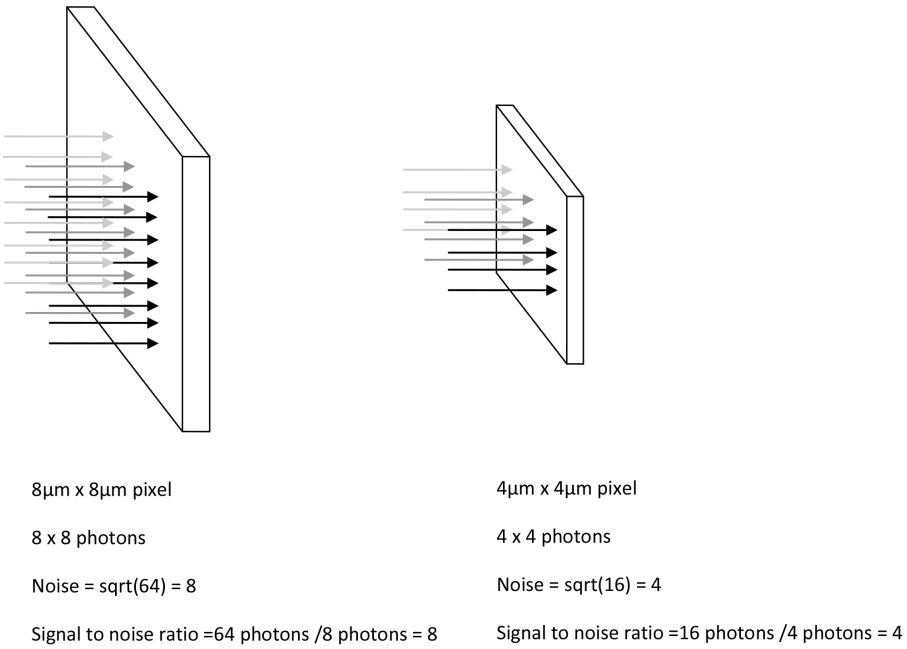

Figure 3.1: An example of the noise created when the pixel size is decreased by half.

3.1 Measurement of the charge cloud size

Electrons are formed when an X-ray photon is absorbed in the silicon bulk of the detector. Depending on the energy of the photon, a charge cloud of a certain size and shape is created. Electric fields push the charge cloud towards the pixel area where the landing position of the charge cloud is completely random. In the optimal case, the complete charge cloud is collected by one pixel. If the charge cloud center is close to the pixel borders, the charges spill over to the adjacent pixels forming a split-event (type) and an event-pattern (shape). However, the charge cloud size and the X-ray event pattern are coupled together. If the pattern is determined then the size of the charge cloud size can be deduced. In the past the so-called mesh experiment introduced in 1997 by Tsunemi [12] was used to investigate the single photon response inside a CCD and subsequently its spatial

resolution. The technique makes use of a gold mesh with 5 μm holes which is placed close to the CCD surface. The mesh allows for the precise knowledge of the landing position of the photons on the detector surface. A schematic of the technique setup is shown in figure 3.2 [12]. The setup consists of an X-ray source placed at a far distance from a CCD camera in order to achieve normal incident beam on the camera. The CCD camera is coupled to a metal mesh with a series of equidistant holes. The mesh is slightly rotated parallel to the CCD such that its holes cover different areas over the pixels. A formal discribtion of the method is discussed in [12] and [13].

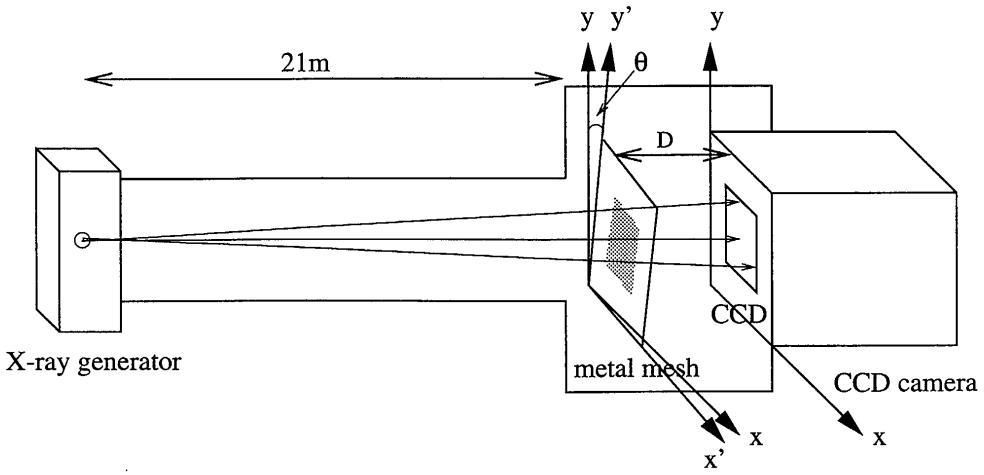

Figure 3.2: A schematic view of the mesh experiment. The X-ray generator produces a parallel beam at 21 meters from the mesh. The aim of the mesh to identify the position of the incident photons independent from the CCD readings.

However the mesh technique suffered from a few drawbacks [12].

- The mesh creates a blurred images for sources that are close to the detector.
- To reduced the blurring the X-ray source is placed 21 m away from the mesh.
- This reduces the intensity which in turn increases the measurement time and decreases the stability of the setup.

- The resolution of the mesh depends on the holes size. The minimum size of the holes depend on the thickness of the mesh and the fabrication material. To investigate high energy photons (above 10 keV) a material with high atomic number must be used. For photons 10 keV and above, the mesh procedure can not be used.

In this part of the thesis, a detailed description of an alternative method to measure the charge cloud size is introduced. The advantages over the mesh experiment is highlighted by the simplicity of the setup and the possibility to measure the charge cloud size created by photons in a wide energy range (1-30 keV). The method developed is based on the assumption that *"on average a charge cloud created by mono energetic photons will always produce the same branching ratios of event pattern shapes when landing on a CCD of defined pixel size"*. In order to realize the task the following steps were carried out.

- **First:** A spectroscopic fluorescence experiment is performed in which metal targets are illuminated with synchrotron radiation. The monochromatic fluorescence radiation creates split events in the detector. The split events are grouped depending on their shape. For every metal target, photons of the K or L radiation lines are selected and the percentage of single, double, triple and quadruple events are extracted (see figure 3.7), which result in a correlation between the photon energy with the event splits distribution. Experimental details are described in the following parts.

- **Second:** A Monte Carlo simulation is performed. The input is a square pixel and a disk-projection of a charge cloud on this pixel. The radius of the disk is fixed and the center of the disk is randomly generated. Depending on the radius of the charge cloud, the disk lay completely in one pixel, or is shared between 2, 3, or 4 pixels, the result is a correlation between the charge cloud radius with the event splits distribution.

- **Third:** The results of the experiment and the simulation are combined and a relation between the energy of a photon and its charge cloud radius is found. The organization of the method traces backward through the flow chart of figure 3.3.

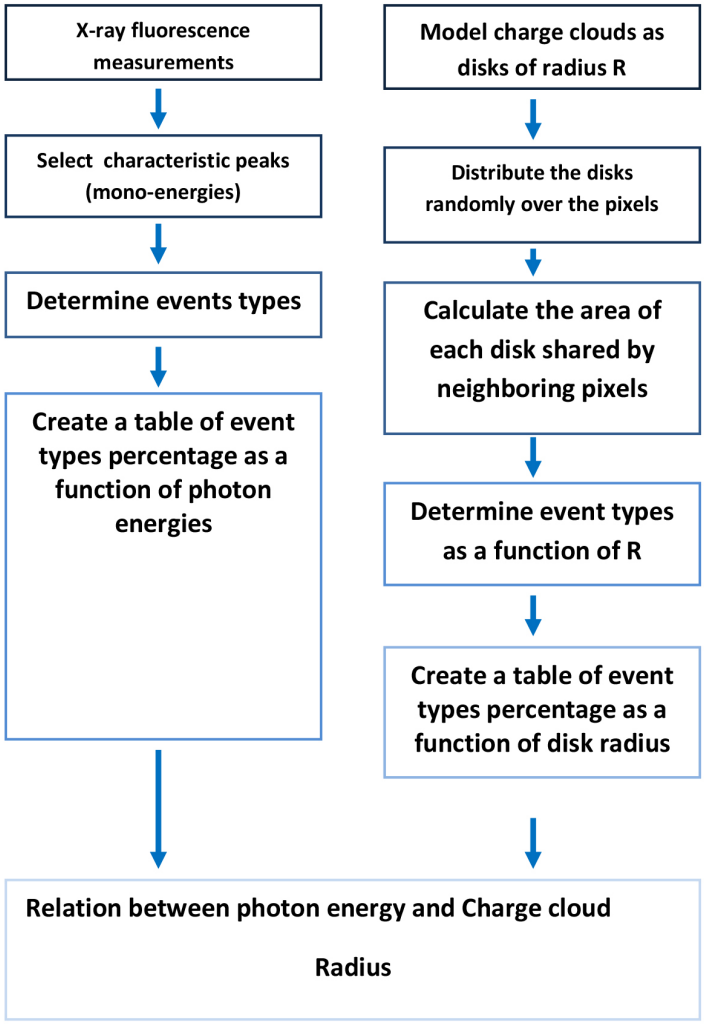

Figure 3.3: Flow chart for the procedure used to extract charge cloud sizes. The left hand side underlines the experiment steps, while the right side describes the steps of the modeling part.

3.1.1 Size and shape of the charge cloud

Charge clouds of electrons created after the interaction of photons with the detector bulk are described by their shape and size. After the first ionization process the created electrons follow a chaotic track in the bulk material as a result of a series of elastic and inelastic collisions. The resulting initial charge cloud has a

shape and size which is determined by the track length of electrons in silicon. Up to 30 keV the electrons track length is less than 10 μm. A plot of the average path length traveled by an electron in Silicon as it slows down to rest (CSDA range) is shown in figure 3.4 [14]. From the CSDA values, the linear range of electrons in silicon is plotted as a function of energy. Since the travel range up to 30 keV is much smaller than the thickness of the detector (450 μm), the charge cloud shape can be modeled by a spherical approximation [15]. The size of the initial charge cloud is also energy dependent [16] and is given by 3.1:

$$\sigma(nm) = 0.0044(E_e)^{1.75}\mu m \tag{3.1}$$

where $E_e = E_{photon}$ is the energy of the electron in keV, or $E_e = E_{photon} - E_{Si}(k_\alpha)$ in case of a k_α fluorescence photon escapes.

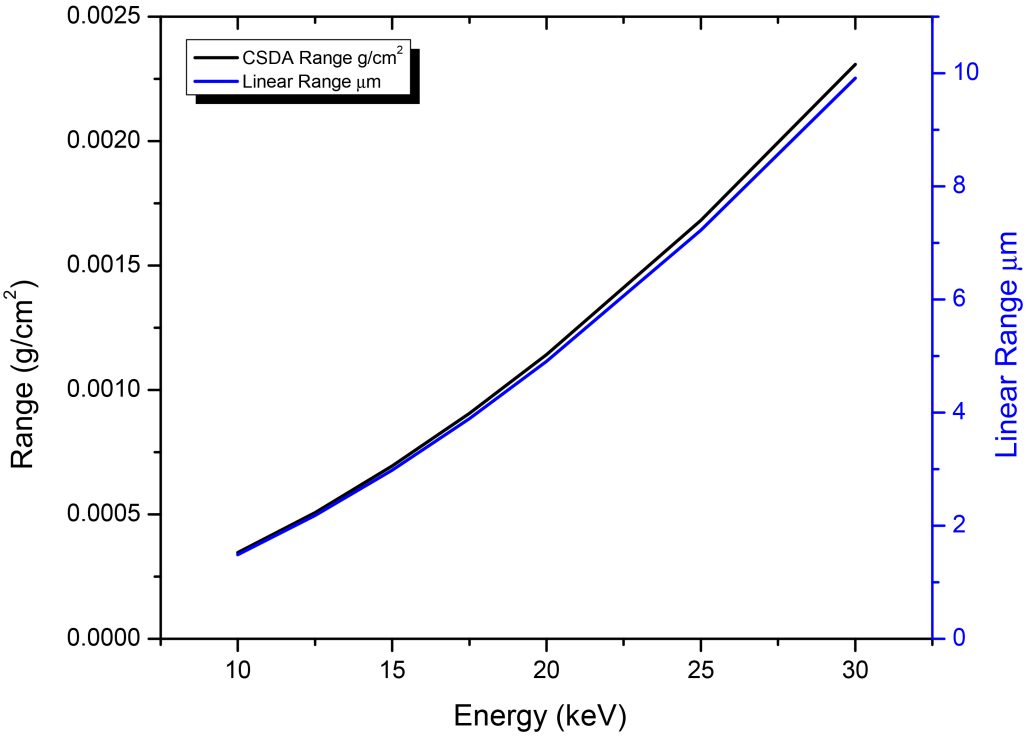

Figure 3.4: CSDA or continuous-slowing-down-approximation is an approximation to the average path length traveled by charged particles as they slow down. The travel range for the created electrons of energy below 30 keV *is significantly less than the 450 μm depletion length of the detector*

The initial charges experience an external electric field in the detector. This field is applied to deplete the bulk from free charge carriers. As the charge cloud travel from the creation point to the collection point it expands. The addition to the initial radius is given by [17]:

$$r_d = \sqrt{\frac{2KT\epsilon_s}{e^2 N_a} \ln\left(\frac{z_d + \epsilon}{z_d - z + \epsilon}\right)} \tag{3.2}$$

where z_d is the detector depleted region depth, z is the depth of interaction of the incoming X-ray photon, N_a doping concentration in the depletion region equivalent to $6x10^{11}cm^{-3}$, ϵ_s is the silicon permittivity, equal to $1.044x10^{-12}Fcm^{-1}$, k_B is the Boltzmann constant, T is the detector temperature $-60°$C and ϵ is a factor added to avoid singularity. The function in equation 3.2 is plotted in figure 3.5. The mean radius of the generated charge cloud increases with the photon energy. At same time the FWHM of the distribution increases. From the right hand slope of the distribution, r_d is energy dependent.

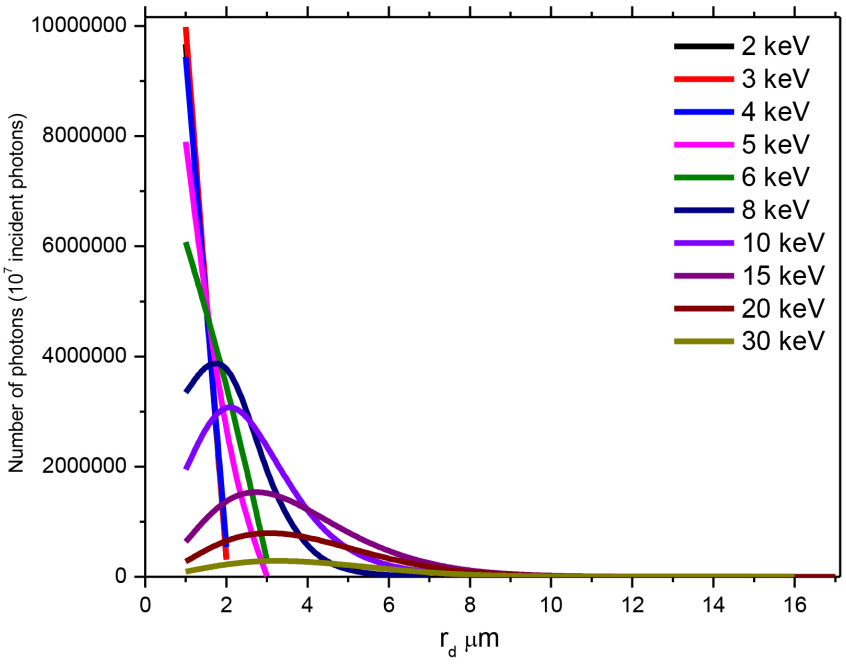

Figure 3.5: In the depletion region where the charges are under the influence of the electric field, the radius of the charge cloud increases as it drifts towards the pixels. This increase r_d depends on the energy of the photon. As an example, a 10 keV *photon (charge cloud) expands by up to 10* µm.

Moreover, z depends on the linear attenuation factor, which in turn is energy dependent. Equation 3.3 relates the depth of interaction of the incoming X-ray photon to the attenuation coefficient according to:

$$z = -\frac{1}{\mu_z(E)} \ln(P + \epsilon) \tag{3.3}$$

where $\mu_z(E)$ is linear attenuation coefficient and P a random number between 0 and 1 standing for the ratio between the photons that traversed the detector without interacting (I) and the incident flux (I_0). ϵ is an offset to avoid singularity when P=0. In figure 3.6 the depth of interaction for a sample of 10 million photons is plotted as a function of photon energy. It can be seen that up to 30 keV the penetration depth does not exceed the 450 μm thickness of the detector.

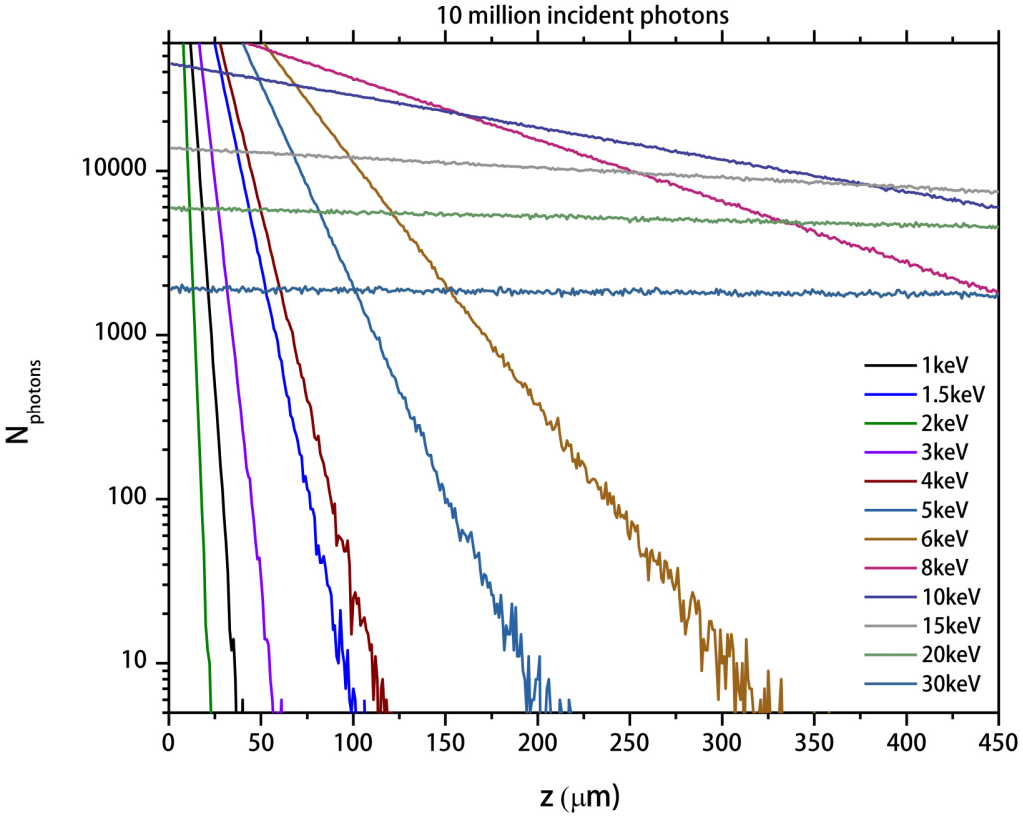

Figure 3.6: The depth of interaction of the incident X-ray photons (z) changes as a function of energy. For 1-6 keV *all photons interact in the detector's 450 μm depletion layer. For 10* keV *and above the number of photons interacting in the detector decreases.*

Depending on the relative center of the charge cloud with respect to the pixel boundaries, the charges of the respective electron clouds are collected by either 1 pixel (single), two pixels (doubles), three (triples) or four (quadruples) pixels. Since the final charge cloud size is smaller than the pixel size (75 µm) no additional split events are possible. Singles, left and right doubles, up and down doubles, four types of triples and four types of quadruples result in 13 possible event patterns types, figure 3.7.

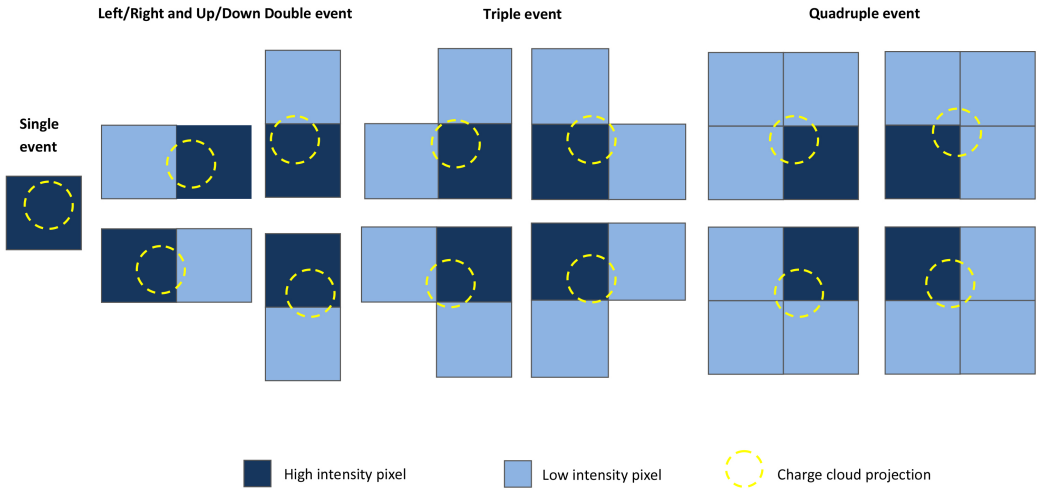

Figure 3.7: Thirteen event types that are accepted as real events. Any other pattern that do not lay within these types is rejected by software.

Any split arrangements other than the 13 represented above are considered as cluster events and are rejected when data analysis is performed. For split events, the shared charges are summed up and assigned to the pixel with the highest charge value.

3.1.2 Experimental determination of event split distributions

The X-ray fluorescence spectroscopy experiment is performed using the pnCCD detector at the Energy Dispersive Reflectometry (EDR) beam line of BESSY II. A sketch of the beam-line layout is shown in figure 3.9[1].

[1] http://dokumentix.ub.uni-siegen.de/opus/volltexte/2009/394/

Located at a bending magnet (E = 1.7 GeV, B = 0.95 T), the distance between source and sample is about 30 m. Except slits and vacuum windows, no optical elements are placed between source and sample. Owing to the critical energy of the BESSY II ring of approximately 1.8 keV and the strong absorption of low-energy X-rays in air, the incident-beam spectrum outside the vacuum chambers appears as a glow-like curve with onset at about 5 keV and maximum flux at about 13 keV followed by an exponential decay towards higher energies. In total the incident-beam spectrum provides photon fluxes between 5 keV and about 45 keV with an integrated flux of about 10^{10}photons/s into an area of 0.2 x 1 mm^2 measured through an air pass of about 1 m.

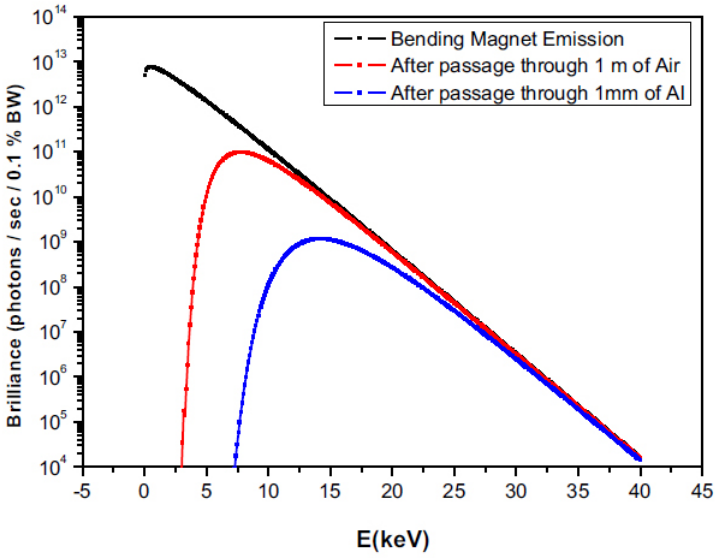

Figure 3.8: Emissions from the bending magnet at BESSY II calculated with XOP [18].

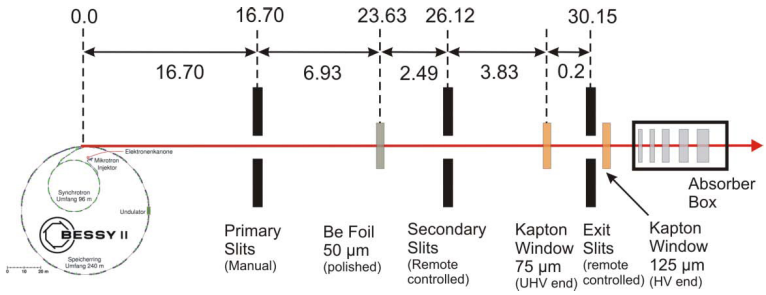

Figure 3.9: Layout of the EDR beam-line. The distances are all in SI unit (meter) [18].

The pnCCD detector used for this experiment is an eROSITA system made up of 16384 pixels spread over a squared array of 92.16 mm^2. The square pixels have a side length of 75 μm. The detector is operated in frame store mode, with one part shielded from radiation. 100 frames are collected every second.
Five metal sheets (Fe, Cu, Rb, Pb, and Mo) are illuminated by synchrotron X-rays of energy between 5 and 40 keV to produce fluorescence light. In table 3.1 the energies of interest are listed. For Fe, Cu, Rb, Mo the $K\alpha_1$ energy characteristic lines were used whereas for Pb the $L\alpha_1$ characteristic line was used since the detector QE ar $K\alpha_1$ characteristic energy (66.8 keV) is negligible .

Element	Fe	Cu	Pb	Rb	Mo
E (keV)	6.403	8.047	10.551	13.395	17.479
Attenuation length (μm)	35	70	156	316	670

Table 3.1: The 5 elements used in the experiment. The magnitude of the energies used in the analysis is shown along with the attenuation of the photons in Silicon.

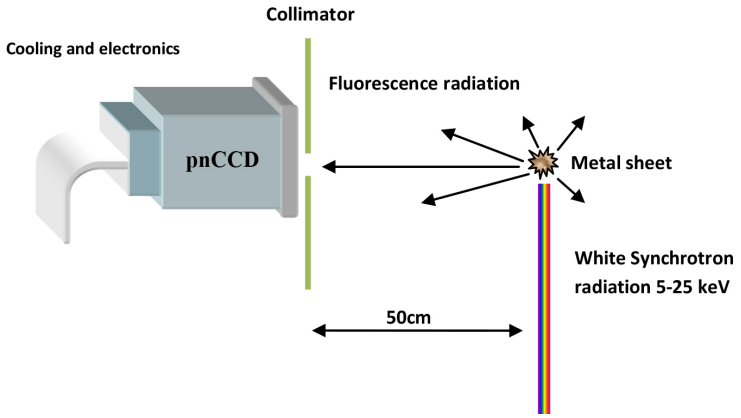

Figure 3.10: A schematic view of the experimental setup at the EDR beam line of BESSY II.

The detector was placed at a distance of 50 cm upstream from the sample at a scattering angle of 90° with respect to the incident beam. In total 10,000 frames are recorded in the single photon counting mode for every metal sheet, figure 3.10. The noise threshold is set to $4\sigma_{noise}$, where σ_{noise} is the standard deviation of the total noise calculated from a set of 300 dark frames (no exposure) recorded at

the beginning of the each measurement. To select the noise threshold magnitude, an analysis of the shape of the Cu ($K\alpha_1$) line is performed and discussed in the following section.

The event type distribution is sensitive to the noise threshold selected by the operator, figure 3.11. To quantify the event noise threshold, the response of the energy spectrum of the Cu ($K\alpha_1$) line to a range of thresholds is investigated. In case of a wrong threshold value, the energy profile deviates from a Gaussian distribution. In fact there is a systematic shift of the energy spectrum to lower values where the shift magnitude increases when increasing the noise threshold, figure 3.12. In other words, the χ^2 value which is defined as the magnitude of discrepancy between the measured spectra and a Gaussian distribution is quantified. The closer χ^2 to 1 the better is the fit and hence the more accurate is the selection of the noise threshold. χ^2 is calculated using equation 3.4.

$$\chi^2 = 1 - \sum_{Energy} \frac{(I_{meas}(E) - I_{Gauss}(E))^2}{I_{Gauss}(E)} \tag{3.4}$$

where I_{meas} is the measured intensity as a function of energy and I_{Gauss} is the fitted model distribution. Figure 3.11 is an example of the effect of the noise threshold. In (a) is a central hot pixel (an event) that contains a signal amplitude of 730 arbitrary units. The surrounding pixels are at a lower signal value. If the noise threshold is set to be ($4\sigma = 40$ then the event is labeled as a **single** event (b). If the noise threshold is set to be ($4\sigma = 30$) then the event is a **double** event with an amplitude of 730+31 (c).

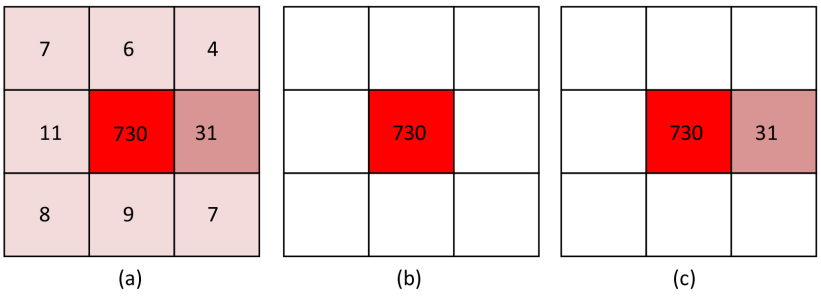

Figure 3.11: (a) An event of 730 a.d.u. (b) Cut off in the case of a hight threshold > 31 a.d.u. (c) In case of a lower threshold <30 (a.d.u.).

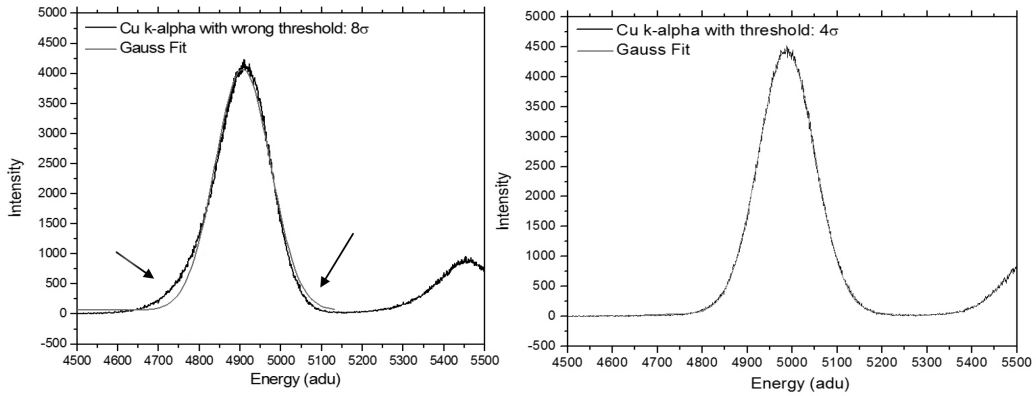

Figure 3.12: Gaussian fit of one spectrum with two different noise thresholds 4σ*(right image) and* 8σ*(left image).*

The results are listed in table 3.2. The spectra of the fluorescence lines of all metals were analyzed using a $4\sigma_{noise}$ threshold, table 3.3.
From the results summarized in table 3.2, $4\sigma_{noise}$ is selected to be the noise threshold in further event analysis procedures.

Threshold	Singles%	Doubles%	triples%	Quadruples%	χ^2
$1\sigma_{noise}$	4.55	36.69	39.39	19.36	0.99806
$2\sigma_{noise}$	8.84	46.63	27.53	17.00	0.99852
$3\sigma_{noise}$	15.47	51.589	17.66	15.28	0.99890
$4\sigma_{noise}$	20.98	52.36	13.31	13.35	0.99938
$5\sigma_{noise}$	24.42	52.25	11.54	11.78	0.99906
$6\sigma_{noise}$	26.72	52.06	10.67	10.54	0.99787
$7\sigma_{noise}$	28.57	51.88	10.03	9.52	0.99594
$8\sigma_{noise}$	30.21	51.59	9.51	8.68	0.99285

Table 3.2: The effect of using different thresholds on the event type distribution. The χ^2 *value is used to estimate the goodness of the Gaussian fit to the energy spectrum of Cu* K_α.

Energy(keV)	Singles٪	Doubles٪	triples٪	Quadruples٪
Fe $K\alpha_{1,2}$: 6.403	23.10	52.68	12.10	12.12
Cu $K\alpha_{1,2}$: 8.040	20.98	52.36	13.31	13.35
Pb $L\alpha_{1,2}$: 10.551	19.27	52.28	14.55	13.89
Rb $K\alpha_{1,2}$: 13.395	15.64	52.60	17.18	14.58
Mo $K\alpha_{1,2}$: 17.479	7.34	53.54	23.35	15.77

Table 3.3: The experimental results of the event type splitting distributions over single, double, triple and quadruple events as a function of energy.

For every data recorded, the branching ratios as a function of energy is obtained. The results are presented in table 3.3 where singles and triples events show a direct correlation with the energy while Quadruples and doubles show a weaker dependence. For this reason, single type events distribution are used as a direct identification of the energy magnitude. The next step is to calculate the split distribution for a list of different charge cloud radii, based on a model describing the charge cloud shape and density

3.1.3 Correlation between charge cloud size and event split distribution

Just before the collection of the charge cloud electrons by the electric potentials of the pixels, the charge cloud is assumed to have a radius ${\sigma_{radius}}^2$. On the other hand, the density distribution of the electrons in the cloud is Gaussian type of equation 3.5. However, for simplicity it can be approximated by a rectangular distribution 3.6 according to the work of Yoshita [19].
Gaussian model:

$$S_{Gauss}(\sigma_{radius}, X) = \frac{1}{\sqrt{2\pi}\sigma_{radius}} \exp(\frac{-X^2}{2\sigma^2_{radius}}) \tag{3.5}$$

[2]Note σ_{radius} is different from σ_{noise} described before.

Rectangular model:

$$S_{Rectangular}(\sigma_{radius}, X) = \begin{cases} \frac{1}{6\sigma_{radius}}, & \mid X \mid < 3\sigma_{radius} \\ 0, & \mid X \mid > 3\sigma_{radius} \end{cases} \tag{3.6}$$

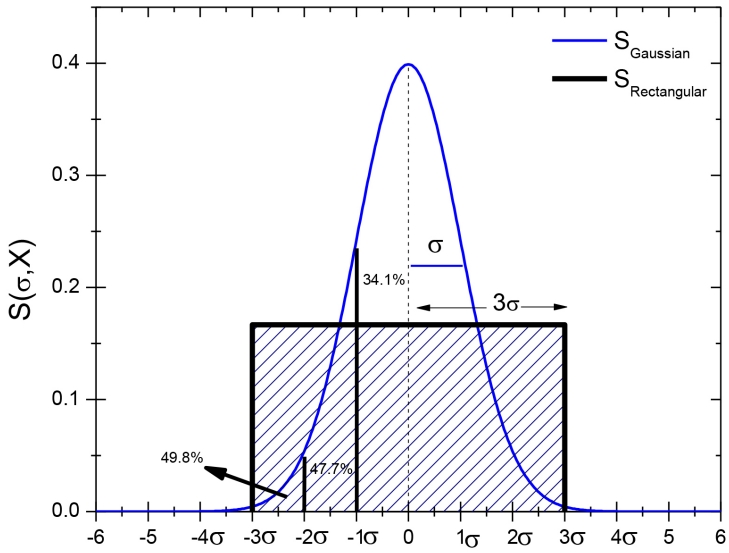

Figure 3.13: Comparison between the two models: Rectangular and Gaussian. The radius in the first is assumed to be equal three times the second model. In both cases the total number of charges is normalized to unity.

Since the integral of $S(\sigma_{radius}, X)$ for both models is normalized to unity, one can define the half width of the rectangular model to be R=$3\sigma_{radius}$, considering that the total charge within the rectangle hosts 99.7% of charges stored by a Gaussian of same radius σ_{radius} as seen in figure 3.13.

The projection of the spherical shaped charge cloud into the pixel plan resembles a disk with radius R having a rectangular charge density profile. Simulated pixels are squares in shaped with side length of value 1. The charge cloud projects on the pixel planes into a disk shape with a radius R. The landing position of the charge cloud, the center of the disk (X_x, Y_c) is random and R is varied between zero and 0.5 (figure 3.14). Depending on magnitude of the disk radius R, a relation with the type distribution is determined and shown in figure 3.15.

To explain the data in figure 3.15 it is necessary to examine figure 3.16 which

represents the locus of the center of a charge cloud landing position for different event types (3.16(a)). For many events with a charge cloud R, when the center (X_c, Y_c) is within the red shaded area, the charge cloud would be entirely collected by one pixel. However, if the center is within the green, blue and white respectively, the charge cloud splits at the pixel boarders (by the register electric potentials) and hence double, triple and quadruple events are formed, respectively.

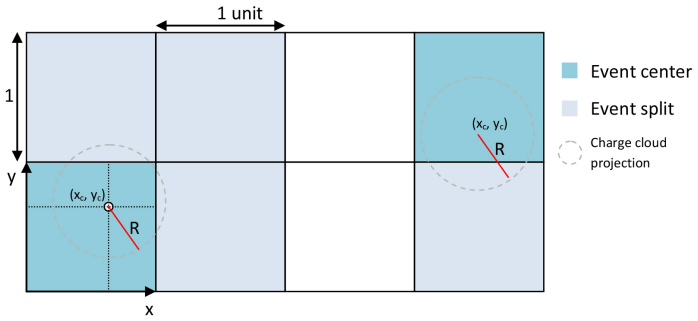

Figure 3.14: A sketch of 8 pixels 2 charge clouds forming a quadruple and a double type event splits. The split pattern depends on R and the center of the charge cloud projection. For many events of equal R, the landing positions centers average up and the event type split distribution depends only on R.

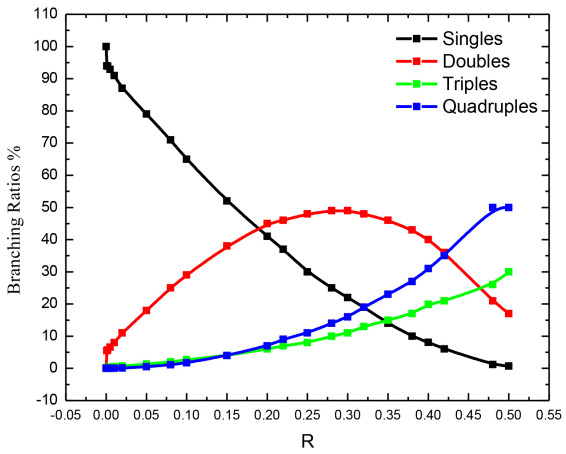

Figure 3.15: Percentages of events distribution as a function of the charge cloud radius R (in units of virtual pixel side length). With increasing R the number percentage of singles decrease, while the percentage of triples and quadruples increase. The percentage of double events increases until R ≈ 0.27 and then decreases. Figure 3.16 (b) illustrates the reason behind this response.

In figure 3.16(b) the percentage of single events decreases with increasing charge cloud radius. The percentage of double events increase up to a maximum value (R = 0.27) and then decreases. For $R > 0.27$ the area of the green rectangles decrease, i.e. the percentage of double events decrease. Triples and Quadruples follow a monotonically increasing curves.

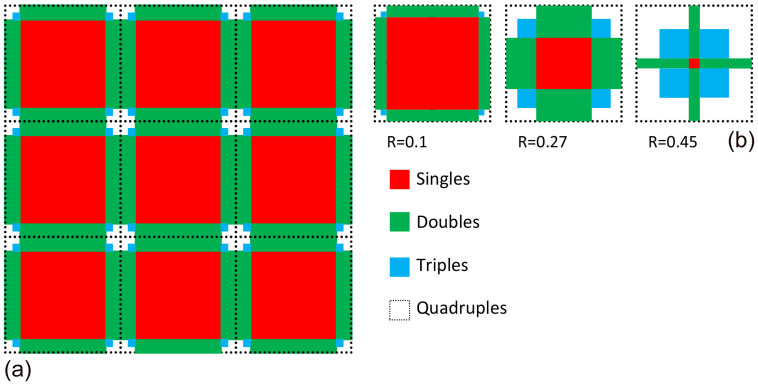

Figure 3.16: Locus of the center of a charge cloud landing position for different event types. In (a) 9 pixels are sketched where the locus of different event type centers are marked in color. For example, a triple event is created if the locus of the event charge cloud is within the blue shaded area. Subplot (b) illustrates how the distribution (branching rations) of different events is related to the size of the charge cloud radius.

3.1.4 Charge cloud size

Figure 3.15 shows that variation in the number of doubles in response to increasing R value is minimum in comparison to single, triple and quadruple events. Thus, for further analysis the doubles are neglected. Mathematically this is represented in equation 3.7.

$$\frac{\partial S}{\partial R} \geq \frac{\partial Q}{\partial R} \geq \frac{\partial T}{\partial R} \geq \frac{\partial D}{\partial R} \tag{3.7}$$

where S, D, T, and Q stands for the percentage of single, double, triple and quadruple events from the numerical analysis part. 3.15.

Table 3.4: The charge cloud size in relation with the photon energy normalized to the real pixel size of 75µm. Values of row 2-4 are normalized to 1.

Energy(keV)	6.403	8.040	10.551	13.395	17.479
$R_{Singles}$	0.292	0.306	0.318	0.340	0.407
$R_{Triples}$	0.299	0.309	0.322	0.356	0.420
R_{Quads}	0.314	0.328	0.334	0.341	0.354
Average	0.301	0.314	0.324	0.345	0.393
$\sigma(\mu m)$	7.52±0.28	7.85±0.29	8.10±0.20	8.62±0.22	9.82±0.87

In the energy range between 6.403 keV and 17.479 keV the charge cloud size can be described by the following linear relation extrapolated from σ(µm) and E(keV) in table 3.4:

$$\sigma(\mu m) = 6.45(\pm 0.21) + 0.16(\pm 0.02) \cdot E(keV) \tag{3.8}$$

Figure 3.17 shows the plot of equation 3.8.

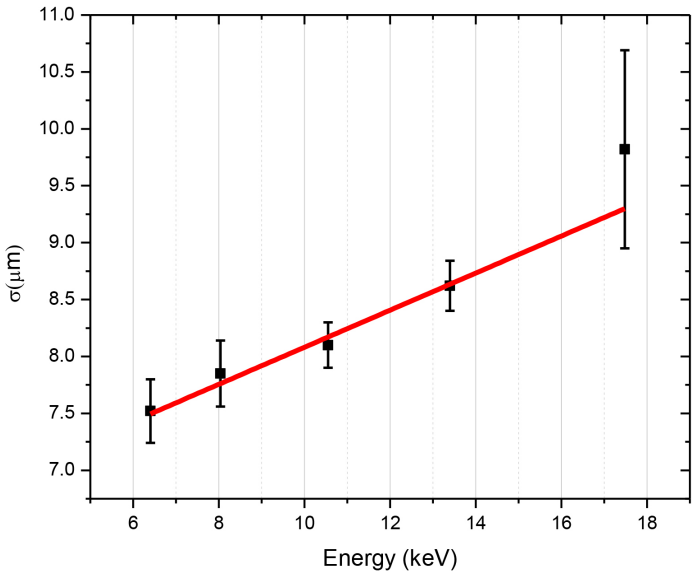

Figure 3.17: The charge cloud radius (σ) follows linearly the energy of photon event.

3.2 Sub-pixel spatial resolution

Charge cloud size and shape can be coupled with the event split patterns in order to determine the X-ray landing position with sub pixel resolution. Event patterns that spread over three or four pixels are used to determine the landing position with an accuracy of 1 x 1 μm^2, whereas the double events can be used to improve the resolution in the split direction. For single-split events, the landing position can be restricted depending on the charge cloud radius, figure 3.15.
In this section, the mathematical formulation of the center of gravity (CG) method for improving the pnCCD spatial resolution is presented and tested. The method can be used for any CCD or pnCCD detector operating in single photon counting mode.

3.2.1 Mathematical derivations

A pixel is represented by a square and the charge cloud projection on the pixel plane by a disk. The center of the disk (the landing position) is the determined by the number of electrons each pixel share, figure 3.18.
The landing position center (X_c, Y_c) is shown in figure 3.18 and is determined by means of the following equations:

$$X_c = P_x - a \tag{3.9}$$

$$Y_c = P_y - b \tag{3.10}$$

where P_x and P_y are the x and y dimension of the pixel, in our case 75 μm each. On the other hand, a and b can be calculated by means of equations 3.11 and 3.12:

$$a = R\cos\alpha \tag{3.11}$$

$$b = R\sin\beta \tag{3.12}$$

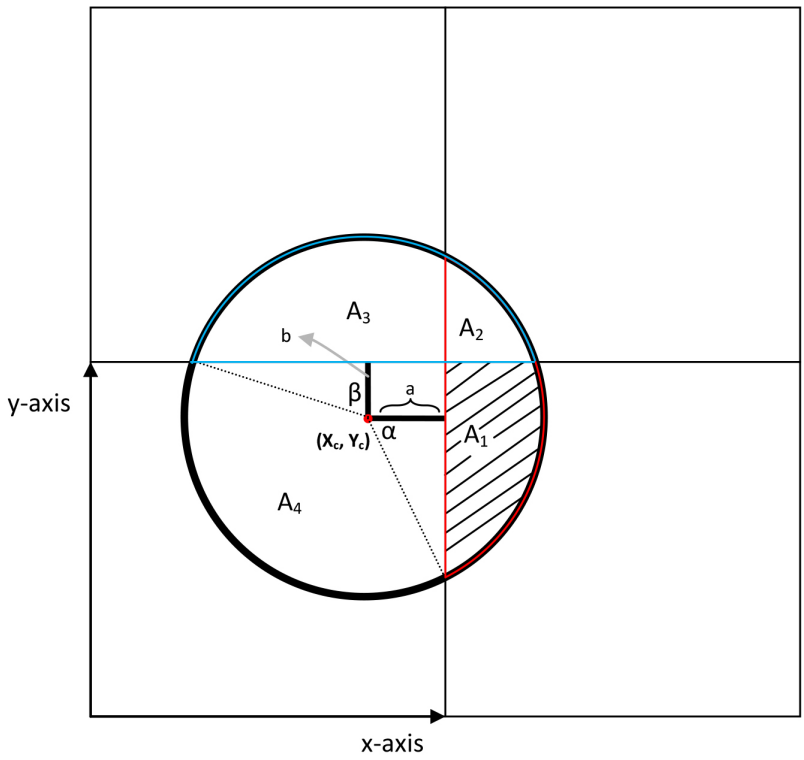

Figure 3.18: The charge cloud shape represented as a circular disk. Areas of the circles sub sectors represented by A1, A2, A3 and A4 represent the splitting ratios between neighboring pixels, whereas the center of the disc at point (X_c, Y_c) is the supposed landing point of the photons.

Angles 2α and 2β face segments $A_1 + A_2$ and $A_2 + A_3$, bounded by red and blue outlines respectively. A_1, A_2, A_3 and A_4 are given in units of electrons. The conversion to meters is done using the density of electrons per unit area which is equal to:

$$\rho = \frac{N_e}{\pi R^2}(e^-/\mu m^2) \tag{3.13}$$

α and β are determined from the following:

$$A_1 + A_2 = A_{segment} = \frac{1}{2}R^2(2\alpha - \sin 2\alpha) \tag{3.14}$$

$$A_3 + A_2 = A_{segment} = \frac{1}{2}R^2(2\beta - \sin 2\beta) \tag{3.15}$$

where α and β are measured in radians.

The solution of equation 3.14 and 3.15 gives α_n and β_n which in turn are plugged in equations 3.11 and 3.12 :

$$X_c(\mu m) = P_x - R\cos\alpha_n \tag{3.16}$$

$$Y_c(\mu m) = P_y - R\cos\beta_n \tag{3.17}$$

3.2.2 Sub-pixel resolution example

To quantify the approach experimentally a ceramic plate 500 µm thick with periodic silver stripes of 100 µm width and spacing of 100 µm was illuminated in transmission by a squared shaped beam profile of X-rays of photon energy in the range between 7-10 keV, figure 3.19.
The ceramic plate was translated parallel to the detector plan with steps of 5 µm, 30 µm and 80 µm with an uncertainty of 1 µm. At each position the X-ray exposure was repeated and a new data set of 50,000 frames is recorded at an average photon flux of 200 photons/s. Figure 3.20 shows the integrated intensity image of the silver stripes (b) and the result after the center of gravity (CG) method is implemented to refine the landing position of the triple and quadruple events(a). Single and double events are not included in the correction.

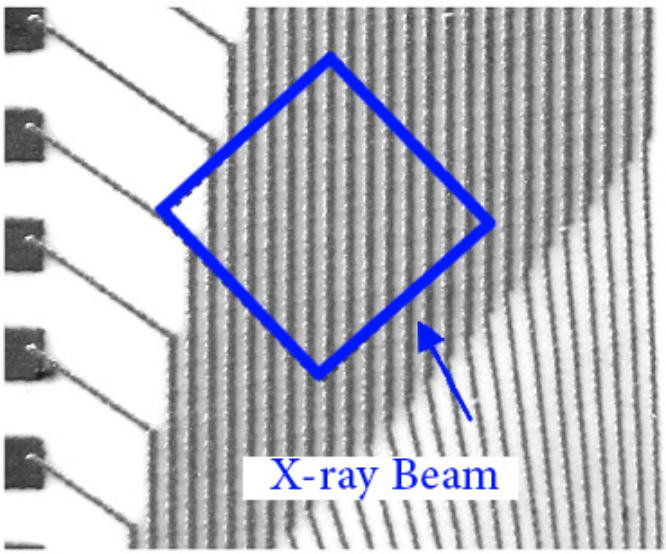

Figure 3.19: Silver stripes with stripe size and pitch of ≈100 µm.

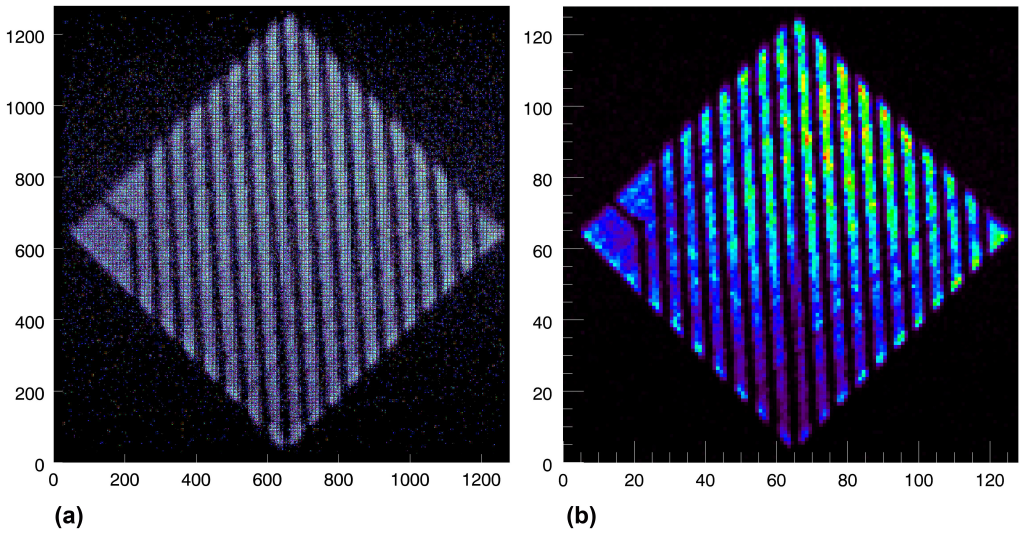

Figure 3.20: A contrast image of the striped silver mesh (b) and the high resolution 10x replica of the same measurement after the triple and quadruple events landing positions were refined with the center of gravity method.

Each real pixel of the 16384 pixels (each is 75 x 75 μm^2) is divided into 100 virtual sub pixels with a size of 7.5 x 7.5 μm^2. The number of sub pixels depends on the number of triple and quadruple events collected. For a pixel size of 75 μm the number of usable events is around 30 percent. If the real pixel is divided into 100 sub pixels then the contrast is reduced by the same factor. As a rule, the higher the number of virtual sub pixels the lower is the contrast.

Taking the horizontal line profile of figure 3.20 (a) for every image at each of the 3 motor positions 5, 30 and 80 μm the motor steps can be measured from the shift of the edge of one or all the silver stripes. The result is shown in figure 3.21 and summarized in table 3.5.

Although, the mesh is translated in step sizes smaller than the real pixel size (75 μm), using the introduced reconstruction methods the movement of the mesh is reconstructed with a sub-pixel resolution.

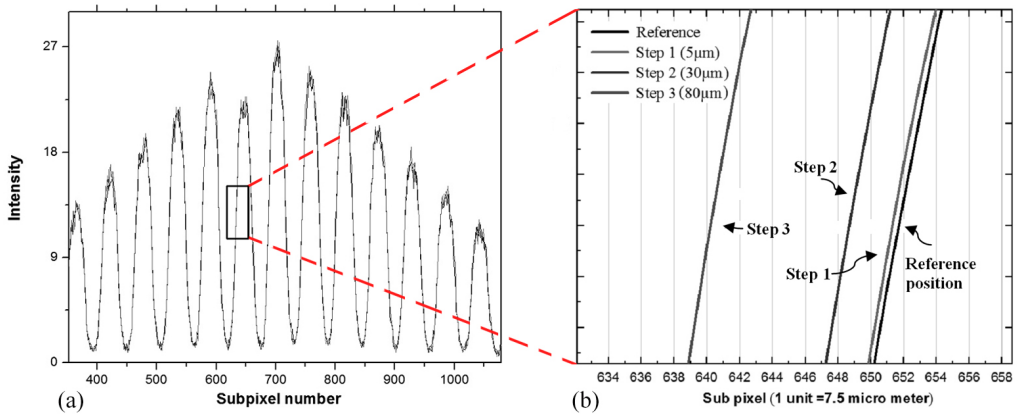

Figure 3.21: (a) The integrated line profiles of the intensity image showing the high and low intensity regions. (b) Overlapped line profiles of the intensity images showing the reference position and after step 1, 2 and 3.

Step	given motor step	measured motor step
1	$5\mu m \pm 1$	$2.6\mu m \pm 1.2$
2	$30\mu m \pm 1$	$24.1\mu m \pm 2.9$
3	$80\mu m \pm 1$	$84.9\mu m \pm 3.5$

Table 3.5: Relative mesh movements from the reference position showing the motor step magnitude given to the motor controller (given motor step) and the measured motor step from the shift in the sub-pixel images line profiles.

3.3 Conclusion

In this part of the thesis a new method is discussed and tested to measure the charge cloud size generated by photons in the pnCCD. Although the measurements was performed with a particular type of CCDs at fixed temperature and depletion voltage, the procedure is independent of the device properties and can be applied elsewhere. The knowledge of the charge cloud size is used to determine the landing position of a charge cloud within the boundaries of a pixel down to the micro meter level without the need to decrease the pixel size physically. Many applications and in particular position resolved X-ray fluorescence spectroscopy and Laue diffraction can directly benefit from the achieved results.

Chapter 4

Application of the pnCCD in material science

4.1 Introduction

The presence of an energy dispersive 2D detector is valuable as a tool which facilitates the development of new experimental methods. Such methods are much needed in the material science communities for many reasons. In the following two sections of the thesis, these reasons are explained in details and two specific examples are provided in which an energy dispersive 2D detector is used to test new methods of study.
The first example, utilizes the pnCCD to simultaneously measure at multiple energies the intensity of Bragg peaks scattered from an iron-platinum multilayer system. The energies are selected in the range of the Pt L-edge in order to enhance the electron density contrast through the energy dependent form factor characteristics. The method allows to measure diffusion coefficients as small as 10^{-19} m^2/s.
In the second subsection, a bent micrometer sized single crystalline copper cantilever is investigated for strain variations using a polychromatic micro Laue diffraction setup. Using the pnCCD, both the energy and spatial evolution of the Laue spots are simultaneously measured. In the future, this method provides the ability to obtain the full strain tensor by a single shot experiment.

4.2 Interdiffusion in Iron-Platinum multilayers

Structural analysis of metallic thin films surfaces and inner electronic density fluctuations is very important for high density magnetic recording devices due to the very large magnetic crystalline anisotropy of these systems. Moreover, metallic thin films act as a model system for the understanding of basic and fundamental phenomena such as inter-diffusion at material interfaces.
Direct imaging techniques such as Atomic Force Microscopy (AFM), Transmission Electron Microscopy (TEM) and Scanning Tunnelling Microscopy (STM) are used to characterize surface topologies and morphologies. However, to study buried and bulk structures the use of X-ray diffraction is necessary. Diffraction at Grazing incident angles to a sample surface (GISAXS) was introduced in 1989 [20] as a response for a necessity to understand in details thermodynamical and kinematic processes between the different components of a thin film. GISAXS has been established as a method that is widely used at many synchrotron radiation experimental stations.
Advantages of the method: GISAXS uses X-rays and thus beam-induced changes are negligible in comparison to electron based methods. Since GISAXS is implemented in a reflection geometry at an angle below the critical angle of the substrate material, the thickness of the substrate is not restricted and the background level of scattered intensity from the substrate is significantly low.
An interesting feature of GISAXS is that the scattering factor near the absorption edge of the sample elemental components becomes energy dependent. This enhances the electron density contrast. The technique is known as Anomalous Small-Angle Scattering (ASAXS) and has the potential to understand complex materials. However, many restrictions limits its wide use which mainly arises from the complexity of the setup. Until now, an ASAXS experiment consist of 2 independent steps. At each, one data acquisition is performed at an X-ray energy below the absorption edge (pre-edge) and one above (post-edge). In a static experiment, this is performed without effort. However, for an experiment where the sample temperature is changing during X-ray exposure (in situ), the structural variations may be faster than the time needed for data acquisition. The presence of a 2D energy dispersive pnCCD would overcome this obstacle.

Anomalous small angle scattering with the pnCCD is introduced as a method of study of thermally induced interdiffusion in Iron-Platinum thin film multilayers in a temperature range between 300-585 K [21].
The next parts of this section introduces the theory of ASAXS, X-ray reflectivity and interdiffusion in multilayers with the intuition needed to understand the results of the experiment.

4.2.1 Anomalous Small Angle X-ray Scattering

Within the scope of the kinematical X-ray scattering theory where x-ray photons scatter only once by the electrons of an atom, coherent scattering takes place when the incident photon undergoes a change in direction without changing is wavelength. The amplitude of the scattered beam from atoms (k) at positions ($\mathrm{r_k}$) is:

$$A(Q) = \sum_k f_k(Q) \exp(-Qr_k) \tag{4.1}$$

where $Q = 4\pi \sin\theta/\lambda$ is the diffraction wave vector, $f_k(Q)$ is the atomic scattering factor (or form factor) and $\exp(-iQr_k)$ is the phase factor. The form factor is the Fourier transfer of the electron density $\delta\rho$. The total scattered intensity (structure factor) is expressed as the square of the amplitude:

$$I^{coh} = \langle A(Q)A^*(Q)\rangle = \langle \sum_j \sum_k f_k(Q) \exp[-iQ(r_j - r_k)]\rangle \tag{4.2}$$

Each atom has its own absorption edge beyond which an orbital electron can be ejected into the continuum states. In conventional x-ray diffraction, the energy of the x-ray beam is fixed and is selected to be far from the edge of the probed material matrix, thus the energy dependence of the scattering factor is not taken into account. However , when the x-rays energy is very close to the absorption edge the scattering factor becomes complex and be expressed as follows:

$$f(Q, E) = f_0(Q) + f_1(E) + if_2(E) \tag{4.3}$$

where f_1 and f_2 is the real and imaginary parts of the anomalous dispersion term

which are both energy dependent.

f_2 is related to the photoelectric effect cross section as follows:

$$f_2 = \frac{E\mu_{PE}(E)}{2hcr_e} \tag{4.4}$$

where r_e is the classical electron radius, c is the speed of light, and h is Planck's constant. On the other hand f_1 is related to f_2 by the Kramers-Kronig relation:

$$f_1(E_0) = \frac{2}{\pi}\int_0^\infty \frac{Ef_2(E)}{E_0^2 - E^2}dE \tag{4.5}$$

4.2.2 X-ray reflectivity from multilayers

The intensity distribution of the reflectivity curves from multilayers is used to determine layer thicknesses and interface roughnesses. The mathematical formulation of the reflectivity is derived from the dynamical theory of diffraction. Below is a brief presentation of the formalism of reflectivity from single and multilayers. In a single layer system, X-rays reflected from the upper and the lower interfaces. The reflectivity depends on the difference in the refractive indexes between the layer and the substrate on which the single layer is deposited. Mathematically, the reflectivity is expressed as in equation 4.6:

$$R = \frac{r_1 + r_2\exp(-2ik_{oz}t)}{1 + r_1r_2\exp(-2ik_{oz}t)} \tag{4.6}$$

where $r_{1,2}$ are the Fresnel reflectivity coefficients, k_{0z} is the vertical component of the wave vector of the transmitted beam and t is the single layer thickness. From equation 4.6, it shows that the reflectivity is maximum when the exponential term is equal to 1. This is achieved if the incident angle α_{im} satisfies equation 4.7:

$$2t\sqrt{\sin^2\alpha_{im} - \sin^2\alpha_c} = m\lambda \tag{4.7}$$

where α_c is the critical angle of total external reflection for the top layer material. A multilayer on the other hand, is a formed when multiple pairs (triples...) of single layers are stacked over each other. The total reflectance of the inter-layers are summed together to give an interference pattern in which the intensity modulation

depends on the index of refraction defined as $n = 1 - \delta + i\beta$. If the multilayer is composed of N periods and a modulation period (A+B) of thickness t_A and t_B, and a substrate (S), then the reflectance can be written in terms of the phase terms of the incident X-ray beam amplitudes (ϕ_A and ϕ_B) as it is given in equation 4.8 and presented in [22]:

$$R = \mid r_{0A} + r_{AB}[\phi_A^2 - \phi_A^2\phi_B^2 + \phi_A^2\phi_B^2\phi_A^2 - ... + (\phi_A^2\phi_B^2)^{N-1}] + r_{BS}(\phi_A^2\phi_B^2)^N \mid^2 \quad (4.8)$$

where r_{0A} and r_{BS} are the Fresnel reflection coefficients of the top layer and the substrate surface respectively. The summation of the term in the brackets lead to equation :

$$R = \mid \frac{r_{0A} + r_{AB}\phi_A^2\phi_B^2(\phi_A^2 - 1)(\phi_A^2\phi_B^2)^{N-1} + \phi_B^2 - 1}{(\phi_A\phi_B)^2 - 1} \mid \quad (4.9)$$

The value of R is maximum when the derivative is equal to zero, i.e. when $(\phi_A\phi_B)^2 = 1$ The condition for maximum reflectivity leads to the condition in equation 4.10:

$$2D\sqrt{\sin^2\alpha_i - \sin^2(\alpha_c)} = m\lambda \quad (4.10)$$

4.2.3 Interdiffusion in Multilayers

"Interdiffusion in Multilayers can be determined from the rate of homogenization of compositional modulation structure of the Multilayers", [23].
The composition of a component (c), in position x and time t can be described in one dimension by Fick's second law for concentration-dependent diffusivity:

$$\frac{\partial c}{\partial t} = D\frac{\partial^2 c}{\partial x^2} - \frac{2D}{\zeta}\kappa\frac{\partial^4 c}{\partial x^4} \quad (4.11)$$

where D is the bulk inter-diffusivity, ζ is the second derivative of the Helmholtz-free energy and κ is the gradient energy coefficient. When κ and ζ become independent of the composition (small composition amplitude) the solution of equation 4.11 is:

$$c = \exp\left[-D\beta^2\left(1 + \frac{2\kappa\beta^2}{\zeta}\right)t\right]\cos\beta x \tag{4.12}$$

where $\beta = 2\pi/L$ and L is the multilayer bilayer thickness .
The effective inter-diffusivity coefficient D is given by equation 4.13

$$\tilde{D}(t) = D\left(1 + \frac{2\kappa\beta^2}{\zeta}\right) \tag{4.13}$$

Moreover, the Bragg peaks intensity is related to the effective inter-diffusivity coefficient by equation 4.14:

$$\tilde{D}(t) = \frac{-L^2}{8\pi^2}\frac{d}{dt}\ln\left[\frac{I(t)}{I(0)}\right] \tag{4.14}$$

The Arrhenius equation summarizes all the inter-diffusivity at various temperatures to find the activation energy H_a given in equation 4.15.

$$\tilde{D}(t) = D_0\exp(-\frac{H_a}{k_bT}) \tag{4.15}$$

4.2.4 Experimental Setup and pnCCD settings at Bessy II

The experiments are performed at the EDR beam line of the storage ring BESSY II using white synchrotron radiation. Detailed description of the beam line is given in previous sections of the thesis. Particular for the current experiment, the incident flux at the sample position is reduced to avoid detector saturation by placing 0.8 mm thick Aluminum sheet by means of an absorber box placed in the beam path. Defined by a collimator the incident beam is confined to a size of 1 mm horizontally and 0.2 mm vertically proceeded by a first collimator with an opening of 1 x 1 mm^2 to reduce parasitic scattering at the detector. Finally, the position was adjusted by means of a 4 axis motor stage such that the incident beam strikes the sample under a fixed incidence angle of 1.8°. The pnCCD is placed at a distance of 0.305 m behind the sample and is moved 12 mm upward relative to the incident beam in order to protect it from it. The sample under investigation is placed inside a vacuum chamber at 0.1 mbar coupled with an *Anton Paar DHS*

1100 heater and controlled by a *TCU200* control unit[1]. See figure 4.1 for setup details.

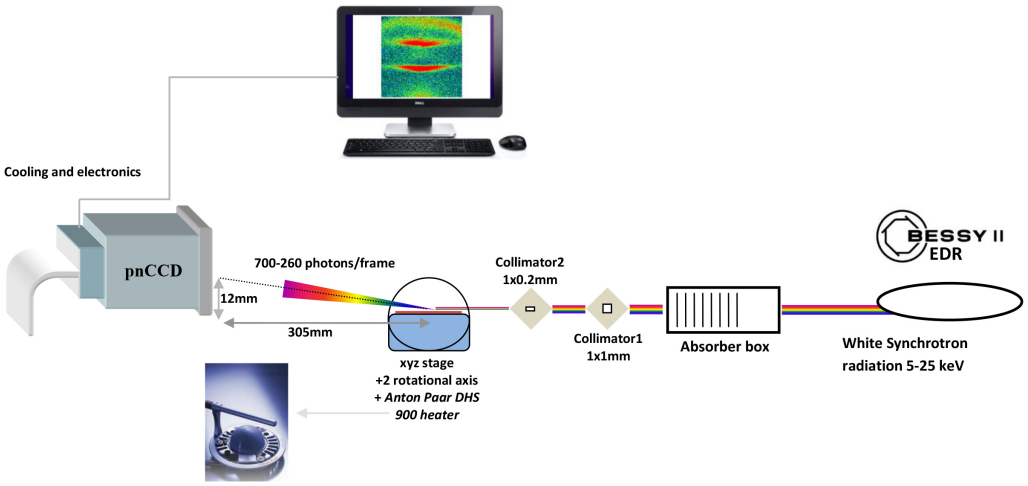

Figure 4.1: GISAXS setup geometry used at the EDR beam line in BessyII. The white synchrotron radiation was attenuated with absorbers to reduce flux. The beam is then guided through a series of collimators to reduced scattering and confide the beam size. The sample placed in a vacuum environment was illuminated at a small angle.

The Fe-Pt multilayer (ML) samples are prepared by magnetron sputtering using a custom built ultra-high vacuum deposition system and two separate metal targets. The Ar sputtering gas pressure is 0.67 Pa. The MLs with nominal composition [Fe 2.0 nm− Pt 2.0 nm]$_{50}$ are deposited onto thermally oxidized (100) Si wafers (1500 µm thick SiO_2 buffer layer). The wafer is diced into 15 x 10 mm^2 samples for subsequent measurements.

A 256 x 256 pixels eROSITA frame-store pnCCD is used for the present experiment. Square pixels of side length 75 µm form the image area. 75 x 51 µm^2 pixels form the storage area. The detector is operated at 230 V back voltage to achieve full depletion. 2 DUO CAMEX ships (Dark Universe Observatory) read the pnCCD signal at a frame rate of 130 frame/s. The pnCCD is placed in a vacuum chamber at a pressure of 10^{-7} mbar. A Copper cooling mask connected to a liquid Nitorgen (LN_2) cycle keeps the detector at an operating temperature of 210 K, figure 4.2 [11].

[1] http://www.anton-paar.com

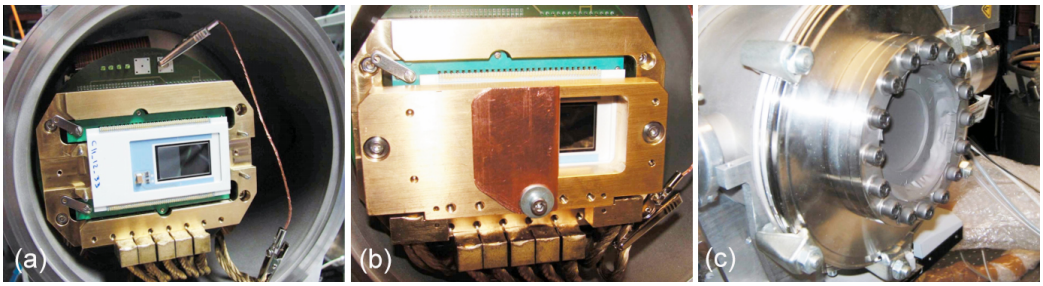

Figure 4.2: The eROSITA frame-store pnCCD. (a) The Vacuum chamber and the ceramic board. (b) A Cu mask of few centimeters is used for cooling, the dark tinted Cu plate used as a shield for the frame store area is also visible.(c) The chamber was closed using a graphite-coated Kapton window of 200 μm *thickness to avoid noise contributions from background light.*

4.2.5 Measurement methodology

The ML [Fe 2.0 nm− Pt 2.0 nm]$_{50}$ sample contains two elements, Platinum with atomic number Z = 78 and Iron with Z = 26. The absorption edges of the 2 elements are tabulated below in table 4.1 [24]:

Edge	K (keV)	L (keV)	M (keV)
Pt_I	78.394	13.879	3.296
Pt_{II}	-	13.272	3.026
Pt_{III}	-	11.563	2.645
Pt_{IV}	-	-	2.201
Fe_I	7.112	0.846	0.092
Fe_{II}	-	0.721	0.054
Fe_{III}	-	0.708	0.054

Table 4.1: Edge energies for Platinum 78 and Iron 26

Due to the fact that the detector chamber consists mainly of iron, the presences of iron fluorescence radiation in the background is significant (at $K_{\alpha 1}$ = 6.403, $K_{\alpha 2}$ = 6.393 keV and $K_{\beta 1}$ = 7.057 keV). This decreases the signal to noise ratio at the iron K-edge and prohibits the use of the iron K-edge in the analysis. On the other hand, the primary incident spectrum is limited to 45 keV, thus the use of

the 78.384 keV platinum k-edge is not possible. Hence, the focus is directed onto probing at platinum L-edges.

The real absorption edges of Pt embedded in an Fe-Pt composite multilayer is expected to shift from that of a free Pt sample due to chemical interactions. This shift is around 20 eV, however this shift is insignificant to the measurement where the energy resolution (FWHM) of the pnCCD is approximately 180 eV at 13 keV. Further more, the absorption edge shift during annealing by approximately 5 eV, which also is neglected in comparison with the energy resolution permitted by the pnCCD [25]. Figure 4.3 represents the energy dependent scattering factor terms f_1 and f_2 close to the platinum L-edges.

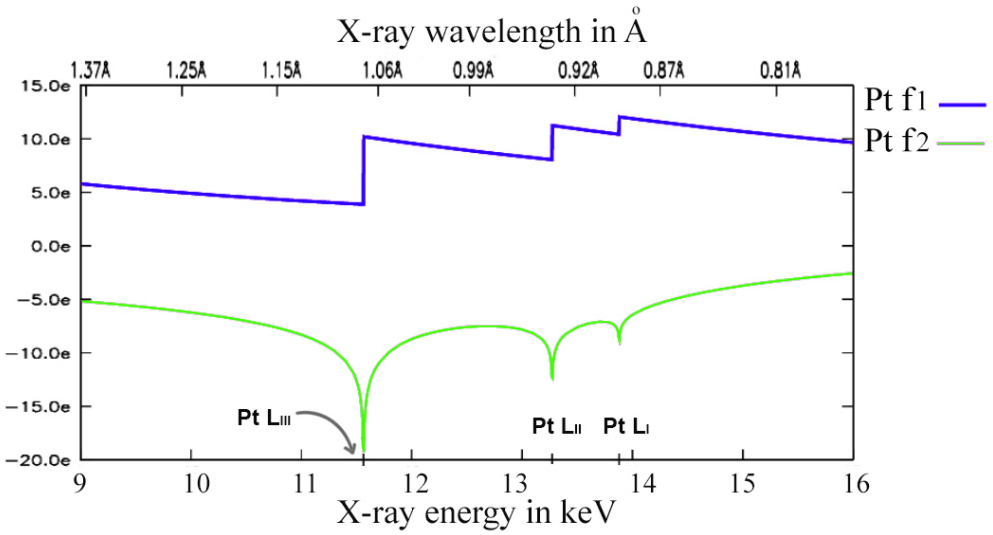

Figure 4.3: f1 f2 and the absorption edges as a function of energy.

Technically, the in-situ experiment is conducted in a temperature range between 298-583 K. 10 data sets are recorded at T=[298, 462, 483, 508, 533 ,548, 558, 568, 578, 583 K]. Each step lasted 18.5 min divided into 5 min temperature ramping intervals, 1 min "temperature stability" interval and approximately 12.5 min data acquisitions intervals. Since the incident X-ray beam is pink, no time interruptions take place in order to tune the energy of the beam. The measurement plan is sketched in figure 4.4. All data sets consist of 300 dark frames with no X-ray exposure and 100,000 data frames. The dark frames are written to determine noise and offset of the pnCCD channels.

Data analysis process is proceeded by correcting each data set for the charge transfer inefficiency (CTI correction), quantum inefficiency and background noise. A "background data set" is recorded without the sample to quantify background noise. The synchrotron ring electron current drops and consequently the photon intensity drop was all accounted for by recording the machine current as a function of time [5] [18].

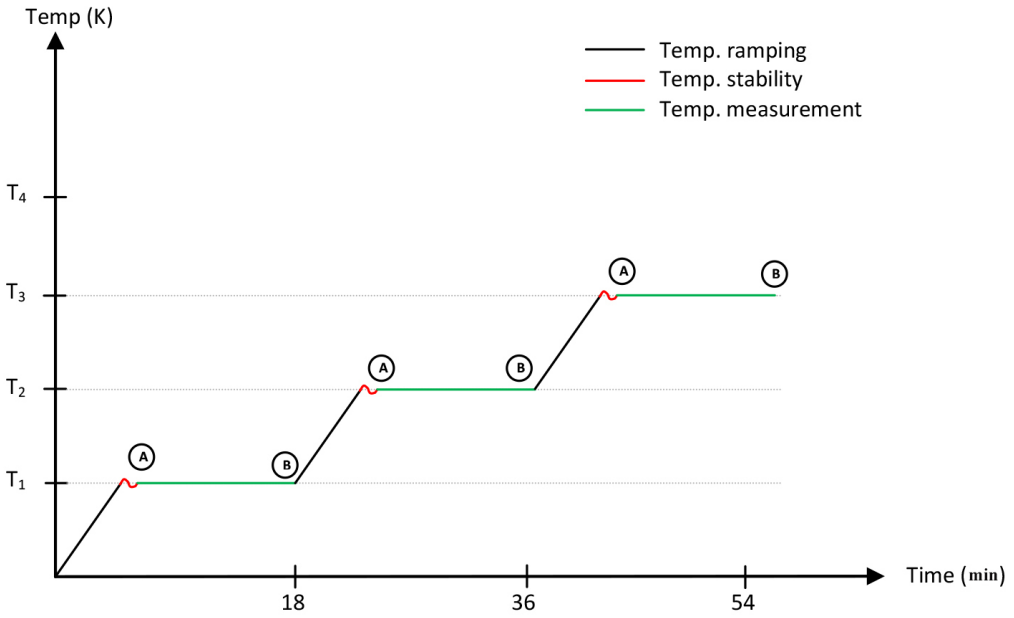

Figure 4.4: Measurement plan for the Iron Platinum ML. Data acquisition was performed between points marked A to B.

In the following sections the results are presented in the following order:

1. The Bragg peaks intensity is presented as a function of temperature and energy between 10-20 keV. Readings from point B in reference to figure 4.4.

2. The Bragg peaks intensity at and outside the L-edges of Platinum is presented to highlight the contrast at the edge. Readings from point B in reference to figure 4.4.

3. The change of the Bragg peak intensity as a function of time at a fixed temperature is presented at 11.2 keV. Readings from point A-B in reference

to figure 4.4.

4. The activation energy of interdiffusion is calculated to validate the method used.

5. Interdiffusion is modeled with the formation of inter-layers between the interface of Iron and Platinum.

4.2.6 Results: Decay of the Bragg peaks

In energy-dispersive mode each pixel of the detector measures the scattering angle (via pixel position with respect to the incident beam position) and the scattering energy. Therefore, the scattered vector magnitude and direction is obtained simultaneously for the whole energy range of the incident vector. The corrected stored data is sliced into slices of 100 eV width. Figure 4.5 shows the 1st and 2nd order Bragg peaks at different energies. For higher energies the peaks shift in the direction of the incident beam.

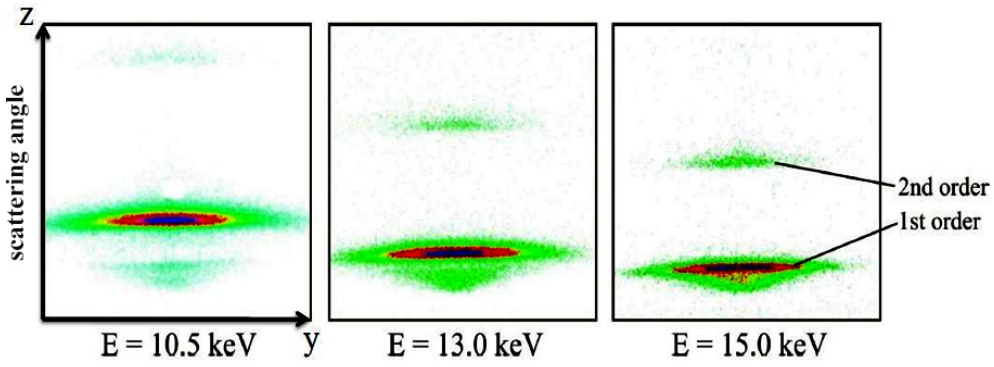

Figure 4.5: Two dimensional images from the detector sliced in the energy domain. The 1st and 2nd order Bragg peaks can be identified as their position and intensity change as a function of energy.

In order to extract the coherent reflectivity from the 3D data volume, all the 2D images were integrated along the y-axis (see figure 4.5) and the resulting reflection curves were displayed as function of energy Figures 4.6 and 4.7 are the 3D and

2D plots respectively of the integrated line profiles. In 4.6 the Bragg peaks (1st, 2nd and 3rd) decay in intensity for higher energies. For high energies the incident beam penetration depth increases and thus the scattered intensity decreases. The 2D plot in figure 4.7 shows again the Bragg peaks shift for higher energies along with fluorescence signals from the platinum L edges. In ”blue” is the second term of the form factor plotted with respect to the energy axis. The shifting in the form factor magnitude takes place at the L edges of platinum.

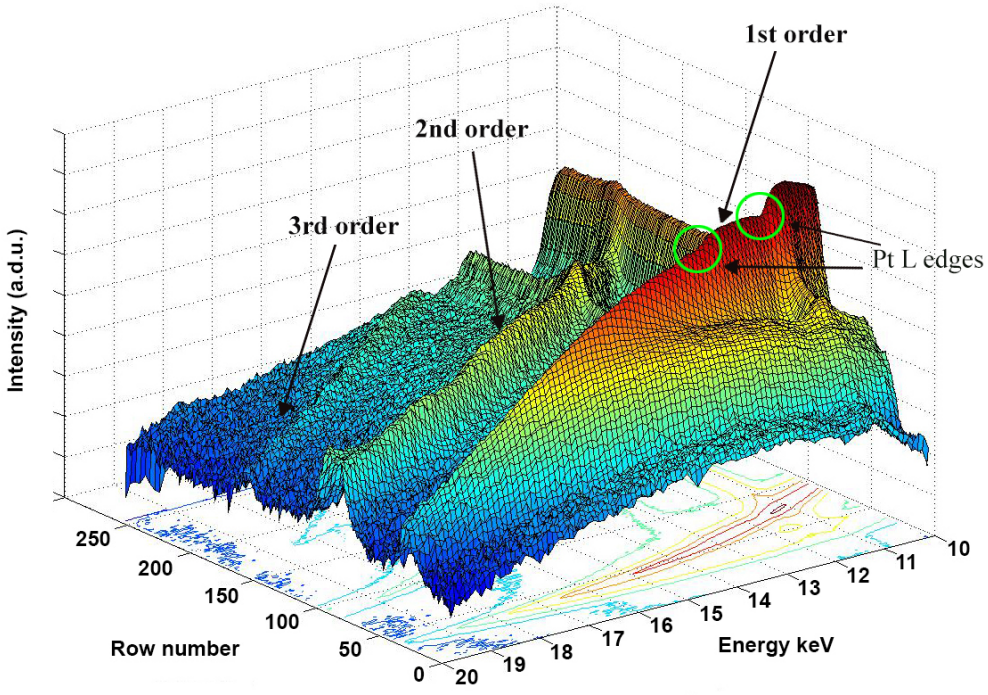

Figure 4.6: 3D plot of the line profiles extracted from 2D plots of figure 4.5. 1st, 2nd and 3rd order Bragg peaks are visible as a function of energy. The Pt L-edges are marked with green circles.

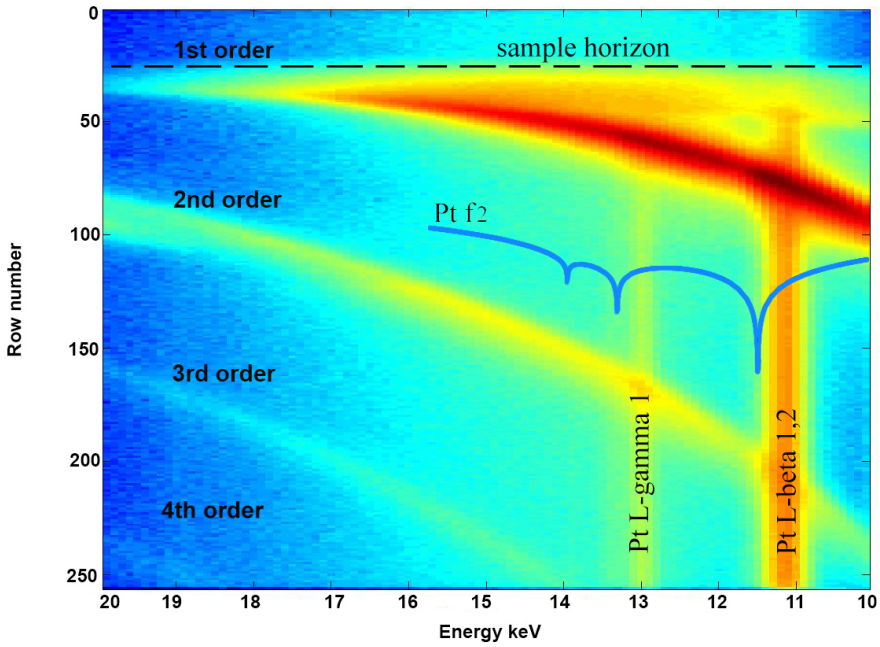

Figure 4.7: 2D projection of figure 4.6 highlighting the spatial evolution of the Bragg peaks as the energy increases. The second term of platinum form factor is plotted in blue for the same energy scale.

A previous study [26] has shown that 2 regimes of interdiffusion are expected: one below $T_c = 534 \pm 4$ K corresponding to a slow, short range diffusion. In this regime no change in the texture of the ML are expected. The second temperature regime above T_c where the diffusion process is much rapid. The temperature dependence of the 1st and the 2nd Bragg peaks are shown in figure 4.8 and 4.9, in the range of the platinum L-edges (10-15 keV). For both peaks the variations of intensity is seen to be maximum at the Platinum L-edge compared to the intensity at energies outside the edge. The drop in intensity with temperature is a result of mis-orientation of the grains that are perpendicular to the ML film plane [26].
Using these data we selected four different energies [10.0, 11.2, 11.3, and 11.8 keV] for a quantitative data analysis, i.e. one energy value before, one after and two within the L-lines of Platinum.

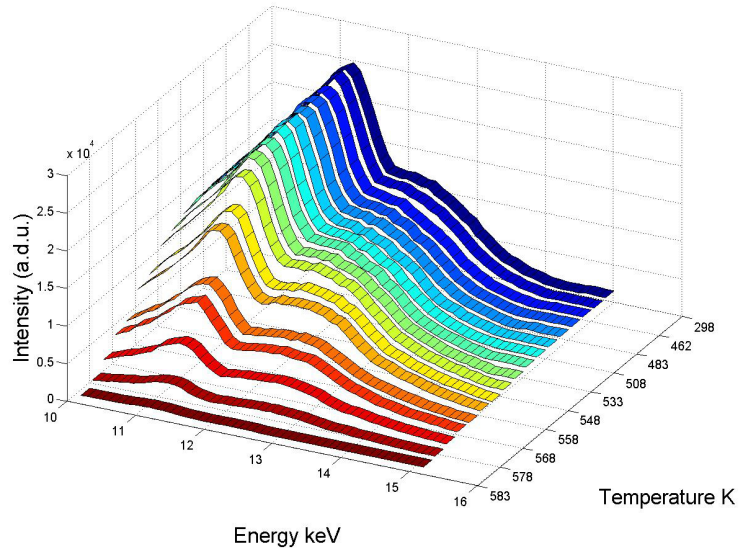

Figure 4.8: 1st order Bragg peak integrated intensity versus energy keV *and temperature* K. *The intensity of the Bragg peaks drop with temperature.*

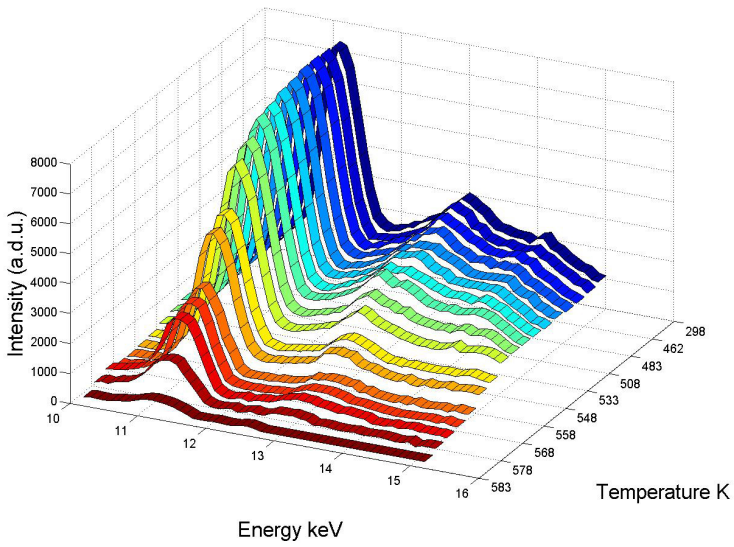

Figure 4.9: 2nd order Bragg peak integrated intensity versus energy keV *and temperature* K. *Two distinguished temperature regimes are visible, below and above 533* K. *The plot also shows that at the L-edges energies 11.563* keV *and 13.879* keV *the contrast is at its highest (peak to edge ratio).*

Enhanced contrast can be seen when the Bragg peak intensities are plotted for energy bands at the L-edge of Platinum and away from the edges. In figure 4.10 the variations of the peak intensities are shown where the two different regimes are more pronounced and can be distinguished. First a slow decay of intensity is followed by fast decay after T_c = 533 K.

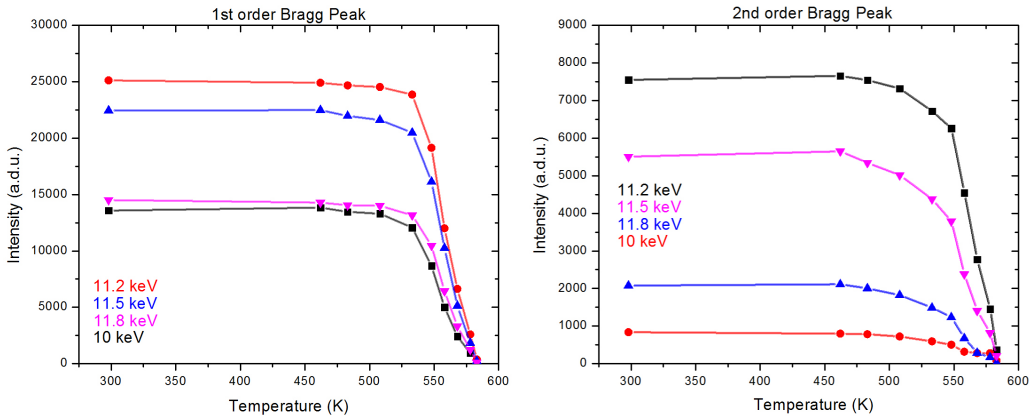

Figure 4.10: 1st order and 2nd order Bragg peaks intensity drops with increasing temperature.

In order to study the dynamics of interdiffusion, time scans are preformed at a fixed temperature. From point 'A' to 'B' in reference to figure 4.4 the 12.5 min data acquisition interval is divided into 10 sub-intervals of equal length. In this manner the Bragg peak intensity is monitored as a function of time in an isothermal environment. Four temperature values are selected. One in the slow decaying part of figure 4.10 and three in the fast decaying part (509, 533, 548 and 558 K). Intensity decay of the Bragg peaks as a function of temperature follows the exponential law $\exp(-T/\tau)$. The result is plotted in figure 4.11 and fitted a with zero offset in order to determine the time constants τ and hence the interdiffusion constant $\tilde{D}$ as in equation 4.14.

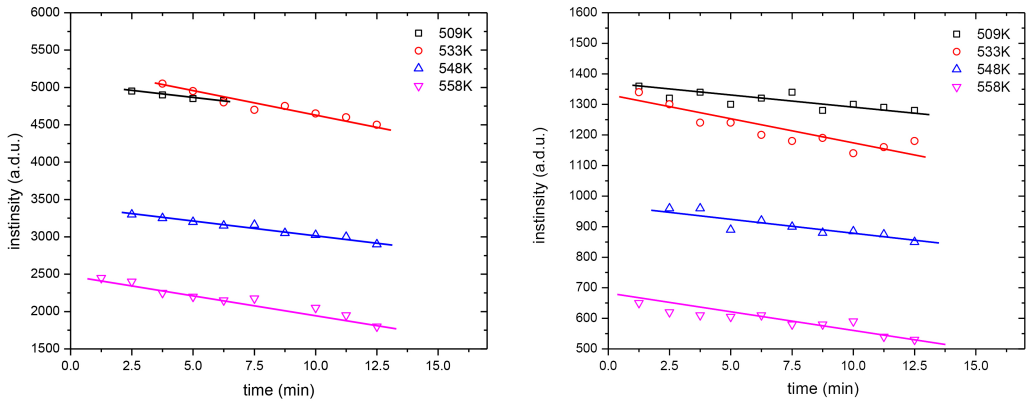

Figure 4.11: Intensity decay of the 1st (left) and the second order Bragg peak (right) as a function of the annealing time and the annealing temperature of the MLs. The data points were fitted to an exponentially decaying function

The corresponding time constants τ are given in the table 4.2 where again two temperature regimes can separated before and after 533 K. In the first temperature regime τ is 3 times larger than in the second one. For the 1st and the 2nd order Bragg peaks the time constants are comparable within the error interval.

Temp.(K)	1st order(min)	$\ln\tilde{D}(m^2/s)$	2nd order(min)	$\ln\tilde{D}(m^2/s)$
509	191±31	-43.179±0.005	212±56	-43.283±0.005
533	84±10	-42.357±0.012	78±12	-42.283±0.013
548	80±5	-42.308±0.013	71±12	-42.189±0.014
558	50±5	-41.838±0.020	63±7	-42.069±0.016

Table 4.2: Diffusion time constants in minutes for the 1st and 2nd order peak. The effective diffusivity is also given in column 3 and 5

The interdiffusion coefficients at low annealing temperatures (500-600 K) are expected to be relatively low [23] [26]. The values presented in table 4.2 are in the order of 10^{-19} m^2/sat low temperatures in comparison to values measured at ($T > 1173$) [27], which are 3x larger. The possibility to measure diffusion coefficients in the range of 10^{-20} m^2/s in metallic multilayers is a real challenge.
The obtained interdiffusion coefficients are used to determine the activation energy of the interdiffusion process in the temperature range 533-558 K. Described by

the Arrhenius law in equation 4.15, the activation energy is the result of a linear fit to the logarithmic values of the interdiffusion coefficients versus $1/T$. Both the 1st and the 2nd order Bragg peaks plots display Arrhenius behavior with activation energy 0.618 ± 0.115 eV and 0.686 ± 0.106 eV respectively (figure 4.12). Both values of the activation energy are less than 1.0 eV which is similar to that of interstitial atomic diffusion. This mechanism is much preferred when atoms in a crystal lattice are thermally activated.

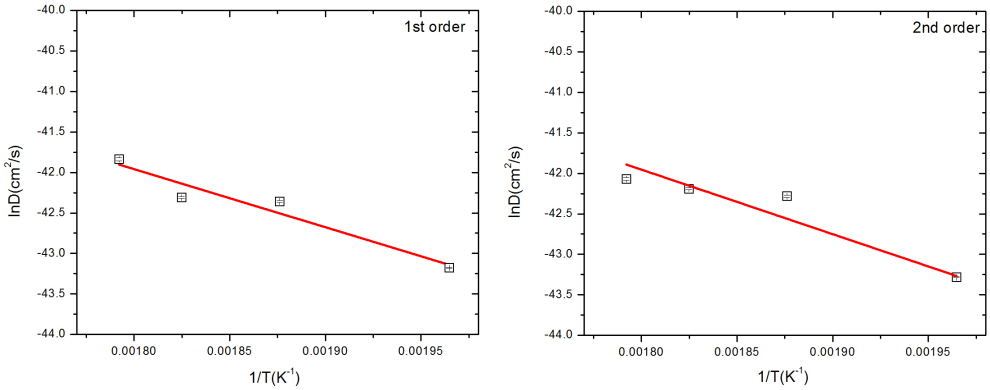

Figure 4.12: Arrhenius plot of ln(D) vs 1/T. The temperature dependence effective interdiffusivity $\tilde{D}$ plotted versus the inverse annealing temperature. The solid line indicates the linear fit of the data.

4.2.7 Modeling and Simulation

The multilayer used in this experiment is formed of consecutive pairs of iron-platinum layers (50 pairs) on a Silicon substrate. The reflectivity curves can be modeled by IMD[2] an extension of xop [28]. For modeling the interfaces between the layers before annealing are supposed to be smooth and free of diffused boundaries or any foreign structure as a result of chemical reactions. The interdiffusion process at the boundaries between layers is modeled by inserting an interlayer with thickness "w" between each two consecutive layers. The interlayer is com-

[2]Specular optical functions; reflectance, transmittance, absorbency, field intensities, phase shifts, and ellipsometric psi and delta functions; are computed in IMD using an algorithm based on recursive application of the Fresnel equations, modified to approximate the effects of interfacial roughness and/or diffuseness. See http://www.rxollc.com/idl/IMD.pdf

posed of iron and platinum with linearly decreasing concentrations as shown in figure 4.13

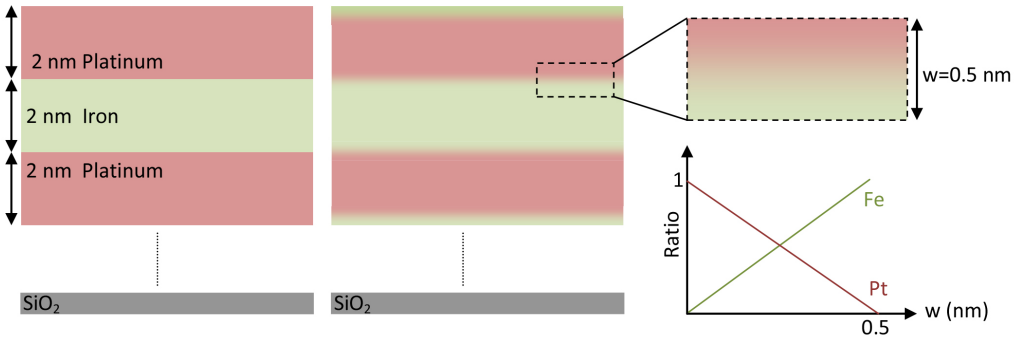

Figure 4.13: Schematic figure of a perfect ML (left) and a ML with interlayer structure (middle). The density profile of the interlayer is linearly decreasing away from the boundaries (bottom right plot).

The total thickness of the sample is left unchanged, whereas the individual layer thickness of Fe and Pt is decreased and the $Fe + Pt$ interlayer thickness is increased. The interlayer composition and thickness is increased in steps and the resulting intensity of the first Bragg peaks are compared with the experimental results. The simulation is performed at two energies 11.2 keV and 11.8 keV just before and after the Platinum L_1 edge. See table 4.3.

Model number	1	2	3	4	5	6	7
Modeled Temp.(K)	289	453	478	503	528	533	543
Fe/Pt ratio	1	3/2	7/3	4	9	9	19
w (nm)	0.5	0.5	0.5	0.5	0.5	1	1.6

Table 4.3: 7 models were simulated in an attempt to describe the sample response at 7 different temperatures. Both the Fe and Pt ratios in the interlayer and the thickness of the interlayer was changed to replicate the experimental data.

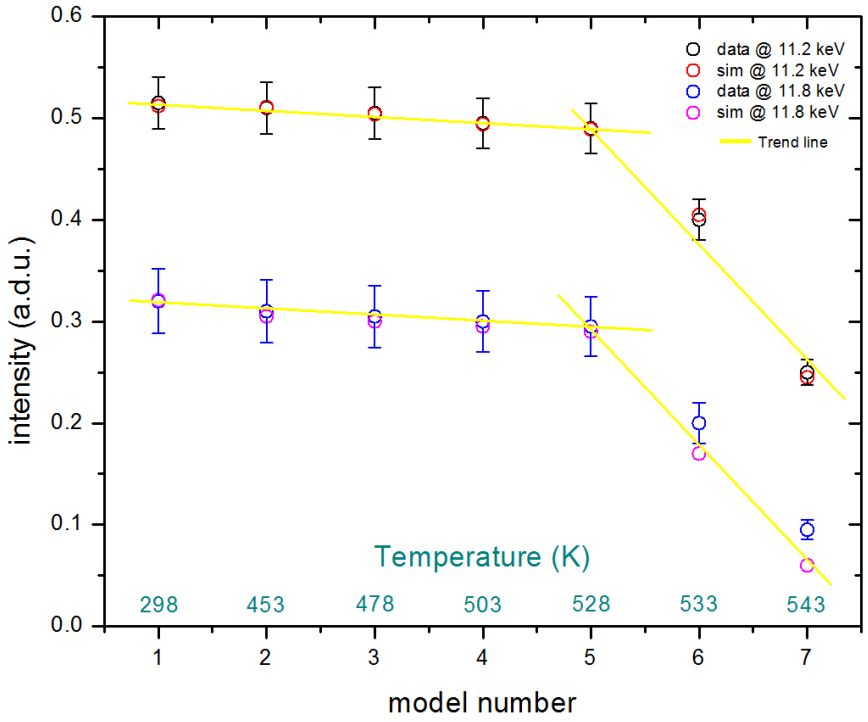

Figure 4.14: schematic figure of a perfect ML (left) and a ML with interlayer structure. The density profile of the interlayer is linear decreasing away from the boundaries

Based on the simulation results, the reduction in the Bragg peaks intensity is attributed to interface roughness due to thermally induced diffusion at the layers boundaries. Although the roughness parameter in the simulation is kept at zero level, the density profile of the interlayer can be supposed to act similar to that of an induced roughness. On the other hand, the bilayer thickness (Fe, Pt and Fe+Pt) remains constant, thus the Bragg peak position do not move with annealing. Moreover, the simulations demonstrate that the interface layer is created mainly by Fe atoms diffusing into the neighbored Pt layer which can be explained by the smaller ionic radius of Fe atoms compared to Pt by a ratio of 0.76 [29].

4.2.8 Conclusion

Anomalous small angle x-ray scattering is performed on Fe-Pt multilayers system using a pink X-ray beam and an energy dispersive pnCCD detector. ASAXS, although a challenging technique, is applied without considerable effort to study

dynamics of diffusion in the sample at different temperature regimes.
With the use of an energy dispersive pnCCD, the scattered photons energies, position and time coordinates are extracted from a 4D data volume after the experiment and hence no interruptions during annealing are needed to select between different energies (which is the case in usual ASAXS). By using a Fe-Pt multilayers system , the interdiffusion was quantified with enhanced contrast by measuring at energies around the Platinum L-edge. The interdiffusivities are accurately measured in one Fe-Pt system and was determined to be in the magnitude of 10^{-19} m^2/s, a value which is much lower compared to high temperature annealing with values of about 10^{-16} m^2/s. The obtained interdiffusion coefficients are temperature dependent and are described by the Arrhenius relation. A detailed simulation study is performed to model the change of intensities of the Bragg peaks as a function of temperature and the results are interpreted by the formation of an interlayer with variable width and composition.
In this part of the thesis a new method to measure small interdiffusion coefficients in a ML system is introduced. For many years, interdiffusion in metallic ML remained poorly quantified because of the experimental difficulties associated with low diffusivity at low temperatures. The presence of an energy dispersive, 2D, and polychromatic X-ray diffraction experiment provides a step forward in the understanding of diffusion mechanisms.

4.3 Polychromatic μLaue diffraction using a pnCCD

Determination of a Laue pattern spot energies and their spatial distribution of the intensities are necessary for a quantitative analysis of dislocation density and distribution. However, the progress in experimental methods to achieve this aim is still slow. In this section, a new experimental method is presented that allows to follow changes crystallographic orientations of micro crystals during a deformation by utilizing a pnCCD detector. First, the Laue method is introduced and then extended to energy dispersive micro Laue X-ray diffraction. Detailed description of the method is presented along with a demonstration experiment performed on a micro copper cantilever. The experiment is performed at beamline BM32 of the European Synchrotron Radiation Facility in Grenoble, France.

4.3.1 Laue diffraction

Laue diffraction is a classical X-ray technique which has been extensively used since the discovery of X-ray diffraction by Max Von Laue in 1912. Prior to Von Laue, William Lawrence Bragg derived the formalism of constructive interference of X-rays scattered from a crystalline material. To understand the formulation of Bragg's and Von Laue's works, it is necessary to introduce the mathematical definition of a crystalline material.
A crystalline material is mathematically defined by a basis attached to a lattice. Each lattice point is accessed by a vector in real space and can be written as in equation 4.16:

$$\overrightarrow{r} = n_1\overrightarrow{a_1} + n_2\overrightarrow{a_2} + n_3\overrightarrow{a_3} \tag{4.16}$$

where n_1, n_2, and n_3 are integers and $\overrightarrow{a_1}$, $\overrightarrow{a_2}$ and $\overrightarrow{a_3}$ are the lattice vectors.
In the reciprocal space, the lattice points are accessible through the reciprocal lattice vector $\overrightarrow{G}$ which consist of a linear combination of the reciprocal lattice vectors $\overrightarrow{b_1}$, $\overrightarrow{b_2}$ and $\overrightarrow{b_3}$ as in equation 4.17:

$$\overrightarrow{G} = h\overrightarrow{b_1} + k\overrightarrow{b_2} + l\overrightarrow{b_3} \tag{4.17}$$

Atoms that are arranged in a periodic crystalline form, scatter X-rays efficiently

when the X-ray wavelength and incident angle satisfies the Bragg condition as in equation 4.18:

$$\sin\theta = \frac{\lambda}{2d_{hkl}} \tag{4.18}$$

where λ is the X-ray wave length, d_{hkl} is the spacing between the lattice planes (hkl) and θ is the angle between the lattice planes (hkl) and the incident beam. For a cubic crystal the lattice spacing d_{hkl} is defined as in equation 4.19:

$$d_{hkl} = \frac{a}{\sqrt{h^2 + k^2 + l^2}} \tag{4.19}$$

The Bragg equation allows for bright constructive interference only when the X-rays are specularly reflected.
The restriction on the specular reflectance is schematically represented in figure 4.15 by the *Ewald Sphere Diagram* which shows the momentum transfer for all possible scattering directions.

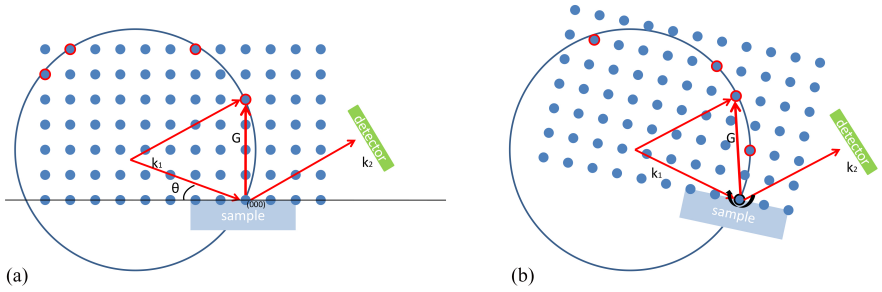

Figure 4.15: (a) Two dimensional representation of the Ewald Sphere for a cubic unit cell. The Ewald Sphere representing the X-ray momentum transfer have a small probability to intersect a reciprocal lattice point (satisfy a Bragg condition). (b) If the sample is rotated the reciprocal lattice points rotate too, increasing the number of lattice points intersecting the Ewald Sphere (marked with red outline).

The radius of the *Ewald Sphere* is inversely proportional to the incident X-rays wavelength, and in case of elastic scattering it is equal to the scattered wave vector magnitude, i.e. $\mid k_2 \mid = \mid k_1 \mid = \frac{2\pi}{\lambda}$.
Von Laue conditions on constructive interference states that *constructive interference will occur provided that the change in the wave vector $k_2 - k_1$ is a vector of*

the reciprocal lattice. This is called the Ewald construction shown in figure 4.15, whereas the Laue condition is represented in equation 4.20:

$$| k_2 - k_1 | = | G | \Leftrightarrow \vec{k_1} \cdot \vec{G} = \frac{1}{2} G \tag{4.20}$$

Both the Laue conditions and the Bragg equation are equivalent, thus *"a Laue diffraction peak corresponds to a change in the wave vector given by the reciprocal lattice vector G corresponds to a Bragg peak from the family of direct lattice planes perpendicular to G. The order, n, of the Bragg peak is just the length of G divided by the length of the shortest reciprocal lattice vector parallel to G"* [30]. Exposing the sample to white X-rays increases the number of the reciprocal lattice points that intersect the Ewald sphere as seen in figure 4.16.

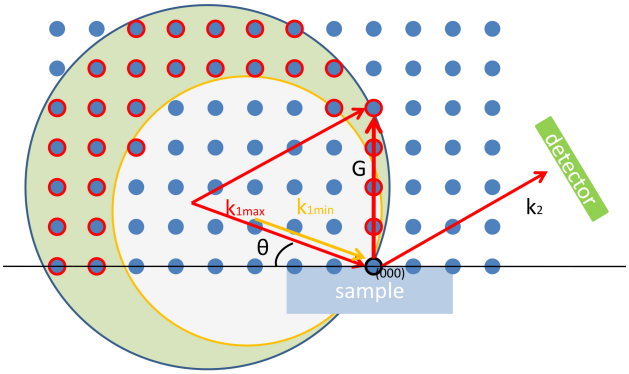

Figure 4.16: Polychromatic diffraction using a broad range of wavelength increases the number of diffraction spots.

4.3.2 The need for white-beam microdiffraction

The Laue approach is primarily applied to determine crystal structures by collecting Laue patterns on photographic films and later on electronic 2D detectors. The main drawback of the Laue technique so far is that Laue patterns are recorded by energy-insensitive detectors which significantly limit the experimentally available information. For this reason, precise X-ray structure analyzes are nowadays carried out by monochromatic techniques using pixel array detectors and rotating the crystal. In recent years a series of attempts have been performed to utilize an energy dispersive 2D detector in single shot Laue diffraction experiments [5, 11].

In material science, the Laue technique has predominantly served to determine the crystallographic orientation of single crystals and to analyze micro-structural changes accompanying plastic deformation of metals. In the last 15 years, polychromatic μLaue diffraction has gained significant attention since micro structure and strain within small crystalline domains can be investigated with sub-micron resolution [31, 32]. The information provided by this method is manifold: Beside the crystal orientation and deviatoric strains [33] also densities of geometrically necessary [1, 34, 35] dislocations can be evaluated with high lateral resolution. Primarily, the technique was used to investigate the strain distribution in semiconductors [33, 36], stress-induced grain-boundary motion [37] and micro-structural phenomena accompanying plastic deformation on the sub-micron scale [38–40].
However, one major drawback of μLaue diffraction exists: Due to the use of polychromatic X-rays, the energies of individual Bragg peaks recorded by 2D energy-insensitive X-ray detectors remain unknown. This makes the simultaneous determination of the crystallographic unit cell, hydrostatic strain components as well as statistically stored dislocation currently very difficult or impossible. In order to overcome this problem, a tunable monochromator can be inserted into the primary beam path [32, 41] which defines the energies of the Laue spots collected by means of a charge-coupled device (CCD). This procedure is time-consuming and often leads to a movement of the footprint of the beam on the sample. Alternatively, Robach and co-workers recently presented a tunable multicolor filter which allows determining the energy of selected Bragg peaks by means of a diamond single crystal fading out distinct energies from the primary beam spectrum [42]. This relatively fast technique can be used to obtain the full strain tensor. However, an analyzes of statistically stored dislocations (SSDs) is still not possible with high accuracy.
Both aforementioned methods alter the primary beam spectrum by either selecting or removing some wavelengths. Alternatively, the wavelength filtering can also take place on the secondary side of the diffraction experiment (sample downstream) which does not influence the footprint and the properties of the primary beam on the sample. Robach and co-workers also used a fully equipped μLaue diffraction setup including an energy-dispersive point detector system on a movable cross-table to measure the energies of individual Laue spots recorded by a

CCD [43]. This approach is believed to be the first technique by which the full strain tensor can be calculated based on energy filtering on the secondary side. However, this method requires time in the order of a minute to record and index the Laue pattern, to move the point detector to the position of a selected Bragg peak and to perform an energy scan. Furthermore, it does not allow to characterize the energy distribution across topologically complex Laue spots observed e.g. in the case of plastically deformed metals. The use of energy-dispersive area detectors for μLaue diffraction could overcome all the above mentioned experimental restrictions.

4.3.3 Theory of deformation in metals: The influence on reciprocal space [1]

Krivoglaz [44] developed a qualitative classification of crystal defects based on an analysis of the Debye-Waller Factor (DWF) exponent, e^{-2W}. In a perfect crystal the DWF is the Fourier transform of the position of the atoms. This takes into account harmonic and anharmonic vibrations of the lattice points. In non ideal crystals the DWF exponent takes into account the static displacements of the lattice points due to defects. The value of DWF is either finite or infinite depending on the type of defects. A comprehensive description is found in [44]. Equation 4.21 is first approximation of the DWF near a defect.

$$2W = ReT_{\infty} \cong c \lim_{\rho \to 0} \sum_{t} [1 - cos(Qu_{ss't})] \left[1 + \frac{1}{f}(\phi_{st} + \phi_{s't}) \right] \tag{4.21}$$

where T_{∞} is the correlation function for defects at large distances, c is the concentration of defects, f is the structure factor for the average crystal, Q is the momentum transfer for certain (hkl) reflection, $u_{ss't}$ is the difference between displacements in two scattering cells s and s' caused by the defect located in the position t, ϕ_{st} and $\phi_{s't}$ describe structure amplitude changes of scattering cells s and s' caused by defects located in the position t [1].
According to Krivoglaz defects can be classified into:

- Defects of 1st kind, where the Bragg peak intensity is reduced whereas the

peak remains sharp. 1st kind deformations can also cause a displacement of the peak position in the reciprocal space if compared to an ideal non-deformed crystal. Moreover, diffused scattering intensity is increased with defects concentration.

- Defects of 2nd kind. This kind of defects broaden the Bragg peaks mending them anisotropic in reciprocal space. The broadening increases with defects concentration.

1st kind	2nd kind
Point defects	**Dislocations**
Coherent precipitates	**Disclinations**
Small dislocation loops	**Planer defects**
	•*grain boundaries*
	•*cell boundaries*
	•*stacking faults*
	•*twins*
Defects small compared to crystal	**Large dislocation loops**

Table 4.4: Classification of defects.

The formation of dislocation networks of dislocations is the main mechanism in which crystals deform [45,46]. Dislocations may be randomly distributed or may group together on large length scales. Statistically stored dislocations (or SSD) are random dislocations with equal number of positive and negative Burgers vectors. SSDs are also called paired dislocations. Geometrically necessary dislocations (or GND) are unpaired dislocations of excess number of Burgers vectors of one sign. GNDs may group into cells and walls. GNDs usually cause streaking in the Laue spots intensity distribution. GNDs can be individual, Incidental Dislocation boundaries (IDB) or Geometrically necessary boundaries (GNB). The last may form dense dislocation walls (DDW) or double walled microbands (WM) if the strain is small. During initial stages of deformation dislocations are randomly distributed. However, in case of strain gradients (in the case of plastic deformations) dislocations favor one sign of the Burgers vector on another and the result

is a correlated bending of the lattice planes. When the strain is large, GNBs form lamellar bands. At high strains complex distributions will form.
In crystals GNDs tend to group into walls in order to reduce strain energy. This can be seen from the stored elastic energy per unit length of one dislocation:

$$\frac{E}{l} \approx \frac{\mu n b^2}{4\pi} \log[\frac{L}{b}] \tag{4.22}$$

where E is the integrated elastic energy, L is the probed length (beam on sample), μ is the shear modules, n is total dislocation density and b is the modulus of the Burgers vector.

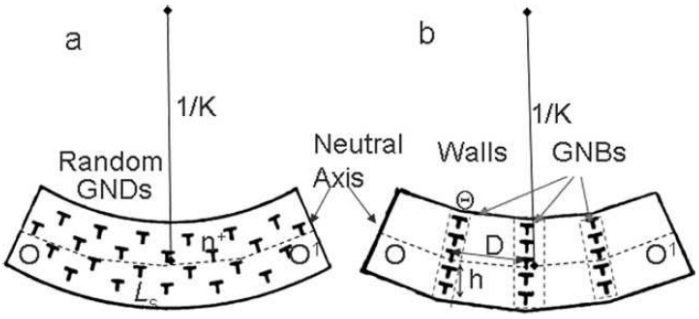

Figure 4.17: Crystal rotation due to random GNDs (a) and with GNBs (b) [1].

4.3.4 Dislocations influence on the scattering intensity

Dislocations change the diffraction conditions for a set of hkl planes. Therefore, the position of the Bragg peaks changes accordingly. The scattering intensity I(q) from a set of hkl planes is a function of the diffraction vector $Q = k_1 - k_0$ where k_1 and k_0 are the reflected and incident wave vectors or it is a function of the deviation vector $q = Q - G_{hkl}$. It is also a function of the correlation function T and can be written as follows:

$$I(q) = f^2 \sum_{i,j} \exp iq.\delta \exp -T \tag{4.23}$$

f is the average scattering factor, δ is the undistorted distance vector between lattice cells i and j and T is determined by the following equation according to [44]:

$$T = nS_0 \sum_t 1 - \exp iQ.(u_{it} - u_{jt}) = c \sum_t 1 - \exp iQ(u_{it} - u_{jt}) \tag{4.24}$$

S_0 is defined as one dislocation position in the transverse plane, n is the total dislocation density, u_{ij} is the displacement of the ith cell due to dislocation at lattice site j.

To understand this, two directions in the q-space are defined, $I(q_{\|})$ and $I(q_{\perp})$. $I(q_{\|})$ describes the shape of the intensity distribution and would change as a result of local variations in the lattice spacing as seen in figure 4.19 (a). Whereas $I(q_{\perp})$ describes the intensity in the transverse direction which depends on lattice rotations caused by defects, figure 4.19 (b).

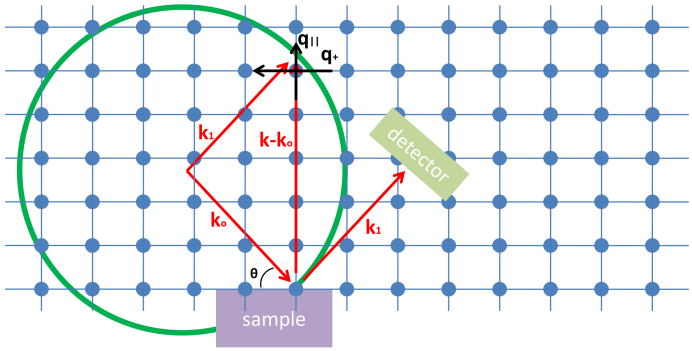

Figure 4.18: Reciprocal space and diffraction conditions

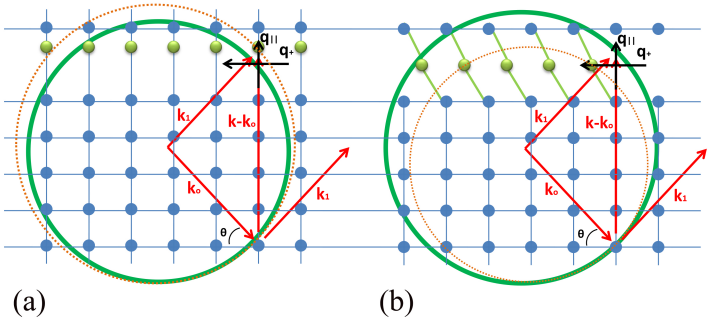

Figure 4.19: (a) Lattice spacing cause $I(q_{\|})$ to change where as (b) lattice rotations cause $I(q_{\perp})$ to change.

Broadening in the radial direction can be understood as variations in the lattice spacing caused by local strain fields [44]. Changes in the transverse direction can be understood as a result of lattice defects that cause rotation in the lattice planes. In detail a description of the influence of different dislocation type on the reciprocal space intensity I(q) is given below in the next paragraphs.

SSDs are paired dislocations and therefore an equal number of randomly distributed Burgers vectors of positive and negative signs will average up over several unit cells. **GNDs** on the other hand, are separated into **random GNDs**, **GNBs** and **GNBs + IDBs**. GNDs cause lattice rotations. This changes the intensity distribution of the Laue spots and cause them to be streaked. The orientation of the streaks depends on the orientation between the GNDs slip systems and the diffraction vector as seen in figure 4.20.

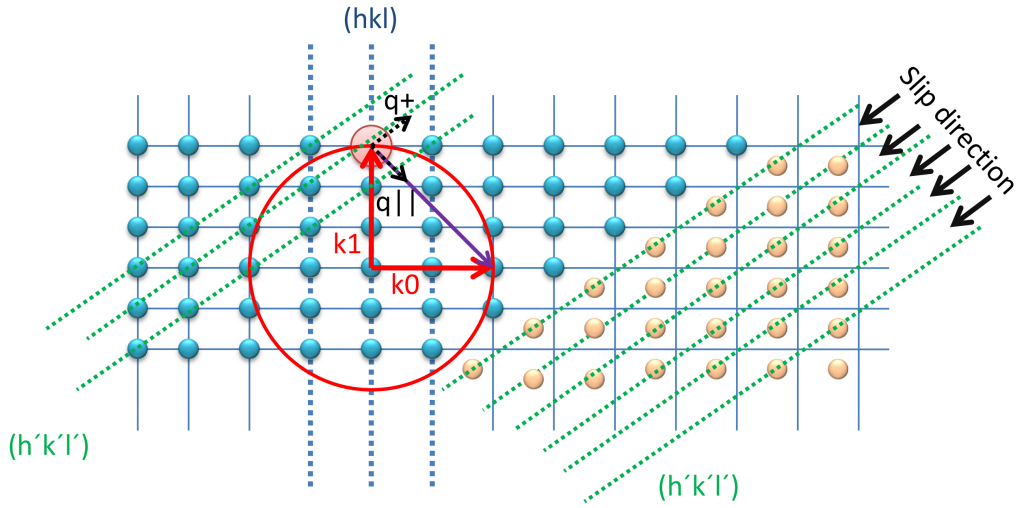

Figure 4.20: The effect of the slip system orientation relative to the diffraction vector G.

The FWHM of the Laue spots in the radial and transverse directions is a measure of the total dislocation density [1]. Laue spots can also split into two or more distinguished spots. This happens when the incident beam is reflected from multiple distinct cell blocks within the probed volume of the sample. Each cell block of a defined size will contribute to the scattered intensity, when the misorientation of the cell blocks exceeds the mean FWHM of the Laue image, the Laue spot splits.

Below is a summery of Laue spots shape dependence on the dislocation type.

- In case of **SSDs**, the shape of Laue spots shape is almost isotropic, figure 4.21(c).
- For random **GNDs** the Laue spot shape exhibits a Gaussian distribution in one direction and a Gaussian with a flat top in the other direction "flat-top-Gauss", figure 4.21(e).
- **IDBs** modify the shape of the Laue spots, such that it can be described by an almost isotropic Gaussian with FWHM increasing proportionally with the density of dislocation and the cell sizes.
- **Paired GNDs** allow for spikes in the Laue spot exhibiting a Lorentz distribution intensity profile, figure 4.21(a).
- **Unpaired GNDs** cause the Laue spot to be streaked, figure 4.21(f).
- **Gradient of GNDs** Anisotropic stream with max at one end,figure 4.21(b).

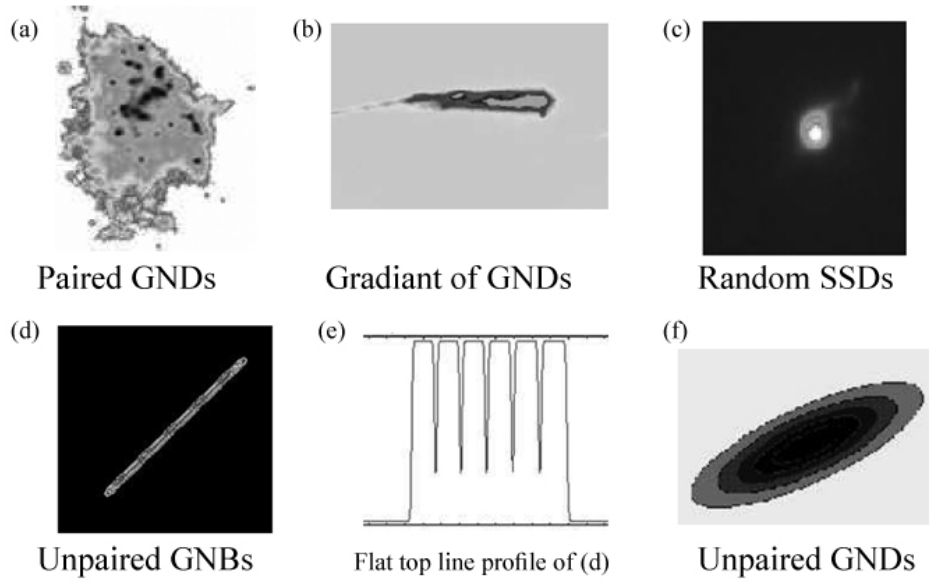

Figure 4.21: The effect of the slip system orientation relative to the diffraction vector G [1].

4.3.5 Diffraction from a deformed Copper cantiliever: Experimental setup and the pnCCD settings

The experiment was performed at the μLaue end station of the CRG-IF beamline of the European synchrotron radiation facility ESRF located in Grenoble, France. Stationed at a bending magnet, the distance between the source and the sample was about 59.51 m [47]. Focusing optical elements were placed at a distance of 28 m and at 59 m from the source, figure 4.22:

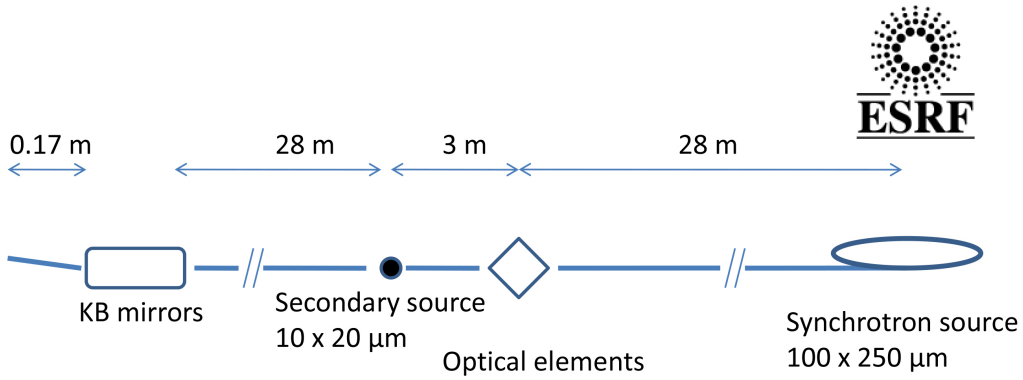

Figure 4.22: Sketch of the beamline with the focusing optical elements.

The brilliance of the bending magnet (@200 mA, 6 GeV and 0.8 T) is 10^{14} $photons \cdot \sec^{-1} \cdot mrad^{-2} \cdot mm^{-2} \cdot 0.1\%$BW. The angular acceptance of the optical elements cuts the bending magnet spectrum to a bandwidth between 5 and 25 keV. The flux of photons of the white beam at the sample position is $10^{10} photons\,\sec^{-1}$ and the shape is shown in figure 4.23.

Two Kirkpatrick-Baez (KB) optics were used to achieve a sub-micrometer beam size at the sample surface. Two mirrors aligned perpendicular to each other are elliptically curved to achieve a common focal point, figure 4.24. The KB mirrors can produce focused spots in the 50 nm range. However, the image of the source in the focal spot degrades as the source size increases. This is understood as the KB mirrors do not fulfill the Abbe criterion, [48].

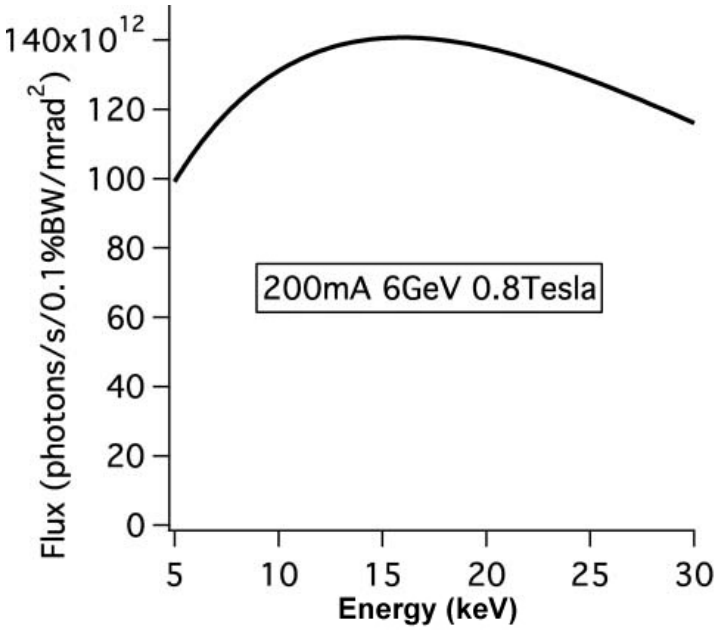

Figure 4.23: Calculated energy spectrum of the BM32 bending magnet.

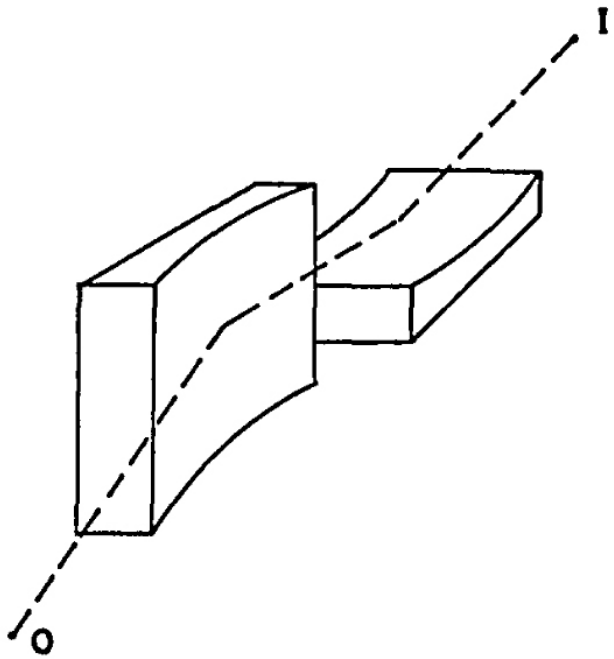

Figure 4.24: Allignment of the KB mirrors with respect to each other, [48].

A 384 x 384 pixels eROSITA frame-store pnCCD is used for the present experiment. Square pixels of side length 75 µm form the image area. Smaller pixels of dimension 75 x 51 µm form the charge storage area. The detector operates at 230 V back voltage to achieve full depletion of a 450 µm thick silicon substrate. 3 DUO CAMEX chips read the pnCCD signal at a frame rate of 87 frame/s. The pnCCD chip is mounted on a ceramic plate which in turn is connected to a copper cooling mask using a thermocouple grease. The charge signal is transported for further treatment through a flex lead connection, figure 4.25.

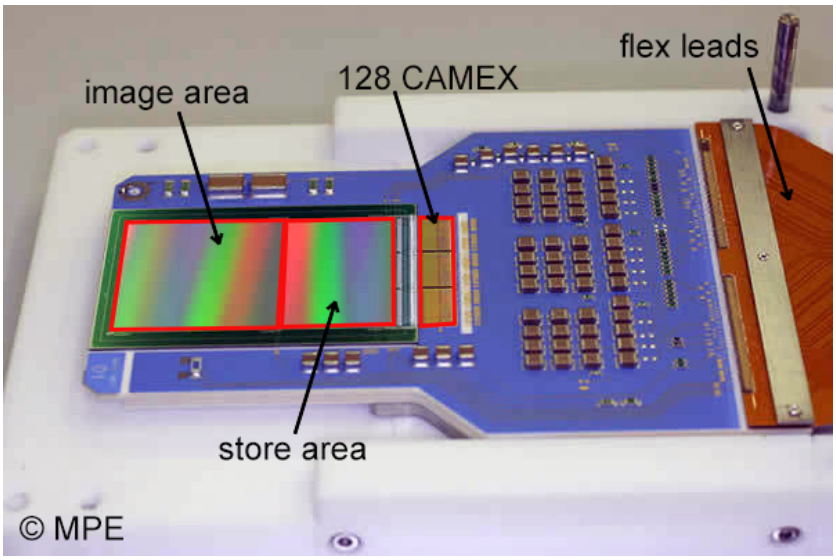

Figure 4.25: 384 X 384 pixels eROSITA type pnCCD.

The pnCCD is housed in a vacuum chamber under low pressure (10^{-4}mbar). An upgrade of the previously installed cooling system (see ML setup) is used to reduce mechanical vibrations created by the predecessor cooling fluid compressor. A "Polycold Systems" of the type "CRYOTIGER" is used to reduce the pnCCD chip temperature to 200 K . The system uses a helium mixture (NF-Gas) as a coolant.

The BM32 beamline is equipped with a MAR LAUE CAMERA. However, placing the pnCCD with its 20 cm diameter chamber has proven to be challenging, as shown in the figure 4.26. The size of the pnCCD chamber denies the possibility to move closer to the sample and hence the solid angle is limited to 20 degrees. A schematic of the experimental setup is shown in figure 4.26 and 4.27.

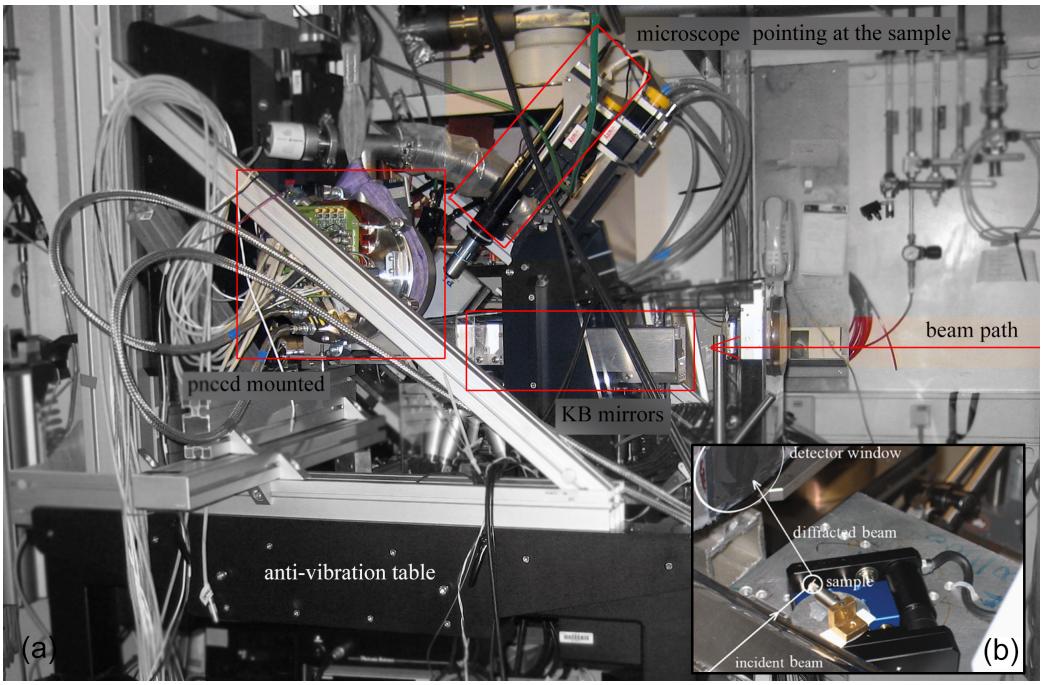

Figure 4.26: (a) Picture of the experimental hutch with the pnCCD mounted. (b) Close up of the sample mount showing the diffraction geometry.

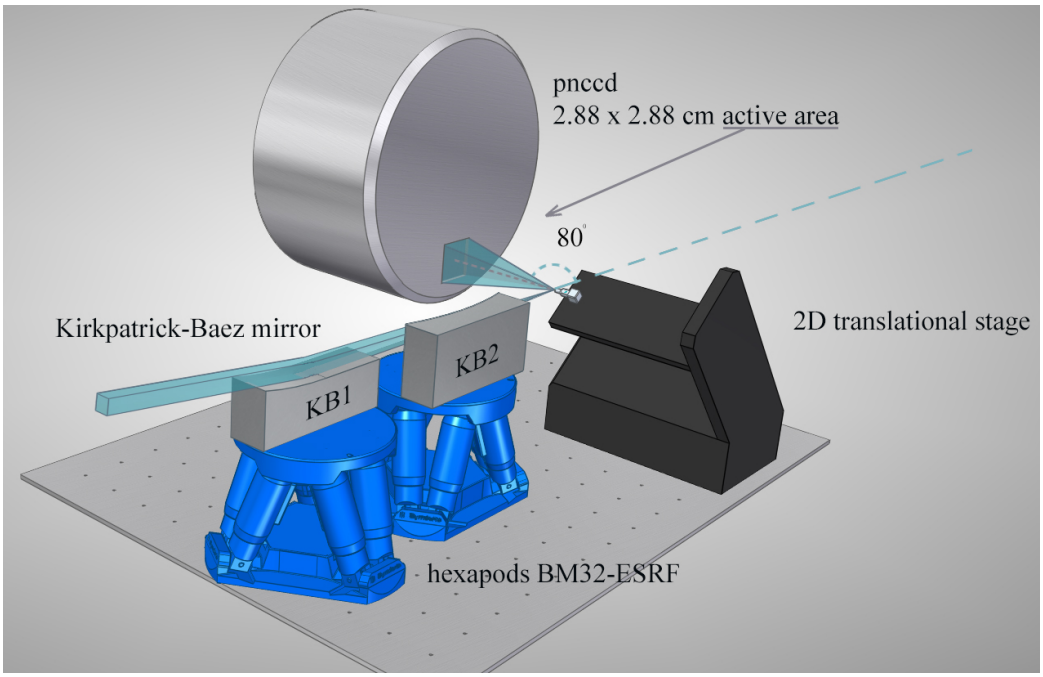

Figure 4.27: Experimental setup for energy-dispersive μLaue diffraction at the BM32.

4.3.6 Sample description and measurement methodology

The sample used is prepared from a single crystalline copper block and cut down to a smaller size of few millimeters. [3]. The shape and size is then reformed by focused ion beam milling until a final size of 6 x 6 x 30 μm^3 is reached. The shape of the sample is shown in figure 4.28. The crystal structure is face-centered cubic with the lattice constant a = 3.615 Å. Prior to the experiment, the sample is deformed in-situ during a polychromatic μLaue experiment at the same beamline and is monitored by a MarCCD [49]. The in-situ experiment yielded a Laue pattern with 27 individual reflections which are used to determine the crystallographic orientation of the sample as shown in figure 4.28.

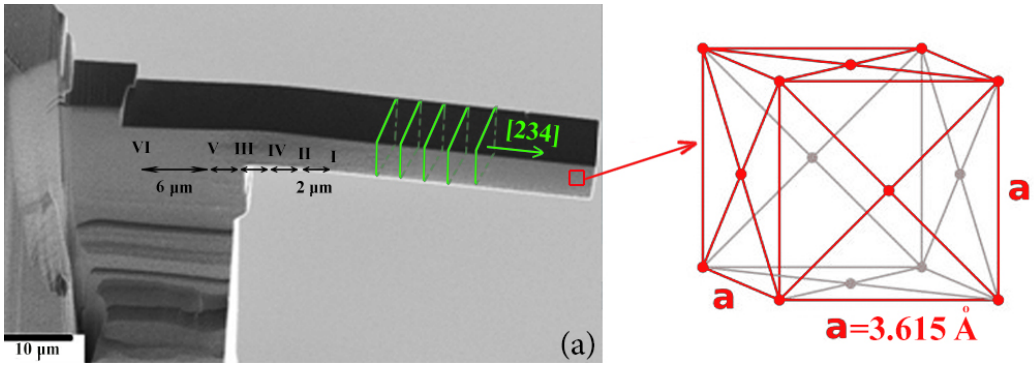

Figure 4.28: Scanning-electron micrograph of the deformed Cu micro-cantilever.

In the present measurement, the sample is investigated with a pnCCD by scanning along the neutral axis of the cantilever. The step size of the line scan is 2 μm in the deformed area with sample positions labeled as I-V, figure 4.28. In the sample base region, the diffraction signal is measured at position VI located 6 μm below position V as seen in figure 4.28.

4.3.7 Results: Laue spots in 3 Dimensions

At every beam position on the sample surface (I-VI) an X-ray exposure that lasted for 50,000 frames (9.36 min) is recorded by the pnCCD detector. The scattered

[3]Sample is provided by Christoph Kirchlechner: MAX-PLANCK-INSTITUT FÜR EISENFORSCHUNG GmbH

X-ray beam contains coherent scattering (diffracted signal) and fluorescence radiation produced when the incident and reflected beam interacts with objects in or close to its path, such as sample alignment motors and pnCCD housing chamber. Fluorescence produced by the sample are also collected. All the photons that inter the detector bulk trigger one or many pixels as discussed in the previous chapters and can be assigned a 3D matrix of the form I(x, y, E) where x ϵ [0-383], y ϵ [0-383] and E ϵ [0-16383] representing the event in x and in y location and the amplitude value taken in a digital unit (a.d.u.).The energies of these reflections are determined by extracting the energy spectra detected in quadratic areas with a size of 5 x 5 pixels around the Laue spots centers and fitting the spectral peaks to a Gaussian distribution.

Due to the small lattice constants of the sample and the experimental constrains for the detector position, only two Bragg peaks are observed centered at the pixel positions (207, 240) and (350, 131). Taking into account the measured energies of 14.9 keV and 18.6 keV (figure 4.29) the Bragg peaks are identified as the Cu 511 and Cu 711 reflections with the inter-planar spacing distances of d_{511} = 0.70 Å and d_{711} = 0.51 Å, figure 4.30. The measured angular distance between the two spots is about 4.30° which fits well with the theoretical angular distance of 4.37° between the (511) and (711) lattice planes. Table 4.5 lists several parameters of the detected reflections including the normalized intensity and the detector quantum efficiency at the reflections energies.

(hkl)	Energy (keV)	d Å	$\|F\|_{theo}$	(x,y)	I/I_{max}%	QE %
511	14.9	0.7	17.3	(207, 240)	23.1	63
711	18.6	0.51	11	(350, 131)	9.3	40

Table 4.5: Summery of the Cu 511 and 711 reflections properties. $|F|_{theo}$ is the theoretical structure factor of the 511 and 711 reflections.

The projections of the 3D data volume into the (x,E) and (y,E) side planes indicate the energy information contained in the recorded data set. The diffraction signal of the crystal gives rise to sharp peaks at the energies of the Cu 511 and Cu 711 reflections accompanied by a homogeneously distributed background. This background signal contains Cr, Fe and Cu fluorescence lines originating from the

sample, the sample holder and the detector housing as well as a continuum of photons scattered by air molecules.

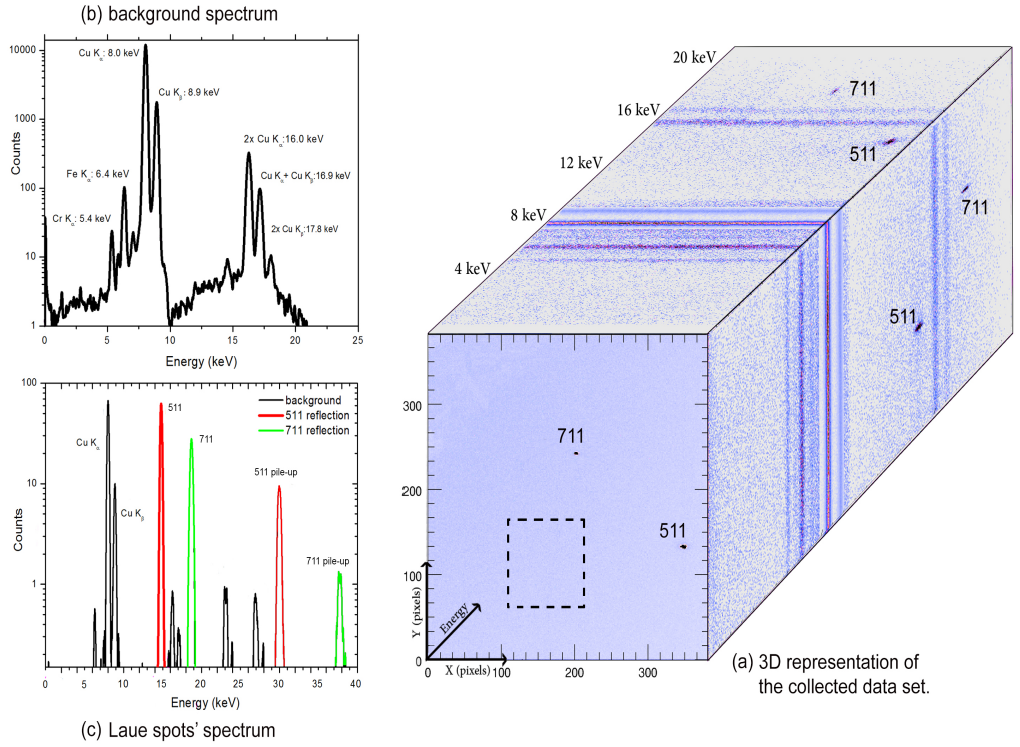

Figure 4.29: Visualization of the 3D intensity distribution I(x,y,E) recorded at the sample position VI including the identified Cu 511 and Cu 711 Bragg peaks. (a) In order to extract structural information from this measurement, I(x,y,E) was projected into each of the three interfaces of the data volume. The blue vertical and horizontal lines represent X-ray fluorescence signals of Cr, Fe and Cu. (b) energy spectrum of the background extracted from the quadratic area with a size of 100 x 100 pixels marked in (a) (dashed box). (c) Energy spectra recorded within regions of 5x5 pixels around the 511 and 711 reflections. The spectral peaks at 29.8 keV *and 37.2* keV *are pile-up signals of diffracted photons, whereas the peaks at 22.9* keV *and 26.6* keV *originate from overlaps of diffracted photons with the Cu K_α fluorescence line.*

In particular, the fluorescence signals correspond to spectral peaks with the energies 5.4 keV (Cr K_α), 6.4 keV (Fe K_α), 8.0 keV (Cu K_α) and 8.9 keV (Cu K_β) (Fig. 4.29(b)) resolved with FWHM of 187 eV, 218 eV, 225 eV and 236 eV, respectively. Moreover, the depicted energy spectrum reveals that the background is dominated by the intense Cu K-lines giving rise to pile-up signals at the energies

16.0 keV, 16.9 keV and 17.8 keV. Figure 4.29(c) shows the superimposing signal of the Cu 511 (red curve) and the Cu 711 (green curve) reflection, respectively. The additional peaks at 23.9 keV and 24.8 keV are pile-up signals of the diffracted photons and the Cu florescence lines.

An X-ray Laue pattern is simulated for the Cu crystal that shows the 511 and 711 reflections in the striped red square representing the position of the pnCCD detector and the direction of the beam with respect to the crystal axis. The two insets (b) and (c) show the layout of the sample seen from the side and the crystal axis with respect to the beam respectively.

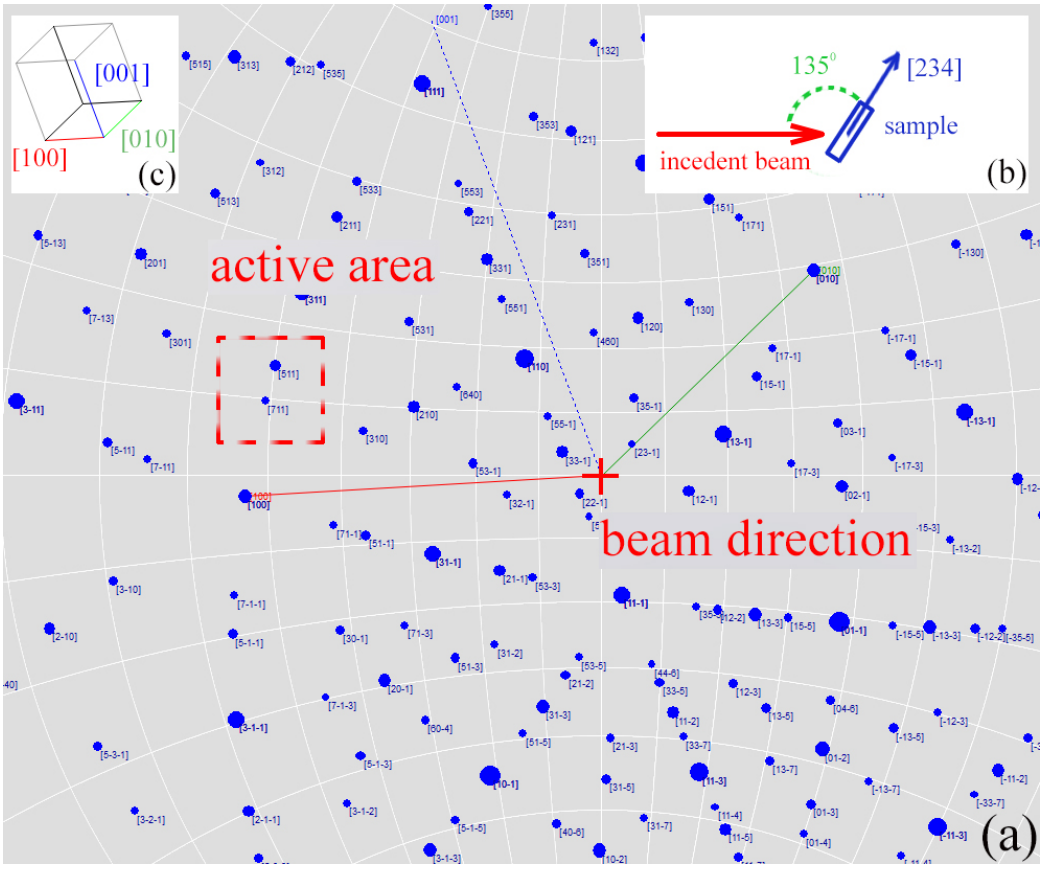

Figure 4.30: (a) Simulation of the Laue experiment presented on a Wulff net (with forbidden reflections). (b) The unit cell relative to the incident beam perpendicular to the surface. (c) Schematic of the setup showing the incident beam angle to the [234] direction vector.

4.3.8 Geometrically Necessary Dislocations

In order to quantitatively analyze the response of different parts of the crystal to deformation, the shape and the energetic structure of the Cu 511 and Cu 711 reflections were studied for the various measurement positions at the specimen. Figure 4.31 displays intensity maps of the two Laue spots recorded by the pnCCD which show the spatial evolution of the diffraction signal for displacements of the Cu-cantilever along the scan direction according to the sample positions I-VI defined in figure4.28.

For positions I and VI, the Laue spots are sharp in space and spread over an area of roughly 5 x 5 pixels. The diffraction signals from undeformed sample regions are collected in both cases. Applying a 2D Gaussian fit to the intensity distribution of the Cu 511 reflection at sample position I gives the standard deviations $\sigma_x \approx \sigma_y \approx$ 1 mrad corresponding to about one pixel width in horizontal and vertical directions. Moving on the sample to positions II-V, the Laue spots become elongated in space and spatially broadened in different directions (positions II and III). At sample position III, the streaking of the Bragg peak is expressed in terms of the standard deviations $\sigma_x \approx 5.6$ mrad and $\sigma_y \approx 0.8$ mrad. Further displacements of the sample to positions IV and V result in fragmentations of the 511 and 711 reflections.

In the previous sections the evolution of a sharp Gaussian Laue spot to different shapes including streaks and fragments was discussed in details. The streaking behavior of the Laue spots is associated with strong strain gradients [1]. Another feature that is the direction of the streaks in the q-space. The red line in the surface plots of figure 4.30 indicates that the direction of the slip planes relative to the reciprocal lattice vector is also changing, which is a result of the formation of paired GNBs at positions IV and V. The features measured at spot position III indicates the formation of unpaired GNBs.

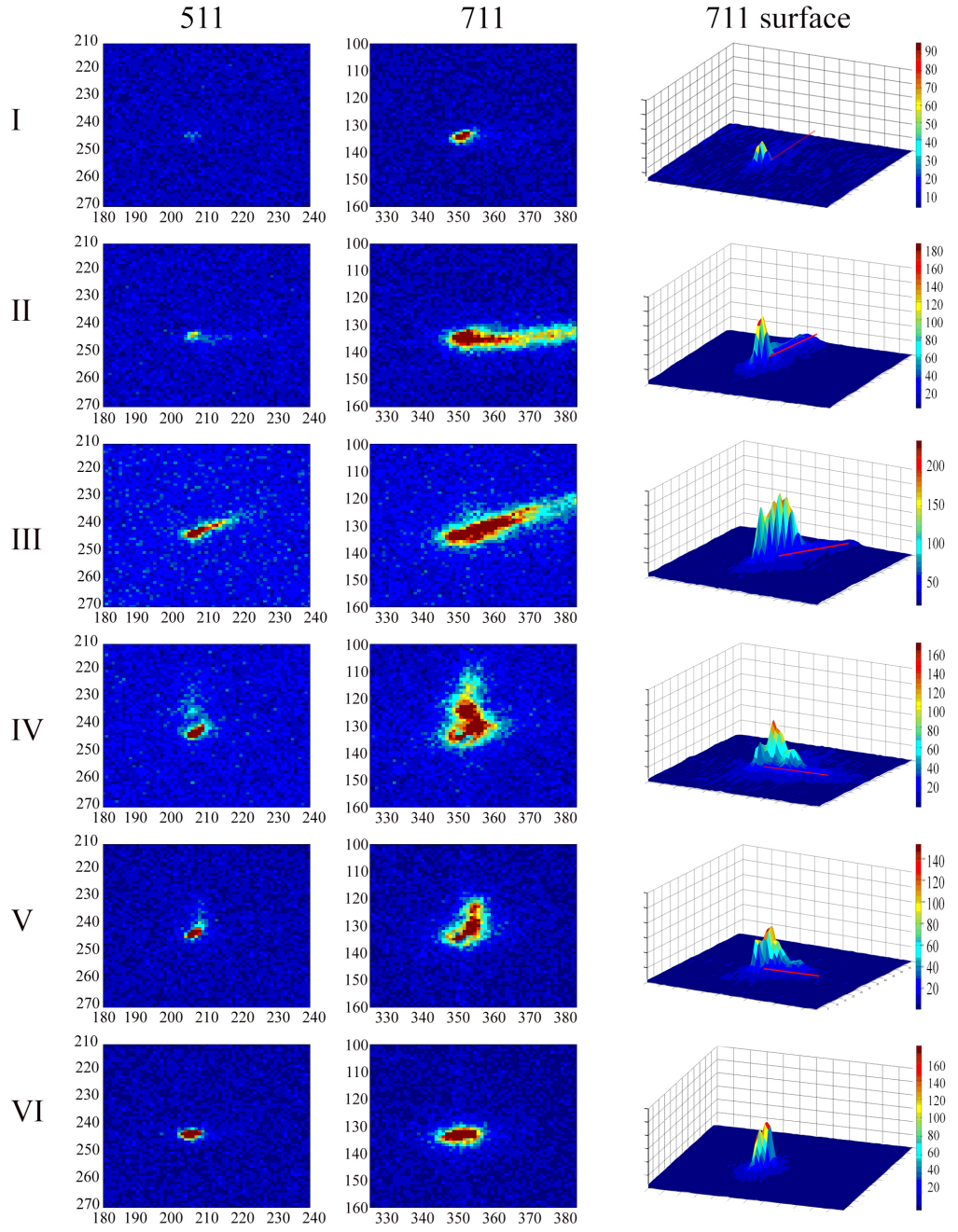

Figure 4.31: Spatial evolution of the Cu 511 and Cu 711 reflections within the detector plane along the scan direction as a result of different micro structure. The sharp spot shapes at positions I and VI correspond to signals from an undeformed Cu crystal whereas streaking (positions II and III) and fragmentation (positions IV and V) are obtained in the case of plastic deformation. The maximum degree of deformation, which is characterized by the presence of stored GNDs in the deformed region, can be observed at sample position III.

The advantages of the pnCCD as a 2D energy dispersive camera, is in measuring of the energy variation along a streak. At every sample position, the spatial shape of the Bragg peaks can be associated with a measurable energy profile. In order to visualize the energetic structure of the reflections, an energy spectrum from a quadratic mask with a size of 2 x 2 pixels (figure 4.32) is extracted. At each position of the mask, enumerated as 1-5 in figure 4.32(a), the energy spectrum is extracted and used to fit the energy of the Bragg peak. Figure 4.32(b) shows an example of this procedure where the energy profile of the 511 reflection was calculated along the streaking direction by fitting the Bragg peak with a Gaussian function over a region of interest between 14.2 keV and 15.7 keV.

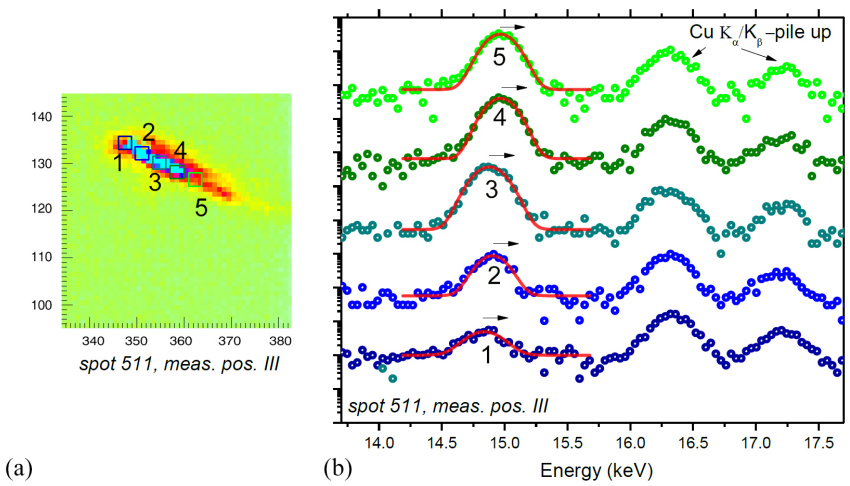

Figure 4.32: (a) 2 x 2 pixel mask used to calculate the energy profile of the Cu 511 reflection along the streaking direction for sample position III. (b) Corresponding energy spectra recorded within the quadratic regions 1-5 indicated in (a). The shapes of the Bragg peak can be well approximated by Gaussians (red curves). A shift of the spot energy towards higher energies along the streaking direction is clearly visible.

The average FWHM of the fitted Gaussians amounts to about 260 eV. The results of this procedure applied to the Cu 511 reflection at every sample position are summarized in figure 4.32 where the spot energy is plotted as a function of the diffraction angle. The same procedure is performed for the Cu 711 reflection leading to comparable results. Thus the data in figures 4.33 and 4.34 allow to correlate the streaking of the individual Laue spots in the detector plane with the corresponding energy shifts along the streaking direction.

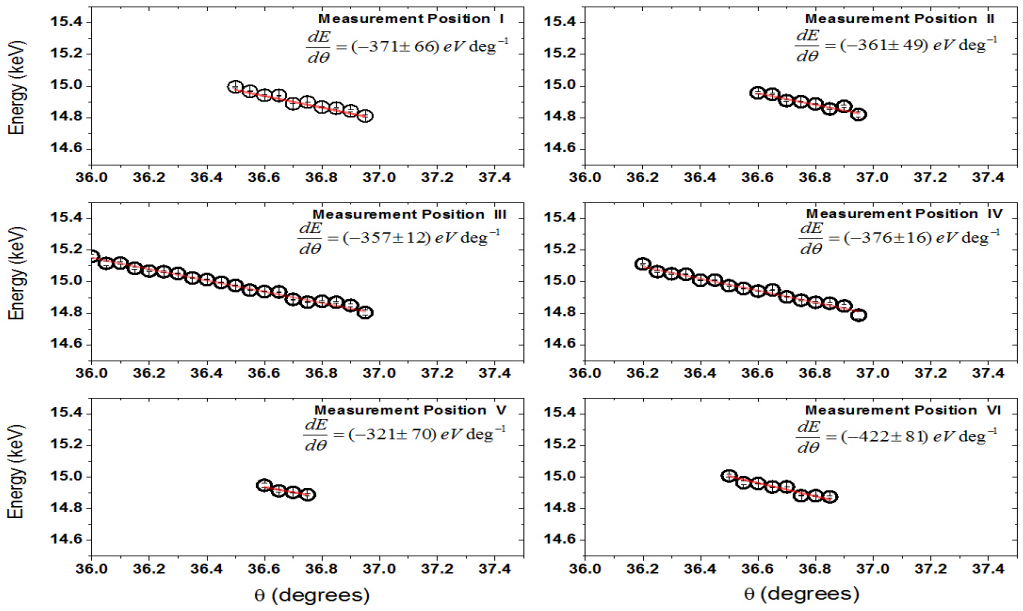

Figure 4.33: Fitted energy of the 511 reflection, evaluated from the energy spectra measured at different streak positions (cf. Fig. 4.32).

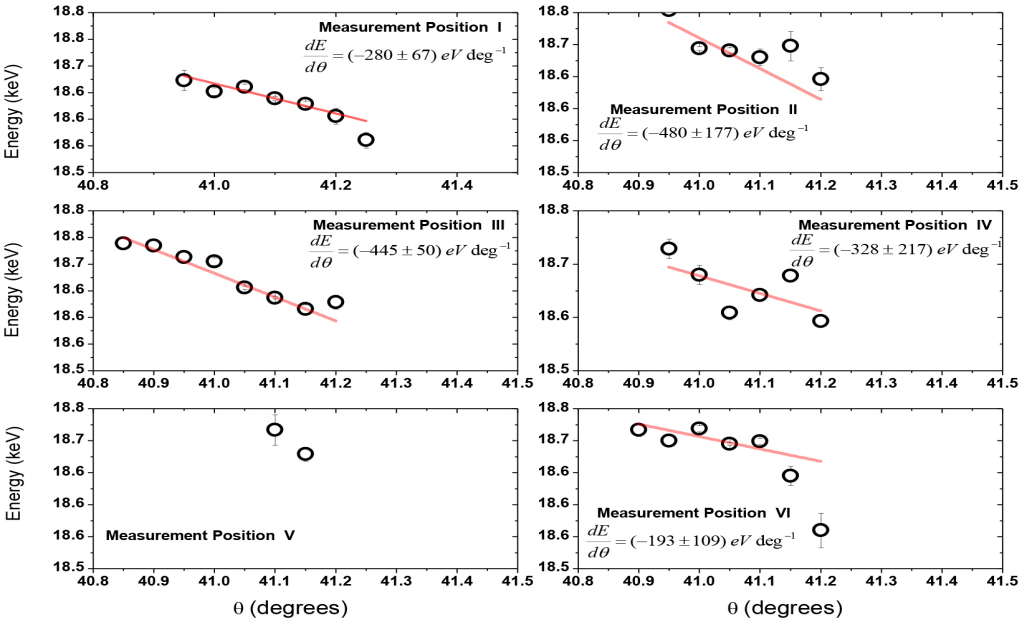

Figure 4.34: Fitted energy of the 511 reflection, evaluated from the energy spectra measured at different streak positions (cf. Fig. 4.32).

4.3.9 Possible deformation scenarios

As already observed in Laue diffraction experiments without the use of energy-resolving detectors, the Bragg peaks originating from plastically deformed regions of the sample are streaked [50]. The streaking of the Laue spots can be attributed to (i) the local lattice rotations caused by the formation of GNDs on distinct slip systems or (ii) deviatoric elastic strain gradients. The latter case is typically neglected in the case of Laue streaking analyzes using monochromatic radiation, however, it can become dominant for samples below a certain size. To unravel both, the full spatial and energetic structure of the Bragg peaks is required [1].
The present experiment clearly demonstrates that each point along the streak is associated with a small shift of the reflected energy. A linear fit of the $E(\theta)$ distribution depicted in figure 4.33, as an example, yields a slope of (-357 ±12) eVdeg^{-1} for the Cu 511 reflection detected at sample position III. After conversion from the conventional wavelength description into the energy description, Bragg's law can be expressed as:

$$E = \frac{hc}{2d_{hkl,\epsilon} \sin\theta} \tag{4.25}$$

where h is Plank's constant, c the speed of light, $d_{hkl,\epsilon}$ the lattice spacing and θ the angle of incidence in reference to the diffraction lattice plane (hkl). The first derivative of equation 4.25 with respect to θ would give:

$$\frac{dE}{d\theta} = \frac{-hc \cos\theta}{2d_{hkl,\epsilon} \sin^2\theta} \tag{4.26}$$

Equation 4.26 is used to estimate the expected energy shift for four different anisotropic linear elastic scenarios. These scenarios are based on the magnitude of the stress tensor components σ:

$$\sigma = \begin{pmatrix} \sigma_{11} & \sigma_{12} & \sigma_{13} \\ \sigma_{21} & \sigma_{22} & \sigma_{23} \\ \sigma_{31} & \sigma_{32} & \sigma_{33} \end{pmatrix}$$

The scenarios are (a) pure rotation as assumed for lattice rotations caused by GNDs ($\sigma_{ij} = 0$); (b) pure shear ($\sigma_{12} \neq 0, \sigma_{ij} = 0$); (c) pure bending ($\sigma_{22} \neq$

$0, \sigma_{ij} = 0$); (d) mixed shear and bending ($\sigma_{22} \neq 0, \sigma_{12} \neq 0, \sigma_{ij} = 0$). Furthermore, the maximum peak width $\Delta\theta_{max}$ as well as the maximum energy shift E_{max} was estimated using the formerly applied bending stress σ_{22} of 152 MPa and shear stress σ_{12} of 4.4 MPa. The results are summarized in table 4.6.

Scenarios	(a)	(b)	(c)	(d)	Experiment
$\frac{dE}{d\theta}[eVdeg^{-1}]$	-384.4	-351.8	-231.5	-239.2	-357 ±12
$\Delta\theta_{max}$[deg]	-	$1.6x10^{-3}$	$6.5x10^{-2}$	$6.5x10^{-2}$	$\rangle$ 1.25
ΔE_{max}[eV]	-	-0.41	-15.18	-15.59	$\rangle$ 200

Table 4.6: Summary of four different scenarios compared with the pnCCD experiment. (a)Roitation, (b) Pure shear (c) Pure bending (d) Mixed shear and bending.

Whereas cases (c) and (d) can be excluded, the experimental error of $dE/d\theta$ is too large in order to distinguish between cases (a) and (b). However, not only the maximum angular shift dθ_{max} but also the observed energy shift ΔE_{max} cannot be explained by pure elastic lattice distortions. Therefore, the main contribution to the observed streaking is suggested to be a pure lattice rotation, for instance, caused by the insertion of GNDs. In figure 4.35, the slopes $dE/d\theta$ of the 511 reflection are plotted for all measurement positions.

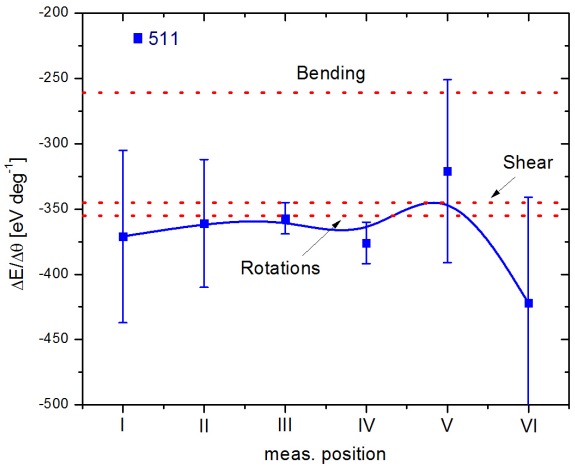

Figure 4.35: Slope $dE/d\theta$ of the 511 reflection at different measurement positions. The values are compared with calculated values for different deformation scenarios (dotted lines).

On the other hand, the FWHM of the Bragg peak does not change with position at the streak or across the cantilever. At the first glance, this could be interpreted by the absence of pronounced SSD density variations, random unpaired GNDs or hydrostatic strain gradients. However, this observation is expected since the Cu cantilever is examined in the unloaded state close to the neutral axis, in which the GNDs in a pile-up can be partly annihilated. Due to the limited energy resolution of the pnCCD, we are currently not able to capture such small energetic variations, which are expected to be well below 30 eV ($\Delta E/E = 2x10^{-3}$).

4.3.10 Conclusion

It is shown that energy dispersive Laue diffraction (EDLD) can be used to evaluate the energetic structure of morphologically complex Laue spots from a plastically deformed Cu micro cantilever. The energy-dispersive pnCCD is operated in the single photon counting mode to record Bragg peaks from a deformed Cu cantilever from different regions across the sample. Bragg peaks from the undeformed regions, are circular and occur at distinct X-ray energies whereas streaked reflections originating from plastically deformed regions are characterized by an energy gradient which is attributed to the lattice rotation caused by the GNDs in the crystal. The experiment is restricted by the relatively small size of the detector chip, one acquisition can be used to collect only a limited number of Laue spots which significantly restricts the interpretation of the phenomena contributing to the streaking at this stage. At least 3 non-coplanar Laue spots are needed to determine the full strain tensor. However, improvements in the experimental setup are already foreseen for the next experiments in order to increase the number of detectable Bragg peaks.

The EDLD method allows recording Laue spots of the sample and to profile their spatial and energetic structures simultaneously. This technique is implemented without changing the incident angle θ and thus in comparison with monochromatic X-ray diffraction, the probed region on the sample is well defined.

Compared to other techniques discussed before, neither the precise knowledge of the incident energy spectrum nor modifications of the X-ray spectra upstream or downstream from the experimental setup are required for a successful Laue

diffraction experiment. Only in the case of perfect crystals, analytical calculations can provide possibilities to predict the Laue spots energies if the primary beam spectrum and the angle of incidence are known, For deformed crystals, the diffracted energies shift in an unpredictable manner, thus a measurement of such shifts is only possible if either the incident energy is precisely known or if an energy-dispersive area detector is used.

The present experiment establishes a new step in the structural analysis of materials especially when deviatoric strains and inter-planar spacing distances d_{hkl} can be determined simultaneously. This allows broadening the application scope of stress measurements to multi grain samples with higher orientation gradients. In the future, it can be expected that on the one side, EDLD performed with novel energy-dispersive detectors like the pnCCD will be used to determine macroscopic strains (of the first order) in elastically stressed samples provided that a sufficient number of Bragg peaks is measured. On the other hand, an analysis of the streaking behavior can serve as an important tool to distinguish between structural effects accompanying plastic deformation of crystals and to understand the deformation behavior of crystals at the micron and the sub-micron length scale. Currently, the method is clearly in its fledgling stage, with some experimental restrictions: the long acquisition time of up to 10 minutes prevents in situ experiments; the small active detector area of 2.88 x 2.88 cm leads to a small opening angles and limits the number of observable Laue spots. Methodologically, it can be expected that the new approach can be used to easily study strain distributions in small crystalline domains using polychromatic X-ray diffraction.

Chapter 5

Summary

Energy dispersive two-dimensional characterization methods have opened a new pathway for material science. The development process has been filled so far with excitement over seeing things which have hitherto been hidden or not possible to observe with previous techniques. However, these new methods depend on the available detector technology as a main tool for non destructive structure analysis. In the presence of 3rd generation synchrotron sources, the detector remains the development bottleneck.

In this thesis, the potential of frame store pnCCD systems for structure analysis in material science using polychromatic synchrotron radiation was investigated. The pnCCD enables simultaneous detection of X-rays energy, spatial coordinates and time stamp of an event. This allow for applications where the scattered X-ray signal from a sample needs to be interpreted in a multi-dimensional coordinate system to follow dynamical processes in the sample. The pnCCD system can be used for application with hard X-rays up to 30 keV. With less than 8 electrons of noise and energy resolution close to the Fano limits in Silicon, the pnCCD is an attractive detector for energy resolved measurements. This work has shown that the pnCCD is also attractive for spatially resolved experiments. The position resolution, previously restricted to the pixel size of 75 x 75 μm^2, can now be improved to reach 1 x 1 μm^2 by software reconstruction of an event landing position. The enhancement of positional resolution has been aided by measuring the charge cloud size created by incident photons of energies between 6.4 and 17.4 keV. In

this energy range, charge clouds created in the detector were measured to have radii (σ) between 7.52 and 9.82 μm.

The above underlined properties of the pnCCD allows for new a experimental methodology to be implemented. In this thesis, the pnCCD is utilized as a tool for polychromatic X-ray diffraction for material structure investigations.

The first experiment demonstrates an anomalous small angle X-ray scattering (ASAXS) performed on an Fe-Pt multilayer system during low temperature annealing. The pnCCD was used to record the diffraction signal from the multilayer system at X-ray energies across the Pt L-edge. Findings confirmed that across the absorption edge, the energy dependent form factor enhances the electron density contrast. The values of the interdiffusion coefficients (D) were measured to be as small as 10^{-19} m^2/s, which are by a factor of 10^3 smaller than values measured at higher temperatures. Moreover, the measurements on the Fe-Pt ML system was performed without time interruptions. The new method, introduced here, removes theses experimental restrictions and takes advantage of edge contrast to measure small scale interdiffusion coefficients.

In another experiment, the energy dispersive μLaue diffraction (EDLD) was used to evaluate the energetic structure of morphologically complex Laue pattern originated from a plastically deformed Cu micro cantilever. In this experiment, the pnCCD was operated in the single counting mode and used to record Laue spots from different regions along the sample. Although only two Laue spots were recorded simultaneously, the energy and spatial coordinates of the reflections were used to index the spots and determine the Miller indices (hkl). Measurements found that the morphology of the Laue spots changes along the sample. The appearance of streaked Laue spots indicated the presence of Geometrically necessary dislocations. By measuring the change in the energy along the streaks (dE/dθ) the deformation scenario was attributed lattice rotations due to the formation GNDs. The present experiment establishes a new step in the structural analysis of materials especially when deviatoric strains and inter-planar spacing distances d_{hkl} can be determined simultaneously.

List of Figures

List of Tables

Bibliography

[1] R. Barabash and G. Ice, "Dislocation in solids," *Elsevier*, vol. 13, pp. 499–601, 2007.

[2] E. Gatti and P. Rehak, "Semiconductor drift chamber an application of a novel charge transport scheme,"

[3] L. Struder, P. Holl, G. Lutz, and J. Kemmer, "Device modeling of fully depletable ccds," *Nuclear Instruments and Methods in Physics Research*, vol. 253, no. 3, pp. 386–392, 1987.

[4] N. Meidinger, B. Schmalhofer, and L. Struder, "Particle and x-ray damage in pn-ccds," *Nuclear Instruments and Methods in Physics Research*, vol. 439, no. 2-3, pp. 319–336, 2000.

[5] S. Send, "Utilization of a frame store pnccd for energy-dispersive laue diffraction with white synchrotron radiation," 2013.

[6] R. C. Alid, S. Bloom, and W. Struck, "Scattering by ionization and phonon emission in semiconductors," *Physical Review B*, vol. 22, no. 12, pp. 5565–5582, 1980.

[7] J. E. Carnes, W. F. Kosonocky, and E. Ramberg, "Free charge transfer in charge-coupled devices," *Electron Devices, IEEE Transactions on*, vol. 19, pp. 798–808, Jun 1972.

[8] R. C. Gonzales and R. E. Woods, *Digital Imaging Processing*. Upper Saddle River, New Jersey 07458: Prentice Hall, 2 ed., 2002.

[9] U. Fano, "Ionozation yield of radiation. ii. the fluctuation of the number of ions," *Physical Review*, vol. 72, no. 1, pp. 26–29, 1947.

[10] A. Abboud, "pn-ccd detector utilized for synchrotron radiation sources," Master's thesis, University of Siegen, Walter Flex Strass 2, 57072, Siegen, April 2010.

[11] S. Send, M. vKozierowski, T. Panzer, S. Gorfman, K. Nurdan, A. Walenta, U. Pietsch, W. Leitenberger, H. Hartmann, and L. Struder, "Energy-dispersive laue diffraction by means of a frame-store pnccd," *Journal of Applied Crystallography*, vol. 42, pp. 1139–1146, September 2009.

[12] H. Tsunemi, K. Yoshita, and S. Kitamoto, "Determination of kilovolt electron energy dissipation vs. penetration distance in solid materials," *Jpn. Journal of Applied Physics*, vol. 36, no. 5A, pp. 2906–2911, 1997.

[13] N. Kimmel, R. Hartmann, P. Holl, N. Meidinger, and L. Struder, "Reconstruction method for the charge collection function of pnccds using data obtained with the mesh experiment," *Nuclear Instruments and methods in physics research, Section A*, vol. 568, pp. 134–140, 2006.

[14] M. Berger, ESTAR, PSTAR, and ASTAR, "computer programs for calculating stopping power and range tables for electrons, protons and helium ions," 1992.

[15] J. J.R., *Scientific charge-coupled devices*. Bellingham, WA, USA: SPIE press, 2001.

[16] T. E. Everhart and P. H. Hol, "Determination of kilovolt electron energy dissipation vs. penetration distance in solid materials," *Journal of Applied Physics*, vol. 42, no. 13, pp. 5837–5846, 1971.

[17] G. R. Hopkinson, "Analytic modeling of charge diffusion in charge-coupled-device imagers," *Optical Engineering*, vol. 26, no. 8, pp. 268766–268766, 1987.

[18] S. Tushar, "Reconstruction of surface morphology from coherent scattering of white synchrotron radiation in hard x-ray regime," 2009.

[19] K. Yoshita, H. Tsunemi, E. Miyata, K. Gendreau, and M. Bautz, "Improvement of the position resolution of the ccd for x-ray use," *IEEE Transaction on Nuclear Science*, vol. 46, pp. 100–106, April 1999.

[20] R. Levine, J. B. Cohen, Y. W. Chung, and P. Georgopoulos, "Grazing-incident small-angle x-ray scattering: New tool for studying thin film growth," *Journal of Applied Crystallography*, vol. 22, pp. 528–532, June 1989.

[21] A. Abboud, S. Send, R. Hartmann, L. Struder, A. Savan, A. Ludwig, N. Zotov, and U. Pietsch, "Application of an energy-dispersive pnccd for x-ray reflectivity: Investigation of interdiffusion in fe-pt multilayers," *Phys. Status Solidi A*, vol. 208, pp. 2601–2607, October 2011.

[22] U. Pietsch, V. Holy, and T. Baumbach, *High-Resolution X-Ray Scattering*, vol. 149. Germany: Springer Tracts in Modern Physics, 2004.

[23] W. H. Wang, H. Y. Bai, M. Zhang, J. H. Zhao, X. Y. Zhang, and W. K. Wang, "Interdiffusion in nano-scale multilayers investigated by in situ low-angle x-ray diffraction," *Physical Review B*, vol. 59, pp. 10811–10822, April 1999.

[24] C. Chantler, "Theoretical form factor, attenuation and scattering tabulation for z=1-92 from e=1-10ev to e=0.4-1.0 mev," *Journal of Physical chemistry*, vol. 24, pp. 71–643, October 1995.

[25] R. Winter, D. Messurier, and C. M. Martin, "Energy-dependent in-situ small-angle x-ray scattering study of nano-ceramics," *Cryst Rev*, vol. 12, 2006.

[26] N. Zotov, J. Feydt, A. Savan, and A. Ludwig, "Interdiffusion in fept multilayers," *Journal of Applied Physics*, vol. 100, October 2006.

[27] A. Kushida, K. Tanaka, and Numakura

[28] M. Sanchez del Rio, R. J.Dejus, and D. Windt, "Xop and imd."

[29] R. Shannon and C. Prewitt, "Effective ionic radii in oxides and fluorides," *Acta Crystallographica Section B*, vol. 25, pp. 925–946, May 1969.

[30] N. Ashcroft and N. Mermin, *Solid State Physics*. Philadelphia: Saunders College, 1976.

[31] G. Ice and J. Pang, "Tutorial on x-ray microlaue diffraction," *Materials Characterization*, vol. 60, pp. 1191–1201, November 2009.

[32] A. MacDowell, R. Celestre, N. Tamura, R. Spolenak, B. Valek, W. Brown, J. Bravman, H. Padmore, B. B.W., and J. Patel, "Submicron x-ray diffraction," *Nuclear Instruments and Methods in Physics Research A*, vol. 467468, p. 936943, July 2001.

[33] N. Tamura, H. Padmore, and J. Patel, "High spatial resolution stress measurements using synchrotron based scanning x-ray microdiffraction with white or monochromatic beam," *Materials Science and Engineering A*, vol. 399, pp. 92–98, High spatial resolution stress measurements using synchrotron based scanning X-ray microdiffraction with white or monochromatic beam 2005.

[34] G. Barabash, R.I.and Ice, M. Kumar, J. Ilavsky, and J. Belak, "Polychromatic microdiffraction analysis of defect self-organization in shock deformed single crystals," *International Journal of Plasticity*, vol. 25, pp. 2081–2093, 2009.

[35] R. Barabash and G. Ice, "Small scale behaviour from x-ray microdiffraction and imaging," *JOM Journal of the Minerals, Metals and Materials Society*, no. 12, 2009.

[36] O. Perroud, R. Vayrette, C. Rivero, O. Thomas, J. S. Micha, and O. Ulrich, "X-ray microbeam strain investigation on cu-mems structures," *Microelectronic Engineering*, vol. 87, pp. 394–397, 2010.

[37] R. Barabash, C. Kirchlechner, O. Robach, O. Ulrich, J. Micha, A. Sozinov, and O. Barabash, "In-situ observation of stress-induced stochastic twin boundary motion in off stoichiometric nimnga single crystals," *Applied Physics Letters*, vol. 103, no. 021909, 2013.

[38] R. Maass, S. Van Petegem, H. Van Swygenhoven, P. Derlet, C. Volkert, and D. Grolimund, "Time-resolved laue diffraction of deforming micropillars," *Physical Review Letters*, vol. 99, no. 145505, 2007.

[39] A. Budiman, S. Han, J. Greer, N. Tamura, J. Patel, and W. Nix, "A search for evidence of strain gradient hardening in au submicron pillars under uniaxial compression using synchrotron x-ray microdiffraction," *Acta Materialia*, vol. 56, pp. 602–608, 2008.

[40] C. Kirchlechner, J. Keckes, C. Motz, W. Grosinger, M. Kapp, J. Micha, O. Ulrich, and G. Dehm, "Impact of instrumental constrains and imperfection on the dislocation structure in micron sized cu compression pillars," *Acta Materialia*, vol. 59, pp. 5618–5626, 2011.

[41] G. Ice, J. Chung, W. Lowe, E. Williams, and J. Edelman, "Small displacement monochromator for microdiffraction experiment," *Review of Scientific Instruments*, vol. 71, pp. 2001–2006, 2000.

[42] O. Robach, J. Micha, O. Ulrich, O. Geaymond, O. Sicardy, J. Hrtwig, and F. Rieutord, "A tunable multicolour 'rainbow' filter for improved stress and dislocation density field mapping in polycrystals using x-ray laue microdiffraction," *Acta Crystallographica Section A: Foundations of Crystallography*, vol. 69, pp. 164–170, 2013.

[43] O. Robach, J. Micha, O. Ulrich, and P. Gergaud, "Full local elastic strain tensor from laue micodiffraction: simultaneous laue pattern and spot energy measurement," *Journal of Applied Crystallography*, vol. 44, pp. 688–696, 2011.

[44] M. Krivoglaz, *Theory of Scattering of X-Rays and Thermal Neutrons by Real Crystals*. New York: Plenum Press, 1969.

[45] M. Ashby, "The deformation of plastically non-homogeneous materials," *Philosophical Magazine*, vol. 21, pp. 399–424, September 1970.

[46] F. Nabarro, *Theory of crystal dislocations*. Oxford, 1967.

[47] O. Ulrich, X. Biquard, P. Bleuet, O. Geaymond, P. Gergaud, J. Micha, O. Robach, and R. F., "A new white beam x.ray microdiffraction setup on the bm32 beamline at the european synchrotron radiation facility," *Review of Scientific Instruments*, vol. 82, pp. 033908–1/6, March 2011.

[48] P. Kirkpatrick and A. Baez, "Formation of optical images by x-rays," *Journal of the optical society of America*, vol. 38, pp. 766–773, September 1948.

[49] C. Kirchlechner, G. W., M. Kapp, P. Imrich, J. Micha, O. Ulrich, J. Keckes, G. Dehm, and C. Motz, "Investigation of reversible plasticity in a micron-sized, single crystalline copper bending beam by x-ray laue diffraction," *Philosophical Magazine*, vol. 92, April 2012.

[50] C. Kirchlechner, G. W.J., M. Kapp, P. Imrich, J. Micha, O. Ulrich, J. Keckes, G. Dehm, and C. Motz, "Investigation of reversible plasticity in a micron-sized, single crystalline copper bending beam by x-ray laue diffraction," *Philosophical Magazine*, vol. 92, pp. 3231–3242, 2012.

Acknowledgements

I would like to thank all the people who helped and supported me throughout the entire process of my doctoral work[1]

- Firstly I would like to express my gratitude to Prof. Dr. Ullrich Pietsch under his direction I have been fortunate to pursue the research described in this thesis.
- I am very thankful to Prof. Dr. Lothar Strüder for the assessment of this thesis and all his support and fruitful discussions concerning my work during the past 5 years.
- I would like to acknowledge PNSensor GmbH and in particular Robert Hartmann and Dr. Martin Huth for all the support in preparing the pnCCD detectors.
- I thank Dr. Sebastian Send and Nadija Pashniak who spent a lot of long days with me during the experiments.
- I am grateful to Dr. Wolfram Leitenberger, Dr. Jean-Sébastien Micha, Dr. Olivier Ulrich, Dr. Odile Robach and Prof. Dr. Nikolay Zotov for all the support. I am also thankful to Prof. Dr. Jozef Keckes and Dr. Christoph Kirchlechner for providing samples and all the helpful discussions and tips.
- I would like to thank my parents, brothers and my sister for all the support and encouragement throughout my studies.
- And I thank Saly, whom her love and support made this work easier.

[1]This work is supported by the Bundesministerium für Bildung und Forschung (BMBF) under grant 05KS7PSA and 05K10PSB.